Study of the Adsorption Mechanisms of Surface Active Agents at the Silica-Water Interface by Total Internal Reflection Raman Spectroscopy

---

A Dissertation Presented to the Faculty

of the Department of Chemistry

University of Houston

In Partial Fulfillment

of the Requirements for the Degree of

Doctor of Philosophy

By

Zlata Simunic-Grenoble

December 2012

Study of the Adsorption Mechanisms of Surface Active Agents at the Silica-Water Interface by Total Internal Reflection Raman Spectroscopy

Zlata Simunic-Grenoble

APPROVED BY:

Dr. Steve Baldelli, Chairman

Dr. Eric Bittner

Dr. Karl M. Kadish

Dr. Shoujun Xu

Dr. Lowell Wood

Dr. Mark A. Smith,
Dean, College of Natural Sciences and Mathematics

Acknowledgement

I thank the Environmental Institute of Houston for their financial support and the Welch Foundation for their funding that provided the necessary research resources and allowed to conduct the research and dedicate my research time for in depth studies of the research related topics.

My particular appreciation goes to my faculty advisor Dr. Steve Baldelli, for his guidance and advice during the research work, and, in particular, for his patience under difficult circumstances, and his encouragement to explore new ideas and research techniques in the scientific field.

I want to thank the committee members for their time to serve on my thesis committee, and their effort to evaluate the research work and provide input to the research results. I also want to thank Dr. Eric Tyrode and Dr. Colin Bain for providing technical support and valuable background information on the TIR Raman technique.

I also thank the members in my research group for their help and their suggestions that contributed to my research work.

Above all, I would like to thank my husband for his understanding and compassionate attitude over several years, and his financial and moral support during my graduate studies. His willingness to take care of necessary daily responsibilities, and his understanding of the time requirements for graduate studies, made a valuable contribution to the success of my research work.

Study of the Adsorption Mechanisms of Surface Active Agents at the Silica-Water Interface by Total Internal Reflection Raman Spectroscopy

---

An Abstract of a Dissertation

Presented to

the Faculty of the Department of Chemistry

University of Houston

In Partial Fulfillment

of the Requirements for the Degree of

Doctor of Philosophy

By

Zlata Simunic-Grenoble

December 2012

Abstract

This study presents the results related to the adsorption behavior of one cationic surface active agent at the silica-water interface and demonstrates the capabilities of the Total Internal Reflection (TIR) Raman sampling configuration to provide spectroscopic information on a molecular level and simultaneously serve as an experimental platform for studying thermodynamic and kinetic properties of molecules at the silica-water interface. This Raman spectroscopic technique takes advantage of an "evanescent electric field" that is generated at the silica-water interface in TIR mode with limited, TIR geometry specific, probing depth.

A minor portion of the research work was related to the adsorption of low vapor pressure solvent molecules from the gas phase at the silica-gas interface, followed by studies at the silica-water interface that proved that neither short alkyl chain hydrophilic ionic liquids nor anionic surfactants adsorb in excess at the silica-water interface.

The primary goal of this work was to study and identify the adsorption mechanisms of a cationic surfactant at the silica-water interface. Spectral analysis and the relevant Raman signal intensities as function of surfactant concentration and surface excess provided the input data for evaluating the thermodynamic and kinetic parameters of benzyldimethylhexadecyl ammonium chloride. Adsorption isotherms were fitted according to the Langmuir model for the pure surfactant, and based on a modified Langmuir model for the surfactant with various concentrations of magnesium chloride, on bare and on hydrophobic silica. The results revealed enhancement of thermodynamic

and kinetic properties of adsorption, as function of electrolyte concentration; the results from the 2nd part of the research work further emphasized the effects of a hydrophobic silica surface on surfactant adsorption behavior; the hydrophobic surface properties promoted different type of surfactant aggregation at the interface, with attenuation of the adsorption driving mechanisms, but with retention of the intrinsic surfactant properties found at the bare silica surface.

Spectral analysis of the Raman scattering intensities as function of concentration and time indicated that no significant reorientation of surfactant molecules takes place at the silica-water interface and the most likely aggregate structure at the surface is spherical at the bare silica surface, and hemi-micellar or hemispherical at the modified hydrophobic silica surface. The study concludes that cationic surfactant adsorption mechanisms can be modulated by substrate properties, electrolyte type, and the concentration levels of both surfactant and electrolyte.

Table of Contents Page

Chapter 5: Research Results from Validation and Optimization Procedures

Chapter 6: Adsorption of Benzyldimethylhexadecylammonium Chloride at the Silica-Water Interface

List of Figures:

List of Tables

Chapter 1: Introduction

1.1. Incentives for interfacial analysis and study of molecular behavior at solid-liquid and solid-gas interfaces

Understanding chemical and physical processes at surfaces and interfacial boundaries, their driving mechanisms, and how these processes can be controlled by optimizing surface properties, is of high interest in scientific, industrial, medical, geological, and environmental technology applications.[1] Interfacial systems include heterogeneous interfacial boundaries at a solid-liquid, solid-gas interface, or involve solid-solid, and liquid-liquid interfaces of different phase composition. In each case, a profound understanding of the molecule-interface interaction as function of interfacial properties is necessary for optimizing surface properties to meet the requirements in electronic, medical, biological, geological and environmental areas.[2-5]

The interfacial boundary between solid and liquid or gas phases is a special region of interest, since the properties at the interface differ from those in the bulk,[6] can vary from one system to another significantly, and are further influenced by external factors. Solid surfaces, in contact with the liquid or gas phase, play an important role for chemical reactions, and are significant factors that contribute to the success of chemical processes in catalysis,[7-12] biological systems,[13, 14] medical and drug delivery,[15] analytical separation techniques,[16] and environmental remediation technologies.[17, 18] Many processes actually occur at surfaces or at the interfacial boundary between two phases; these processes may require adsorption at the surface via mechanisms of physi- or chemisorption, where the

interface serves as an intermediate reaction surface for adsorbing molecules and facilitates chemical reaction processes by influencing thermodynamic and kinetic parameters, i.e., in heterogeneous catalysis.[19] In other processes, the resulting product may be a modified surface with new and specific properties, i.e., in surface coating applications.[20-22] In environmental and remediation technologies, coated solid surfaces provide the adsorbent medium for removal of air, soil, and water pollutants from the environment.[23-26]

1.2. Overview of common surface specific techniques

Various surface analytical techniques have been developed to gather new information on the interaction of molecules with surfaces of interest and to characterize these compounds and their structural configuration. Among these techniques are: X-ray reflectivity, neutron reflectometry, sum-frequency vibrational spectroscopy (SFG),[27-30] direct recoil spectrometry (DRS),[31] reactive oxygen atom "O (^{3}P)" scattering,[32] Rutherford back scattering (RBS),[33, 34]), scanning tunneling electron microscopy (STEM), and ultra-high vacuum (UHV) techniques.[11, 35] UHV techniques for probing molecules on the surface include X-ray photoelectron spectroscopy (XPS), time-of-flight secondary ion mass spectrometry (ToF-SIMS), ultra-violet photoelectron spectroscopy (UPS),[36, 37] metastable atom emission spectroscopy (MAES),[36, 38] metastable impact electron spectroscopy (MIES),[36] which itself is a special technique within MAES, low impact ion scattering (LEIS), high-resolution electron energy loss spectroscopy (HREELS),[36, 37] and

inverse photon emission spectroscopy (IPES).[39] UHV techniques are particularly suitable for studying molecules with low vapor pressure at the interface that can be easily introduced into UHV chambers for surface analytical studies to provide information on the molecular structure and composition at the surface while probing the interfacial region at various technique-specific probing depths for analysis of surface concentration, concentration gradient over various layer depths, structural identification, and electronic density of states.[37]

Non-vacuum techniques include ellipsometry,[40] atomic force microscopy (AFM),[41] and some variants of this technique, i.e., confocal microscopy,[42] and scanning electron microscopy (SEM). Confocal microscopy and related techniques provide surface specific information with a specific probing depth that is controlled by the utilized excitation wavelengths and diffraction-limited resolution of the respective microscope light collection optics.[43]

1.3. Overview of vibrational spectroscopic techniques

Vibrational spectroscopic techniques, i.e., infrared (IR) and Raman spectroscopy, frequently described as complementary techniques, can be configured to provide information on molecular behavior at the interface by probing characteristic vibrational modes of the studied compounds. Some specialized techniques in infrared spectroscopy, i.e., infrared reflection absorption spectroscopy (IRAS), attenuated total reflection infrared spectroscopy (ATR-IR),[44] photon microscopy (PM), and total internal reflection

fluorescence microscopy (TIRF) [45] are widely used tools for surface specific analysis. Among these techniques, SFG, a non-linear optical technique, is considered the most surface sensitive technique providing information on molecular orientation at interfacial boundaries due to its non-linear optical sample probing configuration and related surface specific spectroscopic selection rules.[27, 29, 30, 46-51] The spectroscopic technique employed in this study is a specialized Raman spectroscopic technique based on Raman scattering analysis in total internal reflection mode (TIR Raman). This sampling geometry, where the incident excitation beam is totally internally reflected at the sampling surface, takes advantage of an "evanescent electric field", that allows for surface vibrational analysis of the Raman scattering signals of the molecules at the interface with simultaneous enhancement of the incident electric field strength.[52-55]

1.4. Applications of pure total internal reflection (TIR) Raman spectroscopy

TIR applications as an integral part of Raman spectroscopy have been reported for several decades with initially limited studies of polymer thin films.[56, 57] This type of configuration is favored in experimental settings where total internal reflection of the incident laser beam at the interface between two transparent media can be utilized for enhancement of the electric field strength and excitation of the sampled material of interest without causing damage to the analyzed material. The TIR element might consist of a right-angle or hemispherical prism made of a dielectric material with a refractive index higher than the one of the transmitted medium and material analyzed.[54] Typical

probing depths are in the range of 100 to 200 nm, but ultimately depend on the refractive index ratio of the two phases, the incident angles, and to some extent on the wavelength of the monochromatic excitation source; these penetration depths and resulting surface selectivity can be varied within the depth range given by the sampling configuration, as shown in the analysis of polymeric thin films.[52, 58] Raman spectroscopy in TIR geometry has been employed in studies of molecular behavior at dielectric interfaces, involving materials or substrates, i.e., fused silica (SiO_2), sapphire (Al_2O_3), ZnSe, MgF_2, and CaF_2.[54]

One frequently used material is high purity silica, as shown in various applications, in particular, for the study of the high frequency vibrational modes of surfactants and their thermodynamic and kinetic properties at the silica-water interface. Raman spectroscopy is suitable for probing this type of interface, since the Raman scattering from water molecules is low as compared to IR, and the probed C-H vibrational modes exhibit strong Raman scattering cross sections.[54] Examples are the adsorption study of the cationic surfactant cetyltrimethylammonium bromide (CTAB),[55] and competitive adsorption of CTAB with a non-ionic surfactant at the silica-water interface using a hemispherical silica prism.[59, 60] Both studies used the silica hemisphere as the TIR element and its flat side as the substrate, for establishing adsorption isotherms of the cationic surfactant along with orientational analysis and comparison to SFG data; the competitive adsorption study gave new insight into the adsorption mechanisms as function of mole fractions of the participating cationic and non-ionic surfactant; it described the thermodynamic parameters at equilibrium conditions and presented new information on the kinetic

parameters for the studied compounds in a dynamic system. Other studies were related to biological systems, i.e., phospholipid membranes at solid silica surfaces to obtain information on the conformational order of the organic molecules, and potential defects in Langmuir-Blodgett (LB) type multilayers at the solid-gas interface,[61] or bilayers at the silica-aqueous interface.[62] Structural defects could be identified by comparing the intensity ratio of the relevant C-H vibrational mode intensities. Monolayers of organic mixtures were studied in TIR geometry, with the material positioned and pressurized between solid layers for identification of potential restructuring of the molecules at the interface under confined conditions vs. those in the bulk, with the results indicating that there were no significant changes.[63]

Solid-solid interfaces were studied only within the constraints that the substrate would not exceed monolayer thickness, i.e., the examination of a Langmuir-Blodgett (LB) monolayer of Zn-arachidate sandwiched between a CaF_2 TIR element and a MgF_2 lens at extremely high pressure and compared to the results obtained by the more surface sensitive sum frequency generation (SFG) technique.[64] TIR Raman spectroscopic techniques were applied for the study of waxy layers on the surface of barley leaves where the probing depth of the evanescent electric field was adjusted to the layer thickness of the studied material thus excluding the interference signals from the underlying layers.[65]

1.5. TIR sampling geometry combined with various surface specific or spectroscopic techniques

One special approach for achieving higher surface specificity in microscopic techniques was to combine the TIR concept with confocal microscopy, i.e., for the analysis of PSS:PEDOT thin films using zinc selenide (ZnSe) as the TIR element.[66] The resulting probing depth of 150 nm into the polymer film provided a surface specificity that exceeded the capabilities of conventional confocal Raman microscopy. ZnSe as the internal reflection element (IRE) was the core component in the adsorption study of the surfactant sodium dodecyl sulfate (SDS)[44], by attenuated total internal reflection- FTIR (ATR-FTIR) analysis. The pristine ZnSe surface was used as the hydrophobic substrate in the first part of the experimental work, and then coated with a hematite (α-Fe_2O_3) layer, to create a hydrophilic surface, for comparison of surface property related molecule-surface interactions. Spectral ATR-FTIR analysis provided structural information on the adsorbed molecules as function of surface properties that could be further modulated by solution pH adjustments. The advantages of TIR geometry were demonstrated in the adsorption kinetics study of a porphyrin complex in an evanescent wave cavity ring down experiment (EW-CRDS) with a right-angle silica prism as the TIR element.[67] Even more surface selective analysis could be achieved by integrating an TIR element – a sapphire prism - into the sum frequency generation spectroscopic technique (SFG), as shown by the study of a cationic surfactant at the oil-water interface.[68] Another example of combining a TIR element – also a sapphire prism – with SFG, is the analysis of CO adsorption on polymer covered platinum nanoparticles where the sample cell

contains the TIR element for additional signal enhancement.[19] Similar approaches to incorporate TIR elements into spectroscopic techniques are shown by Watarai et al. during the study of aggregate formation of tetraphenylporphyrin ($H2TPP2^{+}$) at the dodecanol/acid aqueous solution interface by resonant light scattering microscopy with integrated TIR capabilities (RLSM).[69] The TIR enhanced, resonant Raman spectra, clearly showed the aggregate formation domains without the interfering effects of solvent molecules. A similar resonance Raman microscopy study by the same research group demonstrated the effects of dihexadecyl phosphate on the adsorption and orientation of a related porphyrin complex.[70] The orientation of water molecules and structural changes at the silica-aqueous interface as a function of salt addition were successfully demonstrated by integrating a TIR element into the SFG technique.[71] A combination of total internal reflection – sum frequency generation (TIR-SFG) technique probed the behavior of thiolated molecules on gold-plated silica using a sapphire prism as the TIR element with resulting depth specific analysis of the molecules on the ultra-thin gold layer.[72] A heterogeneous catalysis related study of finely dispersed particles on silica surfaces employed SFG analytical techniques in TIR sampling geometry for combining an intrinsically surface specific technique with additional signal enhancing capabilities to study surface phenomena without any destructing consequences for the material under investigation.[73] A similar analytical approach, integration of a TIR element into the SFG optical system, showed the preferential orientation of ionic liquids at the silica-air and silica-water interface.[30] Adsorption and oxidation rates of polymer capped platinum nanoparticles, frequently used in heterogeneous catalytic processes, were successfully

identified by employing SFG in combination with total internal reflection at high pressure conditions.[19] Methanol adsorption and desorption processes in heterogeneous catalysis were studied in situ taking advantage of TIR-SFG, where the surface reactions could be clearly identified with high surface specificity and without any interfering signals from the bulk.[73]

In summary, TIR geometry is well suited for solid-liquid interfacial studies when paired with the appropriate prism material; probing the solid-gas interface allows for more flexibility regarding choice of the TIR element dielectric material since the refractive index ratios of incident and transmitted medium usually are large enough with most dielectric materials to generate the evanescent field effect within a wide range of incident angles. The penetration depth of the evanescent electric field at the solid-gas interface is only relevant in so far as it might cause changes of the refractive index at the interface when the substrate exceeds the thickness of a monolayer.[74]

1.6. Goals of this research work

The primary goal of this research is to evaluate the relationship between surfactant adsorption behavior and interfacial properties by Raman spectroscopy in TIR geometry, with special focus on quartz or amorphous, modified silica, known as fused silica. Quartz or silica are major constituents of soil formations; silica particles are frequently used as solid carriers in oil recovery processes giving strong incentives to study surfactant-silica interaction mechanisms. Adsorption to quartz surfaces of one representative surfactant,

containing a benzyl group ligand at the positively charged ammonium head group and a C_{16} alkyl chain as the non-polar, uncharged hydrophobic tail, is investigated in this study. One objective is to identify the adsorption mechanisms as function of surfactant concentration, electrolyte addition, and silica surface properties, as well as their effects on the surfactant specific thermodynamic and kinetic parameters. The results from the bare silica-surfactant-solution system are correlated to the adsorption properties of the same compound at the modified hydrophobic silica surface.

Spectral analysis of the signal amplitudes and intensity ratios of the key vibrational modes in the high frequency C-H stretching region are used for establishing adsorption isotherms, and obtaining the thermodynamic and kinetic parameters. Structural and orientational analysis of the surfactant by correlation of the Raman scattering signal intensity ratios with surfactant concentration and their evolution over time in the various solution-surfactant-silica systems provides information on the most likely structure of the surfactant aggregates.

The compiled results of the study provide comprehensive information on the surface chemistry and applicability range of this type of cationic surfactant, i.e., optimum concentration range of the surfactant with maximum efficiency and minimal surfactant consumption.

Chapter 2: Background and Theory of Raman Spectroscopy

2.1. Conventional Raman spectroscopy

Raman spectroscopic techniques probe the vibrational modes of molecular species that are susceptible towards interactions of the electronic cloud or ellipsoid of the covalent chemical bond with an incident monochromatic electric field, irrespective of the sample matrix. Fundamentally, Raman scattering is an isotropic, incoherent two-photon emission process[75] that has its origin in the interaction of the polarizability tensor along the molecular polarization coordinate with a monochromatic and coherent incident excitation source.

The induced polarization in Raman scattering contrasts IR vibrational modes that depend on the permanent dipole moment transition of the molecule; Raman scattering has its origin in the interaction of an oscillating electric field vector from a monochromatic radiation source with the electron cloud surrounding the molecular bond that results in a three-dimensional distortion of this electronic polarizability ellipsoid with subsequent scattering of some or all of the adsorbed incident photon energy, described as Rayleigh, Stokes, or anti-Stokes scattering. The Raman scattering intensities depend on several parameters:

$$I_{scatter} \propto N_m \; I_{L(\lambda)} \; \sigma(\lambda) \; \Omega(\lambda) \; D(\lambda) \; QE(\lambda) \qquad (2.1.1.)$$

where:

N_m = number density of excited vibrational modes

$\sigma(\lambda)$ = Raman scattering energy cross section

$\Omega(\lambda)$ = scattering solid angle (sr^{-1})

$D(\lambda)$ = path length and collection optics geometric factors

$QE(\lambda)$= detector quantum efficiency

The technique employed in this work is based on linear optics with the assumption that the interaction between incident energy and vibrational modes intensity is 1st order, unlike non-linear Raman techniques, that depend on a second-order polarizability, i.e., Coherent anti-Stokes Raman Spectroscopy (CARS),[76] and require additional excitation sources.[77]

2.2. Raman Polarizability Tensor

The linear induced dipole vector is described by the generalized following expression:

$$P = \alpha_{ij} E \quad (2.2.1)$$

where α defines the polarizability and E the electric field strength. This generic expression describes the time and frequency dependent linear induced dipole vector resulting from the expansion of the following expressions in the classical description:[77]

$$E = E_o \cos(\omega_o t) \quad (2.2.2)$$

$$Q = Q_k \cos(\omega_k t + \delta_k) \quad (2.2.3)$$

$$P^{(1)} = \alpha \cdot E_o \cos(\omega_o t) \quad (2.2.4)$$

where E_o and E refer to the incident and local electrical field, Q determines the polarization coordinate, and $P^{(1)}$ the first order polarization. Eqs (2.2.1.) to (2.2.4) need further expansion to include the surface specific interaction between s- and p-polarized

incident beams and the derived Raman polarizability tensor that is discussed in section 2.4.

Combining above expressions gives the expression for the frequency dependent and space averaged polarization of the ellipsoid along the vibrational coordinate:

$$P^{(1)} = P^{(1)}(\omega_o) + P^{(1)}(\omega_o - \omega_k) + P^{(1)}(\omega_o + \omega_k) \qquad (2.2.5)$$

The 1st term in the polarization expression, $P^{(1)}{}_o(\omega_o)$ gives rise to the dominating and strong Rayleigh scattering, the derived polarization $P^{(1)}(\omega_o-\omega_k)$ that defines the weaker Stokes Raman scattering and the even weaker anti-Stokes Raman scattering

defined as $P^{(1)}(\omega_0+\omega_k)$. The anti-Stokes type of scattering depends on the molecules already present in a vibrational excited state that have a smaller population density compared to those in the ground state as given by the Boltzmann expression:

$$\frac{N_1}{N_o} = \frac{g_1}{g_o} e^{-\nu_s / kT} \qquad (2.2.6)$$

where N_o and N_1 describe the number density of molecules in the ground- and excited state, and g_o and g_1 define the energy levels of these energy states, and ν_s stands for the scattering frequency.

Rayleigh scattering occurs at the same wavelength as the incident light with the same phase whereas the Stokes shifted Raman scattering signals show a phase shift δ_k relative to the incident phase with Q_k being the coordinate of the normal vibration. The three-dimensional polarizability tensor α_{ij} consists of a 3x3 matrix and is a directional and symmetric tensor. The most intense Rayleigh scattering signal arises from the induced electric dipole resulting from the interaction of the electric field dipole oscillating at

frequency ω_o with the molecular dipole oscillating at the same frequency as the incident electric field and its equilibrium position. In contrast, the weaker Raman Stokes and anti-Stokes scattering are generated when the electric field dipole oscillating at ω_o is modulated by the molecular vibration that oscillates with a vibration specific frequency of ω_k. The resulting Raman scattering at $\omega_o \pm \omega_k$ and signal intensity finally depend on several factors, i.e., favorable interaction between the electric field vector and the molecular oscillating dipole, expressed as the Raman polarization susceptibility, and the Raman scattering energy cross section, given by the ratio of irradiated power vs. scattering intensity.[78]

The derived polarizability tensor α'_{ij} distinguishes itself from the equilibrium position polarizability tensor α_o not only in terms of scattering intensity. The derived polarizability tensor coordinates do not have to coincide with those of the equilibrium polarizability tensor and can be positive or negative, which again indicates, that representing the Raman polarizability of the derived Raman tensor as a real ellipsoid is a simplified way of describing the system. While Rayleigh scattering is in phase with the incident radiation, Raman scattering is incoherent, and may not reflect the phase and directionality found in the incident radiation. It does, however, reflect the energy of excitation of the respective vibrational normal modes. Incoherent light scattering may complicate the analysis of Raman vibrational modes, to some extent, but also provides additional tools for molecular and orientational analysis, when applying the appropriate Raman selection rules for isotropic systems, i.e., as the bulk of a liquid or solid, and anisotropic environments, i.e., surfaces and interfaces, as discussed in detail in section 2.4.[78]

Common excitation energies are usually laser sources emitting in the visible wavelength region with the 532 nm wavelength, i.e., generated by a solid state diode pumped laser. Shorter and more energetic wavelengths of 457 and 488 nm (if argon ion lasers are available) and lower have also been employed; these can be generated by frequency-doubling the fundamental wavelengths to obtain UV range excitation wavelengths of higher energy, as applied in resonance Raman spectroscopy.

2.2.1. Significance of Raman depolarization ratio measurements

The 2rd rank Raman polarizability tensor is known to possess directionality and favor symmetric polarization modes. Symmetry considerations and Raman polarizability tensor properties in combination with controlled experimental conditions allow to determine the degree of symmetry of a vibrational modes by relating the measured scattering intensity of the Raman signal in a known and given direction and polarization to the known orientation of the incident electric dipole and to estimate the symmetry contributions from the ratio of the transmitted vs. the incident signal intensity. A carefully designed experimental configuration for conducting a so-called “Depolarization Ratio “ study would include collection of the scattered light in at least two steps and at two different sampling geometries using the necessary optical components and polarizers. The first part would consist of irradiating the studied material with plane polarized light with both the incident electric dipole and measurement of the scattered light along the vertical (parallel) and also along the horizontal axis ; the second step requires collection of the horizontally

scattered light in both vertical and horizontal (perpendicular to the incident light) polarization mode. The scattering intensity ratio of parallel vs. perpendicularly polarized and collected signal (depolarization ratio ρ) and comparison of polarized and depolarized bands, using the common expression and ratio of intensity, give information on the level of symmetry of a Raman active vibrational mode. In a fully isotropic system, i.e., in the bulk of a solution, depolarized bands usually show a depolarization value of $\rho = 0.75$ whereas polarized bands exhibit a ρ value between 0 and 0.75 that is indicative of the level of symmetry. The closer the ρ value to 0, the more symmetry can be assigned to a Raman active vibrational mode. In practice, a value of $\rho = 0.1$ would be indicative of a fully symmetric vibrational mode. This guideline is not always valid in resonance Raman spectroscopy, where polarization ratios of $\rho > 0.75$ have been observed, since vibrational transitions are coupled to electronic transitions, and light absorption occurs within an electronic excited state.[79]

2.3. Surface specific Raman polarizability tensor

The Raman effect for molecules adsorbed at the surface depends on the orientation of the incident electric field vector that is defined as either p- or s-polarized light relative to the plane of incidence. In contrast to isotropically scattered light from molecules present in the bulk of a gas, liquid, or solid, the Raman scattering from molecules at the surface is isotropic in the two dimensions (xy) transverse or parallel to the surface, and uniaxially anisotropic perpendicular to the surface plane in the z-direction. The Raman scattering

intensity strongly depends on the polarization vector of the respective normal mode relative to the polarization of the incident light. For instance, normal modes of vibration with their polarization tensor parallel to the surface normal will experience strong interaction with the electric oscillating dipole of a p-polarized incident electric field resulting in a large scattering cross section while an s-polarized incident electric field strongly interacts with an electric dipole oscillating parallel to the surface.[54, 55, 74]

Taking advantage of these interactions, experimental studies can be designed to measure and compare the intensity of Raman scattering at four different configurations, with p- and s-polarized light on the incident side, and collection optics set along either x- or y-axis to obtain qualitative information on changes in orientation and structure of the molecule from their intensity ratios. In this study, the criteria were intensity ratios of the prominent C-H stretching vibrations from p- and s-polarized spectral analysis as follows:

Sy/Sy Ratio

$CH_3\ \nu_{as}/CH_2\ \nu_s$
$CH_2\ \nu_{as}/CH_2\ \nu_s$

Pxy/Pxy Ratio

$CH_3\ \nu_{as}/CH_2\ \nu_s$
$CH_2\ \nu_{as}/CH_2\ \nu_s$

Pxy/Sy Ratio

$CH_3\ \nu_{as}/CH_3\ \nu_{as}$

$CH_2\ \nu_{as}\ /\ CH_2\ \nu_{as}$

$CH_2\ \nu_s\ /\ CH_2\ \nu_s$

where S- and P define the polarization of the incident electric field, and the subscripts refer to the collection axes. The ratios within one polarization are indicative of the degree of the alkyl chain ordering, whereas the ratios between two polarization settings relate to the average tilt relative the surface normal. Since the measured intensities are related to the actual number density of the molecules, and collection efficiencies differ from each other, only trends or changes in intensity ratio are significant within this study. The preferred mode of collecting the Raman scattered signals, was s-polarized incident light without polarizer in the collection optics, or alternatively with the polarizer set to collect the scattered signal along the same y-axis, i.e., parallel to the axis of the incident excitation beam (S_y). Only selected experiments included both s- and p-polarized sampling geometries for the purpose of structural and orientational analysis, as discussed above.

The Raman scattering signal intensities in the four principal sampling and signal collection configurations and their dependence on the incoming electric field vector and its interaction with the respective Raman polarizability tensor can be derived from the 3x3 polarizability matrix and the electric field column vector as follows:[77]

$$P_x = \{\alpha'_{xx} E_x + \alpha'_{xy} E_y + \alpha'_{xz} E_z\} Q_{ko}$$

$$P_y = \{\alpha'_{yx} E_x + \alpha'_{yy} E_y + \alpha'_{yz} E_z\} Q_{ko}$$

$$P_z = \{\alpha'_{zx} E_x + \alpha'_{zy} E_y + \alpha'_{zz} E_z\} Q_{ko}$$

with Q being the normal coordinate for the kth vibrational normal mode. For p-polarized light, and the E_z field vector on the incident side, these surface selection rules reduce the polarizability matrix to the following elements:

$P_x = \alpha'_{xx} E_x + \alpha'_{xz} E_z$

$P_y = \alpha'_{yx} E_x + \alpha'_{yz} E_z$

$P_z = \alpha'_{zx} E_x + \alpha'_{zz} E_z$

Only the polarization involving the diagonal polarizability tensors $\alpha'_{xx} E_x$ and $\alpha'_{zz} E_z$, and the off-diagonal tensors $\alpha'_{yx} E_x$, $\alpha'_{zx} E_x$, and $\alpha'_{xz} E_z$,, $\alpha'_{yz} E_z$, are active. The following polarizability tensors are isotropic at the surface:

$\alpha'_{yx} = \alpha'_{xy}$, and $\alpha'_{xz} = \alpha'_{yz}$

For s-polarized light, and only the E_y field vector present, the only active polarization combinations are: $\alpha'_{yy} E_y$, $\alpha'_{xy} E_y$, and $\alpha'_{zy} E_y$ from:

$P_x = \{\alpha'_{xy} E_y\} Q_{ko}$

$P_y = \{\alpha'_{yy} E_y\} Q_{ko}$

$P_z = \{\alpha'_{zy} E_y\} Q_{ko}$

the Raman tensors $\alpha'_{yy} = \alpha'_{xx}$, and $\alpha'_{xy} = \alpha'_{yx}$, are also isotropic at the surface.

Further restrictions are imposed by the scattering intensity collection optics. Signal scattering originating from polarization in the z-direction (P_z), disregarding its presence

at the incident side and its magnitude, is negligible on the collection side. Without a polarizer in the collection optics, all active Raman vibrational modes for the respective polarization mode (P_x and P_y) are included with their scattering intensities along x-and y-collection axes, proportional to the number density of the normal modes, and Raman cross section. For p-polarized light and light collection along the x-axis, i.e., the same optical axis as the incident light, the diagonal Raman tensor $\alpha'_{xx,}$ and $\alpha'_{xz} = \alpha'_{yz}$, are active, whereas for collection along the y-axis, only α'_{yx} and α'_{yz} are present. For s-polarized light, and collection along the y-axis, the fully symmetric Raman tensor α'_{yy} (= α'_{xx} at the surface), and for collection with the polarizer along the x-axis, the off-diagonal Raman tensor α'_{xy} is accounted for.

These selection rules lead to a final expression for the Raman tensor and the signal intensity relationship:[70]

$$Ip_x: \quad \alpha'_{xx} \left| E_x \right|^2 + \alpha'_{xz} \left| E_z \right|^2 \tag{2.3.1}$$

$$Ip_y: \quad \alpha'_{yx} \left| E_y \right|^2 + \alpha'_{yz} E_z \left|^2 \right. \tag{2.3.2}$$

$$Is_x: \quad \alpha'_{xy} \left| E_y \right|^2 \tag{2.3.3}$$

$$Is_y: \quad \alpha'_{yy} E_y \left|^2 \right. \tag{2.3.4}$$

where the subscripts α_{ij} describe the matrix elements of the Raman polarizability tensor, based on the laboratory fixed coordinate system, and E_x, E_y, and E_z, stand for the incident electric field vectors. I_p and I_s describe the intensity of the scattered signal with the incident electric field vector in either p- or s-polarized modes relative to the surface, and

the subscripts x and y give the orientation of the polarizer setting on the signal collection side.

The final definitions in eqs (2.3.1.) through (2.3.4) for relating polarization and collected signal intensity at the surface do not contain any qualitative component. The electric field vectors E_x and E_z interact primarily with the asymmetric polarizability tensors $\alpha'_{xy} = \alpha'_{yx}$, $\alpha'_{yz} = \alpha'_{xz}$, (isotropic at a uniaxial surface in the transverse x-y plane). The collected signal from P_x polarization contains only contributions from the off-diagonal Raman tensor $\alpha'_{xz} E_z$ and from $\alpha'_{xx}E_x$, both for collection of the scattered Raman signals along the x- and/or y-axis. The strongest contributions to the Raman scattering arise from the combination of the symmetric, diagonal tensor interacting with the s-polarized electric field vector, primarily with collection of the scattering intensity along x- and y-axis, or from the y-axis only.[55]

The isotropic nature of the derived Raman polarizability tensor and the resulting scattered light intensities along the xy plane, parallel to the surface plane, and anisotropy of the Raman scattering in the z-direction, bring about one prominent difference between the intensity ratios of the incident vs. scattered light between surface specific Raman vs. depolarization Raman experiments. The fully symmetric derived Raman polarizability element $\alpha'_{zz} E_z$, that scatters primarily along the x-axis, is negligible in the sampling geometry of surface specific Raman (which includes TIR Raman) spectroscopy.

2.4. The electric field vector and Fresnel coefficients at the interfacial boundary

The electromagnetic field in the macroscopic description of Maxwell's equations is expanded to give the electromagnetic field as a superposition of monochromatic fields.

$$E(r,t) = E(k,\omega)\cos(k \cdot r - \omega t) \quad \text{and its Fourier transform:} \tag{2.4.1}$$

$$\hat{E}(r,\omega) = 1/2\pi \int E(r,t)\, e^{i\omega t}\, dt \quad \text{and the inverse Fourier transform} \tag{2.4.2}$$

$$E(r,t) = \int E(r,\omega)\, e^{-i\omega t}\, d\omega \tag{2.4.3}$$

The above equation can be separated out to give the real part E (r,t) and its complex and spatial part E (r) as follows:

$$E(r,t) = \mathrm{Re}\{E(r)\, e^{-i\omega t}\} = \frac{1}{2}[E(r)\, e^{-i\omega t} + E^{*}(r)\, e^{i\omega t}] \tag{2.4.4}$$

Maxwell's equations also hold at an interfacial boundary between two dielectric media, but their differential form needs to be modified to an integral form to account for the discontinuity at the boundary and the boundary condition. If the detailed description of the boundary condition in their integral form is applied to a planar wave incident on a planar surface, the so-called Fresnel coefficients for reflection and transmission of the electromagnetic wave amplitudes are obtained. For the plane polarized wave, the following expression $E^{*}e^{(k \cdot r - \omega t)}$ can be written as the superposition of two orthogonal and plane polarized waves that are defined as parallel (p), and perpendicular (s), to the plane of incidence that leads to the final and general description:

$$E_1 = E_1^{(p)} + E_1^{(s)} \tag{2.4.5}$$

At the boundary condition, $E_1^{(s)}$ is parallel to the surface, and $E_1^{(p)}$ is perpendicular to the surface, but considered parallel to the plane of incidence. Further distinction of the electromagnetic field wave vectors is made by defining: k_1 = incident wave vector and k_2 = transmitted wave vector, ε is the relative permittivity of the material, also defined as the dielectric constant at optical frequencies, where $\varepsilon = n^2$,[80] and μ is defined as the magnetic permeability. The dielectric and transparent optical components and substrates used in context with this research study are considered non-magnetic (μ=1) and the permeability constant μ is usually omitted. In a Cartesian coordinate system, one obtains for the boundary conditions a more straightforward simplified expression; under the assumption that the wavevector components k_x and k_y are transverse, and that $k_x^2 + k_y^2 + k_z^2 = 1$, the wave vectors can be defined as:

$$k_1 = \frac{\omega}{c}\sqrt{\varepsilon_1} \qquad (2.4.6) \qquad k_2 = \frac{\omega}{c}\sqrt{\varepsilon_2} \qquad (2.4.7)$$

$$k_{1z}^2 = \sqrt{k_1^2 - (k_x^2 + k_y^2)} \qquad (2.4.8) \qquad k_{2z} = \sqrt{k_2^2 - (k_x^2 + k_y^2)} \qquad (2.4.9)$$

the subscripts 1 and 2 refer to the incident and transmitted wave vectors at the interface, with xy in the transverse direction along the surface, and z refers to the direction perpendicular to the surface. The transverse wave vector k_x+k_y can be expressed in terms of the angle of incidence, $k_1 \sin\theta_i$. By substituting these expressions into the previous equations, the expressions for the incident and transmitted wave vectors at the interfacial boundary are as follows:

$$k_{z1} = k_1\sqrt{1 - \sin^2\theta_i} \qquad (2.4.10) \qquad k_{z2} = k_2\sqrt{1 - n_{it}^2 \sin^2\theta_i} \qquad (2.4.11)$$

The resulting Fresnel coefficients are obtained for the amplitudes of the reflected and transmitted waves for s- and p-polarized incident electric fields:

$$t^{(p)}(k_x, k_y) = \frac{2\varepsilon_2 k_{z_1}}{\varepsilon_2 k_{z_1} + \varepsilon_1 k_{z_2}} \sqrt{\frac{\mu_2 \varepsilon_1}{\mu_1 \varepsilon_2}} \tag{2.4.12}$$

$$t^{(s)}(k_x, k_y) = \frac{2\mu_2 k_{z_1}}{\mu_2 k_{z_1} + \mu_1 k_{z_2}} \tag{2.4.13}$$

$$r^{(s)}(k_x, k_y) = \frac{\mu_2 k_{z_1} - \mu_1 k_{z2}}{\mu_2 k_{z_1} + \mu_1 k_{z_2}} \tag{2.3.14}$$

$$r^{(p)}(k_x, k_y) = \frac{\varepsilon_2 k_{z_1} - \varepsilon_1 k_{z2}}{\varepsilon_2 k_{z_1} + \varepsilon_1 k_{z_2}} \tag{2.4.15}$$

Fresnel coefficients for p-polarized light are usually larger vs. s-polarized light, and strongly depend on the angles of incidence relative to the surface normal. The p-polarized light has the unique property of $t^{(p)}$ being equal to 1 at the so-called Brewster angle condition, defined as $\theta_B = \tan^{-1} n_t / n_i$.

Wave vectors become complex numbers in the special case where $n_1 > n_2$ at the interface and the incident angle is smaller than or equal to the critical angle. Under these conditions, an evanescent electric field is generated at the boundary, containing sufficient energy to excite the molecular vibrational modes that can be utilized for the special application of TIR Raman spectroscopy, as described below in Section 2.5.[53]

2.5. TIR Specific Raman Spectroscopy

Total internal reflection Raman spectroscopy follows the same Raman scattering and selection rules as surface Raman spectroscopy. It contains, however, one additional optical effect that stems from the integration of an optically transparent dielectric element into the sampling system. This TIR element interacts with the incident electric field leading to important modifications of the electric field properties at the interfacial boundary between the TIR element and the transmitted medium. Raman spectroscopy in total internal reflection mode offers the advantage that the sample is not directly exposed to a highly energetic laser beam that might cause damage of the material under study. The signal scattering intensity can be higher as compared to conventional Raman spectroscopy, and allows for surface specific probing of the interfacial region without the requirement of signal enhancing metal surface, i.e., silver, colloidal particles, or surface roughness, as in surface-enhanced Raman spectroscopy (SERS).[70] The evanescent electric field generated at the silica-water interface, contains sufficient excitation energy for Raman scattering, but its energy flux in the z-direction, perpendicular to the interface, is practically non-existent based on the Poyting vector description. The incident excitation beam, that can be either p- or s-polarized relative to the surface, is totally internally reflected, when the incident angle θ_i is larger or equal to the critical angle, and the medium of incidence, here the fused silica, has a higher index of refraction than the medium of the transmitted beam (following Snell's Law).[53, 81]

The critical angle is given by: $\theta_c = \sin^{-1}(n_t/n_i)$, where n stands for the refractive index (also defined as the square root of the dielectric constant at optical frequencies) of the respective medium, and the subscripts i and t refer to the incident and transmitted medium. It was determined as $\theta_c = \sin^{-1}(1.34/1.46) = 66.6^\circ$ for the silica-water system used in this study. The electric field enhancement coefficient, derived from the complex wave propagation vectors, is proportional to the square of the ratio of the transmitted vs. incident electric field. A schematic of the TIR Raman sampling and scattering signal collection and TIR element-light collection set-up, as used for this study, is shown below in Figs.2.5.1 and 2.5.2.

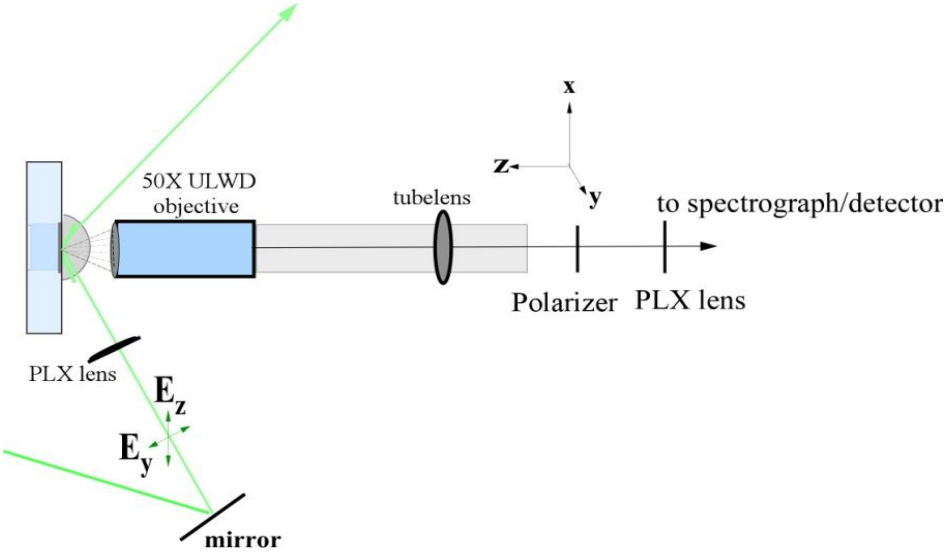

Fig. 2.5.1: TIR sampling geometry

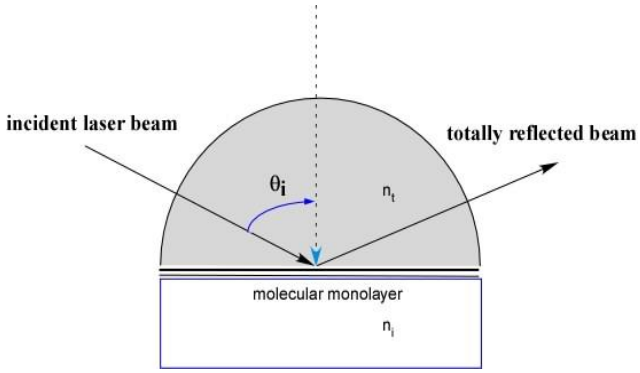

Fig. 2.5.2.: IR grade silica hemisphere as TIR element

2.5.1 The evanescent electric field and Fresnel transmission coefficients

In case of the incident angle $\theta_i \geq \theta_c$, the electric field vector becomes a complex number with the electric field enhancement coefficient being proportional to the ratio of the squared transmitted vs. incident electric field. The transmitted electric fields for p- and s-polarized incident beams at the silica-water interface are described by the following equations:

$$E_2 = [-E_1^{(s)} t^{(s)} \theta^i] e^{ik_x x + ik_z z} \qquad (2.5.1.1)$$

$$E_2 = [-E_1^{(p)} t^p (k_x) k_{z_2} / k_2] e^{ik_x x + ik_z z} \qquad (2.5.1.2)$$

where E_2 and E_1 are the transmitted and incident fields and the k's are the propagation wave vectors in the respective directions, as defined in the previous section. The subscripts 1 and 2 define the vectors for the incident or transmitted electric fields. For

incident angles larger than the critical angle, the electric field vector k_{z2} is imaginary and the electric field is described as:

$$E_2 = [-iE_1^{(s)} t^{(s)}(\theta_1)] e^{i \sin\theta_1 k_1 x} e^{-\beta z} \tag{2.5.1.3}$$

and $$E_2 = [-iE_1^{(p)} t^{(p)}(\theta_1) \sqrt{n_{it}^2 \sin^2\theta_i - 1}] e^{i \sin\theta_1 k_1 x} e^{-\beta z} \tag{2.5.1.4}$$

The resulting Fresnel transmission coefficients define the electric field enhancement as well as the penetration depth of the transmitted electric field in the z-direction, perpendicular to the surface, and into the medium of lower optical density. The Fresnel transmission coefficient is derived from the incident and transmitted wave vectors by using the respective refractive indices (the square root of the dielectric constant for optical frequencies) [80] and expressing the wave vectors in terms of incident angles:

$$t^{(s)} = \frac{2n_1\sqrt{1-\sin\theta_i}}{n_1\sqrt{1-\sin\theta_1} + n_1\sqrt{1-n_{it}^2 \sin\theta_i}} \tag{2.5.1.5}$$

$$t^{(p)} = \frac{2n_2\sqrt{k_1^2 - k_1^2 \sin^2\theta_i}}{n_2\sqrt{k_1^2 - k_1^2 \sin^2\theta_1} + n_1\sqrt{k_2^2 - k_1^2 \sin\theta_i}} \sqrt{\frac{\mu_2\varepsilon_1}{\mu_1\varepsilon_2}} \tag{2.5.1.6}$$

The penetration depth of the transmitted electric field in the z-direction, perpendicular to the surface, and into the medium of lower optical density, can be derived from above eqs (2.28) and (2.29) to define an exponentially decaying electric field, in the z-direction,

where the term β in these equations can be expressed as shown in eq (2.5.1.7) to give the final expression for the evanescent field penetration depth.

$$z = d = \frac{1}{\beta} = \frac{\lambda_\circ}{4\pi(n_i^2 \sin^2 \theta_i - n_t^2)^{1/2}} \qquad (2.5.1.7)$$

The electric field enhancement is proportional to the angle of incidence relative to the critical angle and can be several times the original electric field. In the experimental part related to adsorption mechanisms at the solid-liquid interface of this study, however, the incident angle was set at 73˚, resulting in slightly lower Raman scattering intensity, since the Fresnel coefficient is reduced, but providing more surface specific information of the molecules in both quantitative terms, i.e., surface excess, and molecular identify, at the interface.[55]

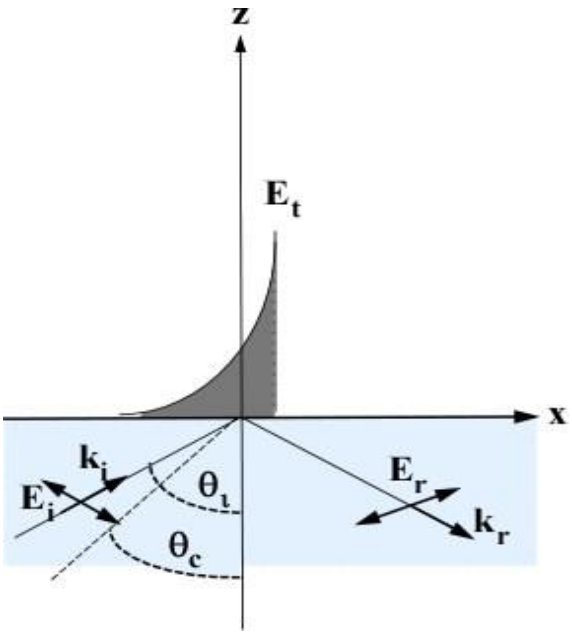

Fig. 2.5.1.1: Evanescent field at the interfacial boundary for $n_1 > n_2$ and total internal reflection

The penetration or probing depth in this configuration is related to the incident wavelength and inversely proportional to the refractive index ratios, as shown in eq. 2.5.1.7. It was determined as 99 nm for an incident laser wavelength of 488 nm (argon ion gas laser) and 108 nm for 532 nm wavelength (solid-state diode pumped laser) at the angle of incidence of 73˚, with only negligible signal contribution from molecules present in the bulk. It follows from the Fresnel transmission coefficients, that the evanescent wave penetration depth into the medium of lower refractive index becomes smaller with larger incident angle θ_i, relative to the critical angle as shown below (Figs 2.5.1.2 and 2.5.1.3) for the transmission coefficients in p- and s- polarization geometry.

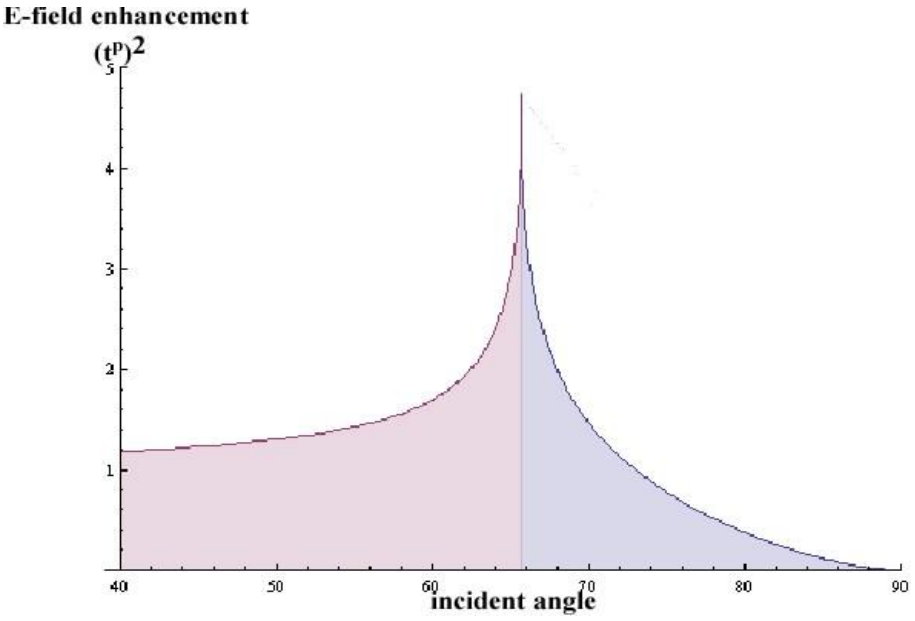

Fig. 2.5.1.2: Electric field enhancement $(t^p)^2$ for p-polarization; θ_c =65.6˚ and λ =532 nm

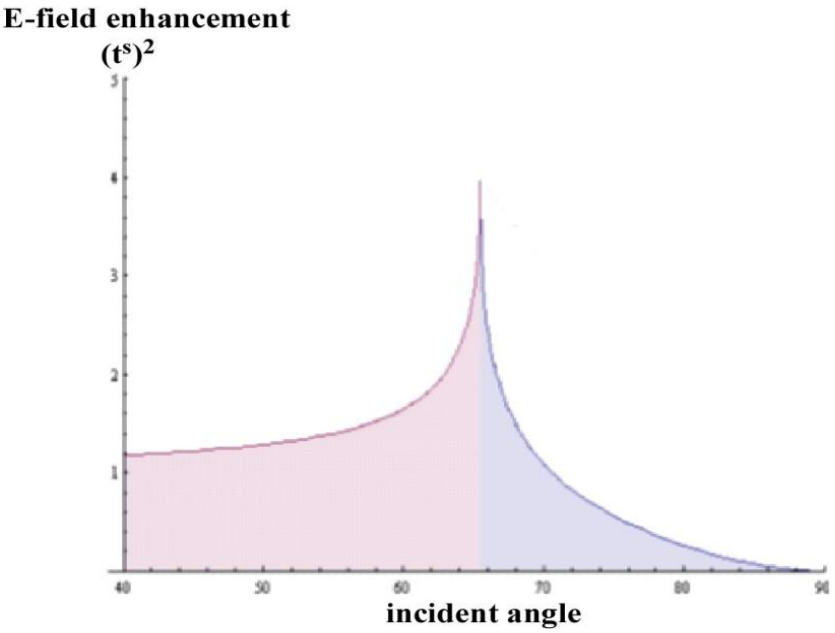

Fig. 2.5.1.3: Electric field enhancement $(t^s)^2$ for s-polarization; $\theta_c = 65.6^\circ$ and $\lambda = 532$ nm

As shown in the graphs, the transmission coefficient for p-polarized light is higher than the one observed for s-polarization when working near the critical angle, although the difference is relatively small due to the small refractive index ratio of the silica-water interface. The difference diminishes as the incident beam is set farther away from the critical angle and becomes negligible at the angles of incidence used in this study. As found in our experiments, and confirmed in literature, the Fresnel coefficient in connection with the favorable interaction of the electric field vector in s-polarized fields with the symmetric polarizability tensor of the Raman oscillating dipole gives stronger signal intensities and clearly allows to distinguish the vibrational modes with higher symmetry relative to the surface plane.

2.5.2. Effects of sampling geometry on Raman scattering intensity

If maximum electric field enhancement is desirable, the dielectric material should provide as large refractive index ratios as possible. A high ratio of n_i/n_t results in higher Fresnel transmission coefficients for any angle of incidence as compared to smaller refractive index ratios. The wavelength is of minor concern when seeking strong field enhancement. It factors, however, into the definition of the penetration depth that is related to the incident wave vector as expressed in eq 2.5.1.7. Undesired side-effects from the dielectric material need to be taken into account when choosing the dielectric material. For example, diamond is a good dielectric with high refractive index n and little interference signals, but its birefringent optical properties may not give the desired results.[54]

This study was conducted at the silica-water and silica-air interface, with a refractive index of fused silica of 1.46, and the critical angle for the silica-air interface being 43.2 to 43.8˚ depending on the laser beam wavelength. At the silica-water interface, the critical angle increases to 65.8˚ and 65.6˚ for wavelengths of 488 and 532 nm, respectively (the small difference arises from dispersion effects with decreasing silica refractive index as the wavelength increases). Incident beams at the critical angle itself are not desirable, since the pure TIR condition may be violated due to some dispersion and deviation from the target incident angle, when focusing the laser beam onto the sampling spot. The N.A. of the laser beam cone has to be factored in and the actual incident angle chosen far enough away from the critical angle. At the silica-air interface, maximum electric field

strength enhancement will provide strong Raman scattering intensity without any concern of penetration depth into the gas phase, assuming that the probed substrate does not exceed a thickness of more than several monolayers that might affect the local electric field strength.

At the silica-water interface, the penetration depth into the aqueous medium affects the overall Raman signal and contains contributions from the bulk that are proportional to the actual probing depth. Working close to the incident angle will give higher enhancement of electrical field but also leads to increased probing depth into the bulk and consequently loss of surface specificity.

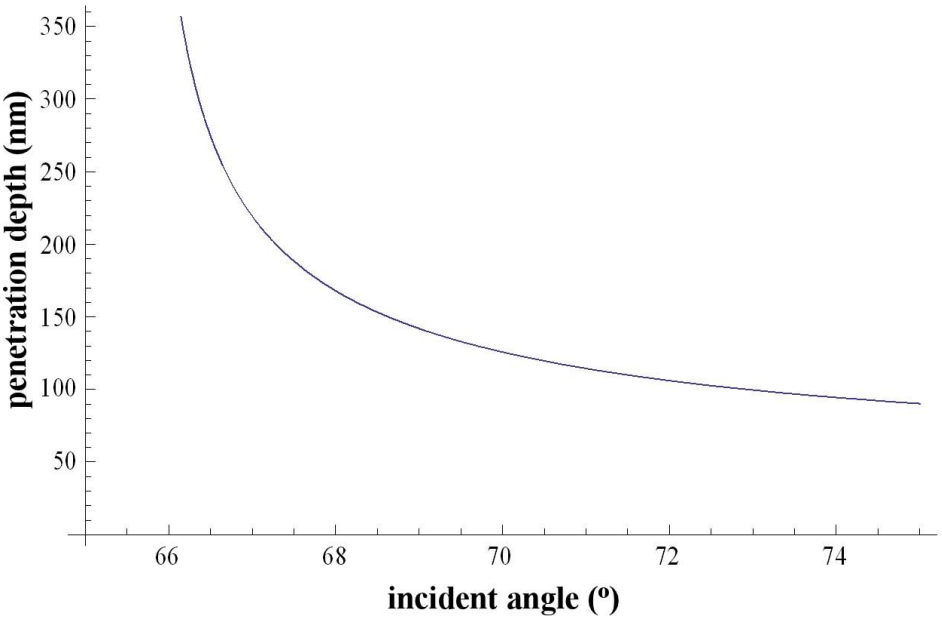

Fig. 2.5.2.1: Evanescent field penetration depth (nm) as function of incident angles at incident laser wavelength of 532 nm

A compromise between maximum transmission coefficient and penetration depth was chosen in this study with the angle of incidence set at 73˚ giving a penetration depth of 108 nm (Fig. 2.5.2.1), and no beam expansion in the final version of the TIR Raman set-up, since the laser output power of the original laser beam was sufficiently large to provide the required energy density at the focused sampling spot, without beam expansion, thus keeping the N.A. of the focused beam at 0.11, with minimal dispersion at the air-silica and silica-water interface.

2.5.3. Applications of Raman spectroscopy in TIR mode

Solid-liquid interfaces, in particular dielectric solid surfaces in contact with an aqueous solution containing the molecules or mixtures of interest, are most suitable for TIR Raman studies of molecular adsorption behavior. The water molecule itself is a poor Raman scatterer (low Raman scattering cross section) and Raman signal contribution from the water molecules in the bulk is, if not avoidable, controllable. The signals arising from water in the bulk and also from silica at the interface are distinctly different from the molecules at the interface and can be subtracted from overall raw Raman spectra. TIR Raman makes an excellent tool for in situ analysis of molecules that contain vibrational normal modes in the high-frequency region, i.e., C-H stretching mode, and adsorb as mono-or bilayers at the interface.

Alternatively, TIR Raman studies at the silica-air interface provide more flexibility in terms of sampling geometry and settings. The incident angles for probing the solid-air

interface can be chosen with respect to the refractive index ratios, without too much concern of the probing depth, as shown in TIR Raman analysis of ultra-thin films at the silica-air interface. At extremely low film thicknesses, the refractive index of the film may have to be factored in, but will lead to only small external interferences and no damage to the sampled material.

2.5.4. Limitations of TIR Raman spectroscopy

One of the major disadvantages of TIR Raman arises from the penetration depth dependence on the incident beam geometry. Any attempt to maximize the transmission coefficients to increase the scattering intensity leads to increased probing depth and loss of surface specificity. The surface specific aspects of this technique can be controlled by choosing adequate sampling geometries, as discussed in the previous sections, but it cannot provide the surface specific properties of purely surface specific techniques, i.e., SFG.

Liquid media involving organic solvents are not suitable for TIR Raman studies as the solvent molecules themselves exhibit strong Raman scattering with too much interference with the molecules of interest. Solid and non-dielectric surfaces, i.e. metals, and other light adsorbing materials, are equally unsuitable, since the evanescent field effect depends on the dielectric properties of both the incident and transmitted medium.[75]

Strong interference from Raman scattering modes originating from the substrate or TIR element itself may also pose some limitations on the suitable frequency range, i.e., strong Raman scattering signals in the low frequency region observed in quartz-based dielectric material. Quartz or modified quartz, in particular IR grade fused silica generates intrinsic Raman scattering from the Si-H, Si-O-Si vibrational modes, that scatter in the low frequency region, and make a good spectroscopic analysis difficult.

Chapter 3: Thermodynamic and Kinetic Properties of Surfactants at Metal Oxide-Water Interfaces

3.1. Surfactant properties and interfacial phenomena

Surface active agents (surfactants) are amphoteric and amphiphilic organic compounds paired with inorganic or partially inorganic counterions. They are classified as cationic, anionic, non-ionic, and zwitterionic surfactant types, depending on the charge of the surfactant headgroup.[82] Their effects on solution and interfacial properties could be described as follows: interfacial surface tension modulation, solubilization of critical compounds, emulsion stabilizer and emulsion breaker,[83] surface wettability (i.e., oil wetting vs. water wetting),[5, 84] and control of surface specific chemical processes by modulation of the solid surface. Cationic surfactants find application in areas where interfacial property changes are intended due to surfactant adsorption to hydrophilic or charge neutral surfaces.[15, 55, 85-88] The more soap-like anionic surfactants are favored in areas where favorable interaction with hydrophobic and positively charged surfaces is required.[44, 89] Besides their use in pure form, the most common applications involve binary mixtures of cationic-non-ionic compounds, frequently as multi-component mixture.[90]

This section describes the evaluation criteria of the principal features and physico-chemical properties of surfactants that typically consist of a hydrophobic tail, i.e., a non-polar alkyl chain, containing between twelve and eighteen carbon atoms, and a charged hydrophilic head group. The head groups are frequently based on the highly water

soluble and polar trimethylammonium cation, or the negatively charged sulfate or carboxylate anions. Other head group types may involve heterocyclic nitrogen containing components, i.e., pyridinium, imidazolium, or pyrrolydinium and their derivatives.[91-93]

3.2. Adsorption of anionic surfactants

Anionic surfactants that are closely associated with soaps and soap-like properties are characterized by a negatively charged head group. The most common head group types include carboxylates as salts of alkanoic acids, i.e., sodium dodecanoate, and sulfonate or sulfate, i.e., in sodium dedecylsulfate (SDS). These anionic surfactant types preferentially adsorb at metal oxide surfaces that are positively charged at the typical pH conditions of 7 – 10. In general, there might be some differences in terms of adsorption kinetics, aggregates shape found at the surface, and differing adsorption mechanisms that are dictated both by the surfactant head group property and by the intrinsic charge and surface specific properties of the substrate itself. Alumina, hematite (α-Fe_2O_3), and zinc selenide are known to show attraction for anionic surfactants, with the extent of adsorption behavior strongly depending on the actual pH of the experimental conditions, [44, 89, 94] resulting in differing adsorption kinetics and adsorption mechanisms. Studies of SDS by FTIR and ATR showed fast adsorption kinetics with the more hydrophilic hematite surface vs. slow adsorption rates at the hydrophobic zinc selenide surface that enhanced electrostatic attraction as the dominating adsorption mechanism at low surfactant concentrations, whereas the hydrophobic effect was most pronounced at higher

concentrations. In contrast, the hydrophilic hematite surface seemed to favor adsorption by anion exchange with self-assembly of the surfactant molecules at the surface.[44]

Sodium laurate, containing a carboxylate group, also studied by vibrational spectroscopic techniques, indicated strong pH and concentration dependent adsorption behavior at the hematite surface.[89] The adsorption isotherms showed only two adsorption regions, that were characterized by a linear adsorption slope in the low concentration region up to the CMC, with an adsorption plateau being reached at the critical micelle concentration in the bulk phase.[89] The prevailing adsorption mechanisms were a combination of inner sphere monodentate and outer hydration sphere shared chemisorption, as confirmed by in-situ FTIR and ex-situ XPS measurements.

Anionic surfactants are not typically found as adsorbents on negatively charged silica interfaces, although research studies claim that adsorption of anionic surfactants is feasible in co-adsorption with non-ionic surfactants.[95] In this case, the non-ionic surfactant, i.e., Triton X100, adsorbs at the silica-water interface first, and the resulting screening of the intrinsically negative charge of the silica surface allows subsequent adsorption of the anionic surfactant as part of a mixed micelle formation. However, increasing the concentration of the anionic surfactant above a certain threshold level usually results in unfavorable adsorption conditions for both non-ionic and anionic surfactant.[95]

3.3. Adsorption of non-ionic surfactants

Non-ionic surfactants, frequently used as co-surfactants in binary or numerous variations of mixed surfactant media, show strong affinity to both hydrophobic surfaces, that are made from or coated with polymeric material,[86] steel,[96] alloys,[97] and also to some hydrophilic surfaces, as demonstrated in a competitive adsorption study on silica.[59] Electrostatic attraction, as found with ionic surfactants at low concentrations, is not the primary adsorption driving mechanisms for these uncharged types of surfactants; The adsorption of the pure non-ionic surfactant takes place via H-bonding between the surfactants' ethoxylated groups and hydrogen accepting sites at the surface, and in most cases, the hydrophobic effect due to the non-polar tail of the surfactant. Adsorption of pure non-ionic ethoxylated nonyl phenols on charged surfaces, i.e., alumina, has not been observed, but occurs in a mixed surfactant system in the presence of a cationic surfactant.[98] However, in binary systems, competitive adsorption of cationic and non-ionic surfactant takes place where the surface properties and also the alkyl chain lengths relative to each other dictate which type of surfactant is dominating at the surface, and the final surface configuration. In case of extremely different alkyl chain lengths, bi-layer type of adsorption structures are found, with the benzyl function of the cationic surfactant intercalating between the alkyl tails of the non-ionic surfactant whose head groups are in close contact with the surface and the hydrophobic tails reach into the aqueous medium.[15] Under these conditions, both surfactants adsorb favorable with synergistic effects. Ultimately, the exact co-adsorption mechanism is controlled by the structure, head group type, and geometry of all surfactants contained in the mixture. An additional hypothesis,

confirmed by experimental studies involving surface charge reversal and zeta potential measurements, claims reduced adsorption of the cationic surfactant, when its head group is smaller than the head group of the non-ionic type.[99] The larger head group of the non-ionic surfactant takes up space at the surface, simultaneously shielding the positive charge at the surface, and thus reducing the electrostatic attraction between the surface and the cationic surfactant, leading to reduced cationic surfactant adsorption.

Micellar structural changes in the aqueous phase due to cationic and non-ionic surfactant mixing will also affect the overall adsorption and structural arrangement of both participating surfactants, as shown in prediction models by Clint's thermodynamic equations, assuming ideal behavior,[99] that appears to be valid within a given range of surfactant concentration, and surfactant alkyl chain length of up to 16 carbons. Adsorption isotherms of non-ionic surfactants were frequently based on Freundlich isotherms, in particular, for adsorption on metal surfaces.[96]

3.4. Adsorption of cationic surfactants

Cationic surfactant adsorption to solid surfaces appears to be limited to hydrophilic surfaces with an intrinsic negative surface charge, i.e., quartz, modified quartz and related materials.[4, 86, 88, 100-102] They do adsorb at modified silica surface with hydrophobic character, however, with modified thermodynamic and kinetic properties.[15] These surfactant types are extensively used as co-surfactants, additives and corrosion inhibition intensifiers in 2˚ and 3˚ oil recovery processes.[103-107] However, attempts to promote

adsorption to metal oxide surfaces with intrinsically positive charge have not been successful. Adsorption has been reported, however, to non-polar surfaces, i.e., octadecyltrichlorosilane (OTS) coated silica-water interface, that is also part of the present study, where adsorption is not initiated by electrostatic attraction between the negatively charged surface and the cationic surfactant head group, but depends primarily on the hydrophobic effect arising from the interaction of the polar aqueous phase and the non-polar alkyl-chain of the surfactant. Adsorption behavior of cationic surfactants, in particular, cetyltrimethylammonium bromide (CTAB) and its related homologue, cetyltrimethylammonium chloride, have been extensively studied as model compounds, to identify their adsorption kinetic and thermodynamic properties, the modifying effects of various monovalent and divalent electrolytes on their adsorption properties, and their aggregate structures. It is generally accepted that the adsorption of cationic surfactants is initiated by the electrostatic attraction between the positively charged head group and the negatively charged silica at very low surfactant concentrations. At higher concentrations, the adsorption is driven by the hydrophobic effect whose magnitude, again, depends on the hydrophobic character of the surfactant structure, determined by the nature of the head group and its effective surface area, the alkyl chain length, solution ionic strength, and on the surface property itself.[4, 86, 98, 108]

The head group size determines to some extent the adsorption kinetics or rates of adsorption where a small symmetric head group, i.e., trimethylammonium, promotes faster adsorption kinetics, due to its small interfacial area, as compared to bulky head

groups, i.e., benzyldimethylammonium, that occupies a relatively large surface area and hydrodynamic radius.

3.5. Association mechanisms of surfactants in solution

Cationic surfactants, like other types, favor two physico-chemical processes: aggregate formation in aqueous solutions,[109, 110] and adsorption to solid surfaces, if the surface properties meet the criteria for favorable adsorption.[4] The tendency to form aggregates is strongly influenced by the length of the hydrophobic, non-polar tail or alkyl chain, the nature of the charged head group, and addition of electrolytes. The head group is known to remain in contact with the surrounding water molecules, and does not contribute to the energetics of micellization. However, its nature plays an essential role in what occurs during the aggregation process, because the head group size and its interaction with the surrounding molecules strongly influences the size and shape of the aggregates.[111]

Increasing the alkyl chain by adding additional methylene groups decreases the CMC value and favors larger aggregation numbers or the packing density.[100] The increase of the hydrophobic portion of the surfactant increases its hydrophobic character and thus its tendency to aggregate into a more energetically favorable aggregate geometry that results in reduced internal energy, described as the Gibbs free energy of micellization. Every methylene group, that can be transferred from the polar aqueous solvent into the inner core of a micellar structure and removed from exposure to the solvent molecules, results in additional free energy of micellization estimated to be approx.. -2.2 to -2.4 kJ/mole for

each methylene that is transferred.[98] The presence of an additional hydrophobic benzyl ligand substituted for the methyl group at the cationic head, accounts for the equivalent of 3 to 3.5 methylene groups[112] added to the hydrophobic portion of the surfactant, thus further increasing the hydrophobic nature of the surfactant, and also the hydrophobic effect, but not contributing to the energy of transfer from polar solution to the micelle core, since the ligand itself is not considered a part of the hydrophobic tail and thus of the micellar core.[93] This energy transfer of the hydrophobic portion from the polar solvent into the micellar core is the only negative thermodynamic contribution to the energy lowering effects of the micellization process, [108] implying that all other energy terms, considered positive, must be kept small, to give an overall negative Gibbs free energy of micellization. The Gibbs free energy of the complete system, solid -, water -, and surfactant aggregate phase, establishes a minimum energy position at equilibrium conditions that can be described by the following expression related to the chemical potential:

$$\mu^{\circ}_g + kT \ln X_g = g\,[\mu^{\circ}_1 + kT \ln X_1] \qquad (3.5.1)$$

where μ°_g is the standard chemical potential of a surfactant aggregate that contains g numbers of surfactant monomers, and X_g and X_1 represent the mole fractions of the aggregates in solution and the mole fraction of monomeric surfactant. In other words, the chemical potential of the aggregate is equal to the chemical potential of the monomers in solution at equilibrium condition. The number density of surfactant molecules that form the aggregates vary with the conditions and depend on surfactant type, polarity or ionic

strength of the solvent, presence of other charged species and surfactant concentration. The term X_{CMC} describes the specific surfactant concentration at which a certain fraction of the surfactant molecules form stable aggregates, measurable by several techniques, and represented by trend changes in a measured property, i.e., conductivity. It is generally accepted that this expression represents the equilibrium position where the number density of monomers is equal to the number of surfactant molecules present in aggregate form. The critical aggregate formation, termed as N_{agg}, is the lower bound for aggregation, the term X_{opt}, the energetically optimal aggregate density, with the CMC being the average equilibrium concentration.[108] The CMC is predicted by the following empirical expression:

$$\text{Log CMC} = a - nB \qquad (3.5.2.)$$

where the constant "a" relates to head group properties, i.e., polarity, charge, and solvent compatibility, and n and B refer to the number of methylene groups and nature of the hydrophobic tail, respectively. Eq (3.5.2) applies to most conventional monovalent surfactants that comprise a straight alkyl chain and common headgroups.[93, 113] The expression needs modification, when either head- or tail group deviate from the typical surfactant geometry; new simulation tools have been developed for CMC prediction,[114] but in many cases, the CMC and related properties are experimentally determined, in particular, for newly developed surfactant types whose size and composition deviates from the conventional forms, such as pluronic surfactants, gemini and zwitterionic surfactants, and for multi-component mixtures.[41, 109-111]

Surfactant aggregrate formation tendencies in solution, and their most likely shapes that include spherical, globular, and rod-like micelles (Fig. 3.5.1), have been extensively studied with the objective to define the criteria that control a particular micellar structure.

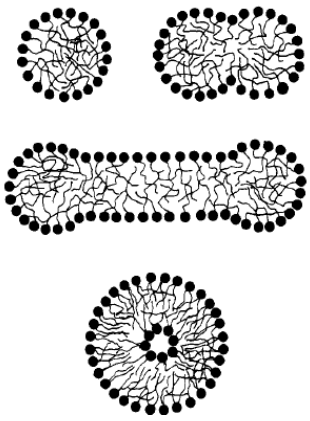

Fig. 3.5.1: Proposed surfactant micelle structures**:**

adapted from:
Nagarajan, R.; Ruckenstein, E Langmuir, *Vol.* 7, *No. 12, 1991* 2935

The preferred aggregate shape in solution is the form that provides the most efficient energy lowering structure and depends on the exact nature of the surfactant and its interaction with the surrounding solvent molecules. For example, studies related to cetyltrimethylammonium bromide or chloride, two of the most common cationic surfactants, suggest that the most likely structure at the micelle formation stage is a spherical shape in solution, but at the interface, may transform to an elliptical shape or rod-like structure. Extension of the hydrophobic tail to fourteen or more carbon numbers is predicted to result in structural transitions to globular or more elongated micellar structures.[108, 115] Studies related to the structure-micelle-relationship also point towards

the possibility of a 2nd CMC that has been observed with benzalkonium derived cationic surfactants and, in particular, with fourteen or sixteen carbon atoms in the hydrophobic tail, or in binary mixtures containing these compounds at extremely high concentrations.[93] The 2nd CMC term is actually a different way of describing the process of micelle restructuring to accommodate changing surroundings. Its values, as reported in literature, however, have mostly been obtained by techniques, i.e., light scattering (LS), requiring addition of a background electrolyte, which again, will affect the equilibrium position and the micellization behavior of the surfactant. In case of benzyl being substituted for a methyl group at the ammonium head, it presumably accounts for an equivalent of three methylene groups,[93] which makes the surfactant type under study prone to showing aggregation properties that deviate from the conventional surfactant behavior. The reasoning found in literature is based on measured changes of surfactant related properties in solution, i.e., conductivity, and further related to simultaneous changes of micellar structure from more spherical to rod-like aggregates. However, some theoretical predictions frequently emphasize that micelle structures found in the bulk do not necessarily represent the same form at the interface, whereas others point out that the bulk structures reflect strongly the interfacial structure.[111]

In general, several parameters influence the micellar structure, i.e., concentrations below or above the CMC, alkyl-chain length, head group type, and, in particular the counter ion and its shielding effects of the charged head group. Alternative expressions for the Gibbs free energy equations for micellization and adsorption are found as follows:

$$\Delta G^{\circ}_{mic} = \mu_{surf/mic} - \mu^{o}_{surf/soln} = RT \ln CMC \quad (3.5.3)$$

It is simply a variation of above eq (3.5.1) also represented as:

$$\Delta G^{\circ}_{mic} = (2-\alpha)\, RT \ln \chi_{CMC} \quad (3.5.4)$$

The Gibbs free energy of adsorption can be derived from the adsorption constant under equilibrium conditions as:

$$\Delta G^{\circ}_{ads} = -RT \ln K_{ads} \quad (3.5.5)$$

Eq (3.5.3) describes the general relationship between the free energy of micellization in solution and the CMC that is simply the difference between the chemical potential of the surfactant in the micelle vs. its standard chemical potential in the solution.[82, 116] When using the term X_{CMC} (mole fraction of surfactant at the CMC), one makes the assumption that the standard state and the chemical potential are related to the pure surfactant, but physically, it is a totally hydrated state with always some hydrocarbon-water interfacial area left.[111] More detailed thermodynamic relationships include the standard enthalpy and entropy change defined as:

$$\Delta H^{o} = - RT^{2} (\partial \ln cmc/\partial t)_{P} + RT^{2}/n\, (\partial \ln X_{mic}/\partial T)_{P} \quad (3.5.6)$$

$$\Delta S^{o} = (\Delta H^{o} - \Delta G)/T \quad (3.5.7)$$

The above expressions relate heat enthalpy and temperature effects on the CMC, and thus provide information on heat enthalpy or entropy contributions in the micellization process. The classical assumption was that the breakdown of the water structure surrounding the surfactant monomers is the principal contributor to ΔS^{o}, giving a positive

value. Later studies by Evans corrected this statement by concluding that the overall entropy change is negative due to the transfer of surfactant molecules from water into the micelle, which frees up the water molecules and allows re-establishing of the original hydrogen-bonded water structure.[111]

The expression in eq 3.5.3 for the Gibbs free energy of micellization does not take into account the degree of association or dissociation of the counter ion.[117] A modified eq (3.5.4) contains a second parameter "α" that corrects the original expression related to the phase transfer of charges from solution to micelle by adding an additional parameter "α". This expression refers to a monovalent surfactant, i.e., one single charge on the head group at the surfactant molecule, accompanied by a monovalent counter ion of opposite charge. The "α" parameter, typically in the range of 0.2 to 0.5, is surfactant type dependent and needs to be experimentally determined; it defines the effects of the counter ion in terms of valency, hydration sphere, and affinity or degree of binding to the cationic head group.[111] Conductivity or conductance measurements are usually carried out to determine the degree of counterion association, but the results reported in literature vary, partly because of uncertainties related to the activity coefficients that should be applied for the counterions.[118]

The most common techniques to determine the relevant parameters for predicting the micellization process of a given surfactant and determining the concentrations that correspond to the critical micelle concentration (CMC), are surface tension and/or conductivity measurements. The resulting isotherm curves from surface tension

measurements are fitted to extract the CMC, and the maximum surface coverage at this concentration.[110]

Eq 3.5.4 relates the Gibbs free energy of adsorption to the adsorption constant K_{ads} that can be derived from experimental studies, i.e., adsorption isotherms,[119] as discussed in the following section. In a three-phase system consisting of surfactant, solution, and solid surface, adsorption of the surfactant is observed along with micellization as a parallel and competing process for lowering the Gibbs free energy of the system. The exact Gibbs free energy can be determined only, if the standard state of the surfactant is known. An alternative approach is to determine the change of the Gibbs free energy due to adsorption effects, as has been done in this study.

3.6. Temperature effects on surfactant solubility and aggregation

A minimum temperature range, typically around room temperature up to 40˚, is required for a surfactant-solvent system to allow for solubilization of surfactant monomers in solution and for surfactant monomers to form aggregates.[89, 119] This critical temperature, usually referred to as the Krafft point, must be attained to transfer lyotropic surfactants from a solid or crystalline state into the solubilized state. Beyond this critical point, temperature effects may enhance or attenuate a prevailing mechanism, i.e., increased temperatures may favor transfer of the surfactant tail from the aqueous phase into the micellar core affecting both ΔS and ΔH, possibly in opposite directions.[120] Surfactant solubility in water and the entropy change of water itself may be the main contributor to

the overall net free energy of micellization in certain surfactant-solution systems at low temperatures, whereas at elevated temperature regions the contributions come from the free energy gain from the transfer of monomers from solution into the micelle.[120]

3.7. Effects of counter ion and electrolyte on surfactant adsorption properties

The surfactant molecules carrying one charge at the head group, are accompanied by a counter ion of the same valency but with opposite charge. In case of cationic surfactants, the counterions can be simple halides, i.e., chloride, bromide, iodide, whereas anionic surfactants are typically paired with monovalent metal ions, i.e., lithium, sodium, potassium. The size (ionic radius) of the counterions as well as their hydration shell influence their affinity to the head group of opposite charge, their charge screening effectiveness, and the CMC of a given surfactant. It is well documented that halide ions decrease the CMC in the order of I^-> Br^-> Cl^- for cationic surfactants,[2] and in the order Li^+ > Na^+> K^+ for anionic surfactants.[121, 122] For example, in case of benzyldimethyldodecylammonium chloride, the CMC is reported as 8.8 mM whereas the CMC decreases to 5.6 mM for the same surfactant with bromide as the counter ion that has a higher affinity towards the charged head group as compared to chloride. The generally accepted theory is that the smaller halide anion chloride is fully hydrated, does not bind as tightly to the headgroup as the larger less hydrated bromide anion, or the even larger iodide.[123] The less hydrated ions show higher affinity for the headgroup with more

efficient shielding of the head group charge that result in higher aggregation number (larger packing parameter), and possibly a smaller size micelle.

Addition of mono- or divalent salts, preferably of the same type as the surfactant counterion, typically results in enhanced adsorption kinetics with increasing adsorption constants proportional to the amount of the additive. Along with faster adsorption rates, a reduction of the CMC and the surface tension relative to the pure compound is observed, as well as changes of the surface excess.[2, 5, 87, 97, 124] Research studies have shown surface excess modulation that resulted in increased adsorption in the presence of an added electrolyte proportional to the concentration of the salt. Other studies, however, demonstrated the lowering of the surface excess as compared to the pure surfactant.[87, 102] The electrolytes screen or attenuate the repulsive headgroup charge, and simultaneously increase the polarity of the solvent that enhances the hydrophobic effect, and the salting in or salting out effects. Salting out, in this context, would refer to the monomer and the electrolyte competing for association with the water molecules and favor micellization, whereas, salting in would describe enhanced surfactant-water interaction.[125] This effect is also related to the polarity of solvent relative to the polarity of the solute; for example: increasing polarity of the solvent by increasing the ionic strength increases the solubility of a polar solute in the liquid, but leads to repulsive effects for a less polar or non-polar solute.

Divalent metals have shown affinity towards silica surfaces under certain favorable conditions with silica surface binding rates and energies of adsorption that depend on the

concentrations of the metals and the background electrolytes used.[13, 126] Research data that are related to the silica surface charge modulating effects of metal chloride salts show varying results that range from further increasing the intrinsic negative charge by surface silanol deprotonation and disruption of the water structure at the surface to generating a positive net charge at the bare silica surface, due to specific adsorption of the metal ion.[127]

In context with electrolyte addition, the expression for CMC prediction and aggregate formation is given by:

$$\log CMC = a - b \log C \quad \text{for ionic surfactants} \tag{3.7.1.}$$

or alternatively expressed in exponential form:

$$CMC = Conc * e^{a-b} \tag{3.7.2.}$$

with "a" and "b" being surfactant-electrolyte specific constants. Addition of magnesium chloride, as shown in this study, does appear to affect the initially negatively charged surface properties, leading to surface charge neutralization, whether by non-specific or specific adsorption to the silica; development of positive charges at the bare silica surface following specific adsorption of divalent metals at the silica-water interface, could not be confirmed in this work.[122] However, the magnesium ion appeared to disrupt the water structure in the electrical double layer, as shown by an offset of the Raman spectral baseline in the frequency region of the less-structured, liquid-like vibrational modes of the water molecules.[128, 129]

3.8. Micellization and adsorption kinetics

Evans and Ninham[130] made attempts to describe the kinetics and mechanisms of micelle formation in the early 1980's by proposing a closed association model based on phase separation and strong association with the counterions from the relation:

nZ = micelles, where the equilibrium constant is defined as:

$$K = \frac{[\text{micelles}]}{[\text{monomer}]^n} = \frac{k^+}{k^- / n} \qquad (3.8.1)$$

where activities have been replaced by the concentration, and "n" stands for the number of monomers in the micelle, with a value for n such that K is at its maximum. Eq (3.8.1.) relates the equilibrium constant to the rate of transfer into the micelle, k^+, and exit rate k^-, and the average aggregation number n. It includes the competing mechanisms of bringing the hydrocarbon chains in close contact with each other, and away from the water molecules, without putting the head group charges too close. The general rules of packing and the predicted packing structures are deduced from head group geometry, symmetry, and hydrodynamic radius, and the length of the alkyl chain: the packing parameters for the respective shapes are:

The ratio of $V/(A_{o*}\ lc)$ = 1/3 for spherical, and ½ for cylindral, and = 1 for a bilayer structure. The parameters contained in the above expressions are defined as follows:

$V = R^n * \text{Area (head group)}/3$, with R^n describing the hydrodynamic radius of the monomer, A_o the head group surface area, and l_c the effective alkyl chain length. The overall guidelines for optimum micellar packing might be summarized as: An all-trans and ordered configuration of the hydrophobic alkyl chain would be energetically unfavorable that leads to a large hydrocarbon-water interfacial contact area; the most likely configuration in a micelle are deformed alkyl-chains with minimum hydrocarbon-water contact. The packing density is controlled by the balance between short-range repulsive forces and long-range van der Waals attractive forces, and the alkyl chains are found at all possible configurations, with the methyl terminal group not necessarily found at the center of the micelle, but in between the center and the outer micelle surface.[111]

3.9. Co-existing mechanisms of surfactant adsorption at the silica-water interface vs. micellization in solution

Micellization and adsorption to surfaces are two competing processes leading both to lowering of the Gibbs free energy of the surfactant molecules. The aggregate formation tendency and its related energy terms strongly influence the adsorption behavior of the surfactant. It is well established that surfactant adsorption will occur in a three-phase system containing silica as the hydrophilic surface with slightly negative charge of -0.013 C/m^2, the aqueous phase at approx. neutral pH, and a cationic surfactant. The general aspects of the adsorption process are known for most common surfactant-solid systems, but there is still some uncertainty about the exact effects of the head group geometry and electrolytic additives on the adsorption kinetics and thermodynamics of surfactant.

Adsorption isotherms are based on various adsorption models, i.e., Langmuir adsorption, related to monolayer formation, modified Langmuir, and the Freundlich isotherm. Each model is adapted to the adsorption behavior of the respective system. The adsorption isotherms established in this study fit strongly to a Langmuir or modified Langmuir adsorption isotherm, an adsorption model that accounts for the interaction between neighboring molecules at the interface and the resulting change in free energy of adsorption and adsorption constants, as discussed below in section 4.6.

3.10. Surface tension and conductivity measurements

The most common technique for CMC determination are surface tension and conductivity measurements, conducted over the surfactant concentration range of interest in aqueous solution. Depending on the expected information, the measurements cover at least the concentration range across the expected CMC, or may reach from extremely low concentration to concentrations far above the CMC. Surface specific thermodynamic parameters can be found by determining the surface tension (in mN m^{-1} or dyn cm^{-1}) and its change at the water-air interface for a series of relevant surfactant concentrations and relating the gradient in the measurement curve and the change in the slope of the gradient to the maximum surface coverage, according to the following expression:

$$\Gamma_{max} = -\frac{1}{2RT} * \left(\frac{d\gamma}{d \ln[C]} \right)_T \qquad (3.10.1)$$

The value of "2" in the denominator accounts for dissociation of the surfactant into two ionic species in the liquid phase, [C] is the concentration of the surfactant in mol/L at equilibrium at the CMC, converted to mole fraction, and γ the surface tension. The surface excess at maximum or saturation surface coverage is determined from the linear portion of the surface tension slope right before the CMC value in units of $\mu mol\ m^{-2}$, after curve fitting and applying the thermodynamic relationship shown in eq (3.10.1).

Commonly applied surface tension measurement techniques include: (a) pendant drop or pendant bubble method that analyzes the shape of a hanging drop or a bubble at the end of a needle, (b) sessile bubble method where a bubble is floated against the top of a container, (c) Wilhelmy plate method, where a specially designed plate is placed vertically into the liquid and the force required to prevent it from being pulled into the liquid is measured, and (d) the "du Nouy" ring tensiometer method that utilizes a thin iridium ring and measures the force required to pull the ring through the air-liquid interface.[131] The method used in this study was the "du Noüy" ring method that appears adequate for surface tension measurements at the air-water interface.

Alternative techniques to identify the surfactant CMC are conductivity or conductance measurements where the slope/coefficient of the gradient of conductivity vs. equilibrium concentration are determined and the intersection of the two slopes before and after a breakpoint in the measured curve, is used for CMC determination, and the ratio of the slopes determines the additional correction parameter "α", shown in eq (3.5.3).[116] This ionization parameter, or degree of dissociation, cannot be determined

from surface tension measurements implying that surface tension measurement may yield only limited information regarding the free energy of micellization, but gives information on surface coverage at the air-water interface, and of course, the surface tension lowering properties of the surfactant at this interface. Surface tension measurements are further useful for identifying impurities in the surfactant under investigation. Organic impurities lead to anomalous behavior of the surfactant regarding surface tension and possibly CMC lowering effects, that manifests itself by a depression in the surface tension curve right before the CMC.[132] Alcohol impurities, frequently found at trace amounts in the surfactant from the previous synthesis process, are known for their surface tension lowering properties by forming an adlayer at the water-micelle structure. Other organic impurities may have CMC modifying effects by acting as water structure making or breaking agents.[111]

3.11. Adsorption models for adsorption at solid-liquid interfaces

After the onset of adsorption, and initial formation of aggregates in solution and consequently at the interface, the adsorption process is energetically driven by hydrophobic mechanisms, until a maximum is reached characterized by a plateau region in the adsorption isotherm. In case of silica surface charge neutralization by non-polar alkyl chains, or by charged metal salt ions, the electrostatic adsorption mechanism is absent. In this case, the hydrophobic effect is the primary driving mechanism. After admicelles, or bilayer type structures are formed, and adsorbed at the respective

surfactant solution concentrations, no further adsorption is expected, even if the surfactant concentration in solution exceeds the CMC. A model showing the possible formation of hemimicelles, admicelles, and bilayered structures is presented below:

Some literature sources point towards the possibility of a 2nd CMC developing at high concentrations,[133] or, in case of long alkyl chain surfactants that contain an aromatic ring ligand at the head group, also at lower concentrations (3x CMC), as well as formation of a second adsorption layer and micellar restructuring in solution.[87] Several studies on surfactant adsorption behavior also show the possibility of decreasing surface excess beyond the CMC equilibrium concentration.[100]

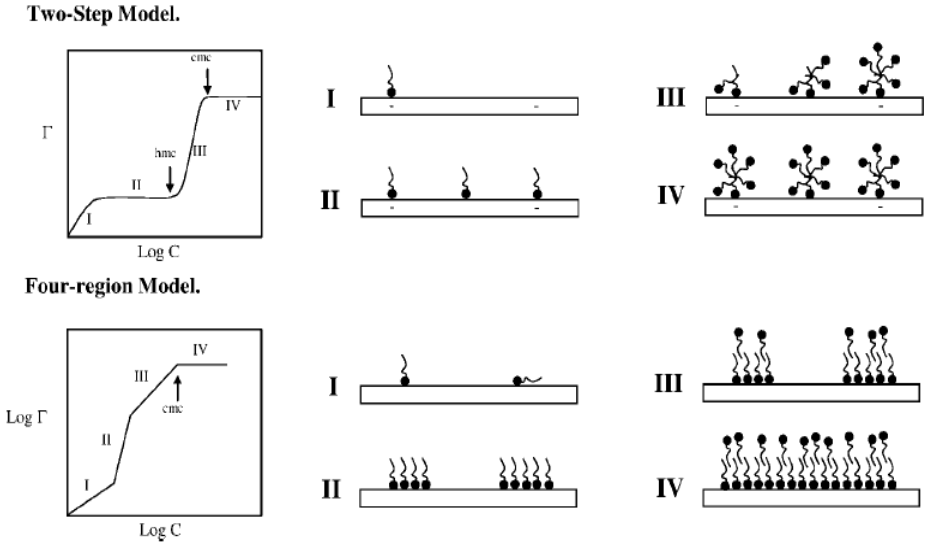

Fig. 3.11.1: Proposed surfactant adsorption process at solid-liquid interfaces

Adapted from:
Somasundaran, P.; Fuerstenau, D. W. *J. Phys. Chem.* **1966**, *70* (1), 90–96

One method available for determining the adsorption isotherm of a given surfactant-solid system is the traditional depletion method. With this technique, the partitioning of the solute between solid and liquid phase at equilibrium conditions is measured over the relevant concentration range.[110] The resulting isotherm curves can then be fitted to the respective adsorption model. In this study, the adsorption isotherms were determined from spectroscopic analysis of the Raman scattering spectra of the relevant surfactant concentrations. The signal intensities of the key vibrational modes, the symmetric methylene and/or the benzyl vibrational modes in the Raman spectra were used as basis for determining the adsorption isotherms that were fitted to a Langmuir or modified Langmuir adsorption model to determine adsorption constants and the interaction energy parameter according the expressions below:

$$\frac{\theta}{1-\theta} = K_{mod} * [C] \quad (3.11.1) \qquad K_{mod} = K_L * e^{g\theta} \quad (3.11.2) \qquad g = n*E/RT \quad (3.11.3)$$

where K_L and K_{mod} define the Langmuir and the modified Langmuir constant and $g = n*E*\theta/RT$ refer to an interaction parameter "g" that includes the number of neighboring molecules n, the surface coverage θ and the interaction energy E. This model has been frequently applied for similar processes where the conventional models, i.e., the pure Langmuir or Freundlich models are inadequate, since the adsorption behavior of the studied species does not only depend on the available surface sites, [134] but also on the interaction with the neighboring molecules.[82, 135-137]

The above equations are based on more detailed background theory as described below for the Langmuir adsorption model for monolayer coverage without and with interaction between neighboring surfactant molecules:[138]

For a Langmuir type adsorption mechanism, the Langmuir constant can be expressed as:

$$K^{-1} = \exp [-\Delta\Delta_{ads}f/RT] \qquad (3.11.4.)$$

The Langmuir constant can be extracted by plotting its inverse:

$\theta^{-1} = 1 + K^{-1} + X^{-1}$ (X is the mole fraction of surfactant in the liquid phase)

with the slope $= K^{-1}$, or as a logarithmic linearized expression:

$\ln (\theta/1-\theta) = \ln conc + \ln K$ and the intercept is: $\ln K$

The modified Langmuir (also known as Frumkin-Fowler Guggenheim model)[82] takes into account interaction between neighboring molecules; it can be expanded to a 3-D lattice mode with more than one adsorption layer. In this study, it is assumed that a single layer (hemi-micelle) or double layer (ad-micelle or bilayer maximum) is present:

The expression can be further expanded to include the Boltzmann factor:

$$(\theta/1-\theta) = (x/1-x) \exp\left[- \frac{\Delta\Delta ads * f}{RT} + 2\lambda o\theta - 1\lambda\theta \right] \qquad (3.11.5.)$$

λ may contain a subscript or index that refers to a lattice matrix specific weighting factor. In case of cooperative adsorption mechanisms, increased adsorption is observed due to favorable lateral interaction between adsorbed molecules, since the first molecule

adsorbed promotes the subsequent adsorption of the 2nd; it may be due to adsorption-induced changes of the surface properties, caused by interfacial changes, or changes of the adsorption sites. Lateral attraction leads to aggregate formation at the interface, which is assumed to occur with surfactant adsorption, and is energetically a compromise between free energy lowering by forming an aggregate vs. the loss of entropy of the surfactant molecules in the adsorbed state. These entropy considerations and its reduction by a given factor are accounted for in a modified expression, also referred to as the Hill expression:

$$(\theta/1-\theta) = (x/1-x)^{g} \exp\left[-\frac{g * \Delta\Delta ads * f}{RT}\right] \qquad (3.11.6.)$$

This factor "g" can be experimentally determined and modeled by plotting the above expression as ($\ln \theta - g\theta$) vs. ln X and relate g to the deviation of the resulting expression from linearity and thus from the standard linearized Langmuir model. A value of $g > 0$, points towards positive interaction, and for $g = 0$, no interaction and the Langmuir model is applicable; in case of $g < 0$, the adsorption behavior is considered to contain a negative interaction energy term, due to repulsive forces. The above expressions do not give linear correlations if applied as written, but can be linearized by adjusting the parameter g and converging on the best correlation.[135, 136, 138]

Within TIR Raman spectroscopy, this kind of adsorption model and analysis applies to two-phase systems, i.e., such as liquid-solid interfaces, where the substrate does not exceed mono- or bilayer thickness and changes of the Fresnel coefficient and refractive index ratio are not expected. In case of multi-layer formation, the model needs to be

expanded to a three-phase system, with the substrate counting as a third independent phase. [74]

Chapter 4: Experimental Design

4.1. Experimental design related to an argon ion laser as excitation source

The initial TIR Raman set-up, with capabilities for both Raman spectral analysis in conventional and in total internal reflection (TIR) Raman mode, used a multi-mode argon ion laser (Innova 318 Series, Coherent Inc.), with three principal wavelengths as the laser excitation source. The center wavelength of 488 nm was chosen as the operating wavelength; it was isolated by dispersion of the three output wavelengths via a Littrow type prism and by blocking the outer wavelengths of 457 and 514.5 nm. This laser system design was used as the excitation source for initial experimental work including the adsorption study of volatile organic compounds at the silica-air interface, the adsorption studies of the ionic liquid 1-butyl-3- methyl imidazolium dicyanamide [BMIM][DCA] and two anionic surfactants, as well as the validation of the TIR Raman set-up with the cationic surfactant cetyltrimethylammonium chloride (experimental layout in Fig. 4.1.1).

The TIR Raman set-up was developed on a 2’ x 1.5’ in-house built laser table platform, encased in a remodeled compartment with openings on the side as required for entrance and exit of the optical light path. The platform, designed analogous to a conventional optical table allowed for placing optical components in the appropriate positions with the necessary height adjustments. Laser and wavelength dispersion optics were positioned next to the compartment at the entrance side, whereas the spectrograph

and detector are located at the exit side. The main components of the complete set-up include on the incident side of the sampling system:

Argon ion laser source, dispersion prism, half-wave plate, anti-reflection coated broad-band and argon ion wavelength specific anti-reflection coated mirrors, beam expansion and beam-blockers, focusing lens, TIR prism, and sample cell.

On the light-collection side the primary components are:

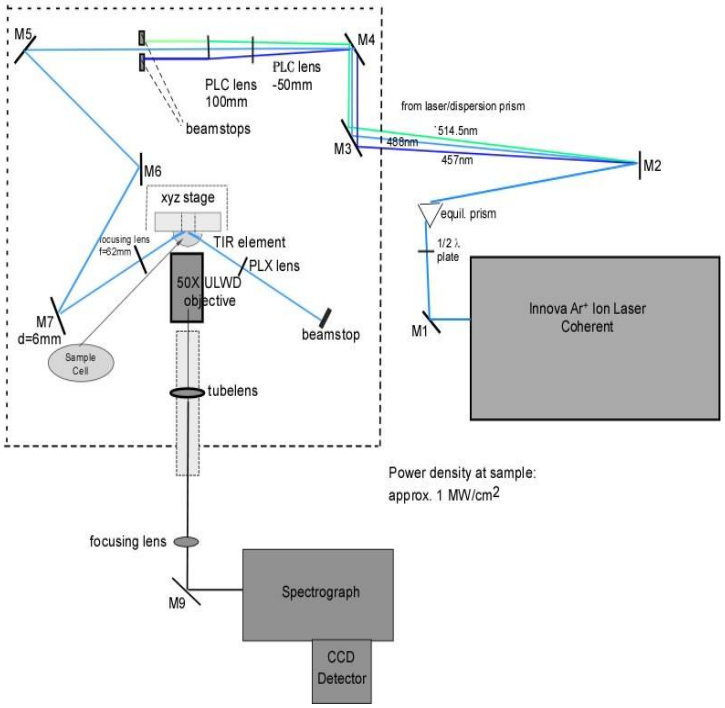

Fig. 4.1.1: Experimental layout of argon ion laser operated in TIR Raman set-up

ultra-long working distance (ULWD), infinity corrected objective for light collection and collimation, and a biconvex lens (f = +200 mm) for focusing; an additional focusing lens is integrated between the primary light collection set-up and the spectrograph entrance,

followed by another broad-band mirror, spectrograph, dispersion grating (HF grating for 488 nm wavelength with a spectral range of 1250 to 3650 cm^{-1}, and detector system (Fig. 4.1.1.)

4.2. Focusing and Raman signal collection optics

Since the argon ion laser model available (318 Series, Multi-mode, Coherent Inc.) has three significant emission lines of 457, 488, and 514.5 nm, the TIR Raman application required separation of the three wavelengths, in order to isolate the center wavelength of 488 nm, that contributed 38% of the total power obtained at the laser head output power. The first instrumental configuration used a Littrow prism (90˚ x 60˚ x 30˚), placed on a flat surface at the appropriate height and distance away from the laser head at an angle of 80˚ from the output laser beam, after reflection off an anti-reflection coated mirror. A wavelength-specific half-wave plate was placed in front of the Littrow prism for converting the vertically polarized laser beam to horizontally polarized light, that would correspond to p-polarized incidence at the Littrow prism in upright geometry. The refractive index ratio of silica-air of 1.00/1.46 provided sufficient dispersion to separate the three wavelengths by 5 mm over a path length of 1 m, and keep all three wavelengths within the diameter of the transmission optics of 1" dia. and block off the unwanted wavelengths of 457 and 514.5 nm at the beam blocker. The final setting at the laser head of 1.0 W gave 220 mW of output power at the focusing lens, after separating out the 488 nm wavelength, blocking off the unwanted wavelengths, and passing through the beam

expansion system and the remaining optics. The laser beam was expanded by a factor of 4 to obtain a larger beam diameter of 12 mm before the focusing lens. The Littrow prism configuration was finally replaced by an isosceles prism (Coherent Inc., estimated refractive index n = 1.8) with improved dispersion and minimal reflectance losses at more favorable angles of incidence (closer to the Brewster condition).

Integration of a beam expansion lens system provides a larger beam diameter at the focusing lens. The resulting small laser spot size on the sample achievable with higher beam expansion factors (i.e., 4x) and small focal lengths of the focusing lens, results in increased energy density on the sample, but with a large N.A. value of the laser beam incident onto the probed surface. It causes excessive dispersion at the silica surface, both at the air-silica incident side and silica-air or silica-liquid interface with deviation of the incident and transmitted beams from the target incident angles; ultimately, it leads to loss of surface specificity due to an electric field probing depth that is higher than the target value, and most likely to lower energy density at the focusing spot than the calculated and theoretical value. This excessive dispersion, also related to the N.A. at the focusing optics, may be even detrimental, as discovered during the developmental stage of the experimental TIR Raman set-up after removal of the beam expansion with simultaneous increase of the output power of the laser excitation source.

The theoretically determined energy density in the final design did not increase as much as expected from the increase in incident laser power, as discussed in the following section. The power density was raised from 220 mW in the 1st design to 440mW in the

final design, but was compensated by the reduction of the laser beam diameter (from initially 12 mm with 4x expansion, then to 6 mm with 2x expansion, and finally 5 mm in the final design without expansion) with relatively small increase in the calculated power density. However, the actual Raman scattered intensity increased by several factors. This phenomenon is attributed to the fact that the initially high power density was either compressed to an extremely small spot, and the total power density integrated over the area covered by the collection objective was not increased. A larger sampling spot matches the field of view of the objective and collection optics, with higher power density when integrated over the entire area of focusing. The second argument is the energy density at the focusing spot was lower than calculated due to excessive dispersion, and also due to unreliable measurements of the power meter. The optimum approach appeared to be a laser energy source that requires no or minimum beam expansion, a small N.A. value, with mild focusing onto the sampling spot, i.e., an effective focal length of 60 – 65 mm for the focusing lens.

A right-angle prism with a flat surface of incidence is less suitable as TIR element, since dispersion effects were even more pronounced, as experienced in the initial experimental design. This right-angle prism was replaced by a hemispherical prism made of IR grade fused silica. The hemisphere provided enhanced flexibility in terms of choosing the incident angles, with lower deviation from the target angles, less dispersion, and minimal losses at the air-silica surface of incidence due to less deviation from the surface normal at the outer air-silica surface irrespective of the angle of incidence at the TIR surface. The sketch below illustrates the potential for increased dispersion and

deviation from the surface normal of the outer rays of the laser beam in connection with a right-angle prism relative to the hemispherical prism and less deviation from 0˚ away from the surface normal at the air-silica incident side, and less dispersion at the TIR interface. Reflectance for this configuration is known to be small; it was determined as 0.02 using the Fresnel reflection coefficient expression,[139] and would drop to zero at the Brewster angle that was determined as 55.6˚ from: $\Theta_B = \tan^{-1}(1.46/1.00) = 55.6^{\circ}$, with no phase shift occurring for plane or parallel polarized light and 180˚ phase shift for perpendicularly-polarized light, but no change of the orientation itself. One additional feature to consider in future design is the use of a curved mirror on the focusing side instead of a flat one, that matches the radius of curvature of the hemispherical TIR element to further minimize dispersion effects.

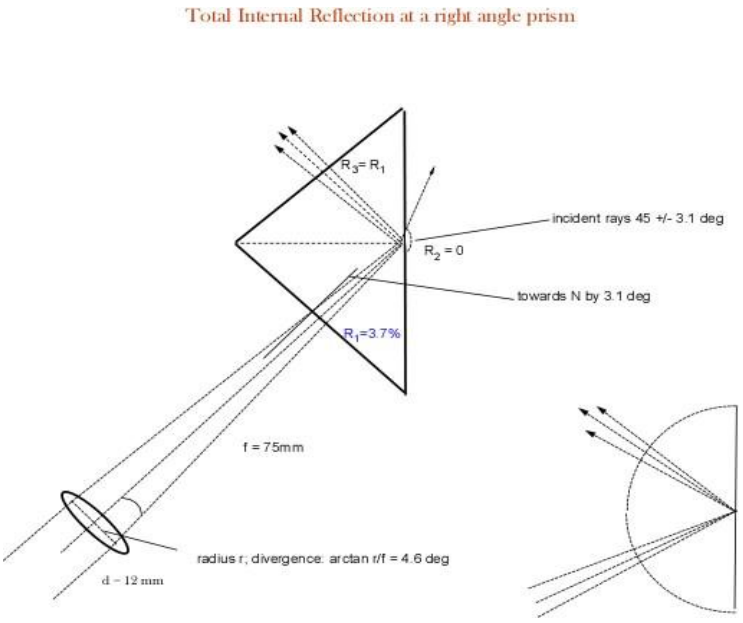

Fig. 4.2.1: Right angle vs. hemispherical dispersion element

The fact that the effective focal length of the focusing lens (f=60 mm nominal) was 63 mm at the hemisphere vs. 67 mm at the right-angle prism is a strong indicator for existing dispersion at both interfaces, and with outer rays from the laser beam being incident outside the surface normal; these effects were more pronounced at the right-angle prism, and increasing with increasing N.A.

The laser beam expansion, based on the Galilean telescope principle, consisted of a pair of suitable lenses that were integrated into the laser beam path and coupled to the beam blocker. The beam expansion factor was determined as follows:

Lens system employed:

+200 mm positive plano convex lens

-50 mm negative plano concave lens

Distance between the two lenses: 150 mm.

The common focal point of the two lenses is the sum of the two focal lengths giving: +200 – 50 = 150 mm. This distance was chosen between the plano concave (f= - 50 mm) and the plano convex (f = +200 mm) lenses to achieve a final and collimated laser beam with an expansion ratio of 4x, determined from the ratio of the two focal lengths 200/50 (from the Thin-Lens-Equation, also known as the Gaussian Lens Formula)[139]

Initial power density before focusing: 220mW = 0.220 J sec^{-1}

Effective focal length of the prism: 63 mm

Beam diameter before focusing: 12 mm

Since this expansion factor of 4x proved to give excessive dispersion and deviation of the focused rays from the actual target angle, the expansion factor was reduced to 2x by modifying the lens pair system, and replacing the +200 mm focal length lens with a +100 mm focal length and placing both at a distance of 50 mm apart, with the concave lens again in front to give:

Expansion ratio: +100/-50 = 2x expansion

The final diameter of the expanded laser beam was determined as 6 mm and used as input to determine the effective focused laser spot size and the effective power density at the sampling spot, after applying the Rayleigh criterion and the appropriate expression for lens focusing of a Gaussian beam that relates the focused spot size to the focal length.[140] For the respective wavelength of 488 nm of the monochromatic beam, and the initial beam diameter, the final new diameter of the focused beam was determined as follows:

$$W_2 = \{1.27 * \lambda_o * f_{eff}\} / w_1 \qquad (4.2.1.)$$

where 1.27 is a constant related to the Rayleigh criterion, λ_o is the wavelength in vacuum, f_{eff} is the effective focal length of the focusing lens and w_1 and W_2 are the beam diameters of the initial beam before focusing and the final beam at the focused sampling spot. The final elliptical sampling spot surface area and the final power density were then determined according to the following calculations:

Final dia. $=\{1.27 * 488 * 10^{-9}\text{m} * 63 \text{ mm}\} / 6 \text{ mm} = 7 \mu\text{m}$

Elliptical spot size: determined from $\pi * r_1 * r_2$

$r_1 = 7/2 = 3.5$ μm and $r_2 = \{r_1 / \sin (90\text{-}73)^{\circ})\} = 12$ μm (from trigonometric considerations with beam incidence of 17˚ away from surface plane)

Area of elliptical focusing spot: $\pi r_1 r_2 = \pi (3.5 * 12)$ μm^2 = approx. 132 μm^2

Power density: $\{0.22 \text{ J} * sec^{-1} / (132 \mu m^2)\} * 10^8 \mu m^2/cm^2 \} = 0.167$ MW cm^{-2}.

A focusing lens with 45 mm effective focal length that was tested for potential increase of the energy density by decreasing the focal spot area, proved ineffective and usage of short focal length lenses was not further pursued.

The initially chosen angle of incidence was as close as possible to the critical angle, i.e., at 45˚ incidence, with the intent to maximize the evanescent field enhancement, as illustrated in chapter 2. This geometry, however, showed its draw-backs in unwanted high angle-dependent penetration depth of the evanescent field into the bulk, unwanted and high dispersion at the surface, and high signal contribution from molecules in the bulk. The angle of incidence was finally chosen at 73˚, with lower penetration depth of 97 nm with 488 nm incident wavelength, or 108 nm with incident wavelength of 532 nm in the final TIR design.

The numerical aperture (N.A.) of this system was determined as:

Effective focal length: 63 mm

Radius of the laser beam before focusing: 3 mm (with 2x beam expansion)

The angle "α" formed at the incident side was determined as 2.73˚ from the divergence in front of the lens:

The angle $\alpha = \tan^{-1}(3/63) = 2.73^{\circ}$

N.A. = n * 2 sin α = 1.46 * 2 * sin 2.73˚ = 0.14

This expansion system appeared most suitable for the experimental work carried out with the argon ion laser, but was omitted in the final experimental design that involved a solid state laser with initial beam diameter of 2.25(±0.25) mm at the laser head, and approx. 4.5(±0.5) mm diameter at the focusing lens, but significantly higher incident laser power, as described in the next section.

4.3. Diode laser system as excitation source – final design

The Argon laser was replaced with a diode pumped solid-state laser (Verdi V-6, Coherent) with emission wavelength of 532 nm that was used as the laser excitation source for all relevant experiments related to the primary research objective - adsorption of cationic surfactants. The laser beam diameter of 4.5mm (or max: 5 mm – assuming 10% relative error – at the TIR focusing lens) was initially expanded, but this approach was abandoned because of a high N.A. value at the focusing spot. The final design does not include a beam expansion option and the laser is sent directly by the appropriate mirror optics to the focusing lens with 63 mm effective focal length and resulting 440 mW power measured before focusing on the sample, at an output power of 0.5 W at the

laser head, as used for the 1st part of the experimental work. The power was raised to 1.0 W for the 2nd part of the study, with resulting 880 mW at the focusing lens. The incident angle of the laser beam at the silica-water interface was set at 73˚ with a penetration depth into the water medium of 108 nm (eq 2.5.1.2.)). This angle of incidence combined with the focusing length of 63 mm before the sample and the actual laser beam diameter gave a N.A. of the focused laser beam of 0.10 (±0.01) with an elliptical spot size of 198 μm^2 (π*4.3 x 14.7) μm^2 and 222 kW cm^{-2} power density on the sample.

The numerical aperture (N.A.) of this system was determined as:

Effective focal length: 63 mm

radius of laser beam before focusing: 2.25 mm (alternative value used: 2.5mm)

"α" angle formed at the incidence determined from the divergence in front of the lens:

The angle $\alpha = \tan^{-1}(2.25/63) = 2.05^{\circ}$

N.A. = n * 2 sin α = 1.46 * 2 * sin 2.05˚ = 0.102 or rounded off to N.A. of 0.11, if a 10% tolerance is included. According to the calculations, the diode laser source, with a smaller beam diameter, provides only marginally higher power density at the sampling spot, but with narrower N.A., that together with higher laser incident power actually resulted in an overall stronger excitation source and stronger Raman scattering intensity. The experimental layout of the TIR Raman, as shown in Fig. 4.3.1, was the final design used for the primary research work related to the adsorption behavior of a cationic surfactant.

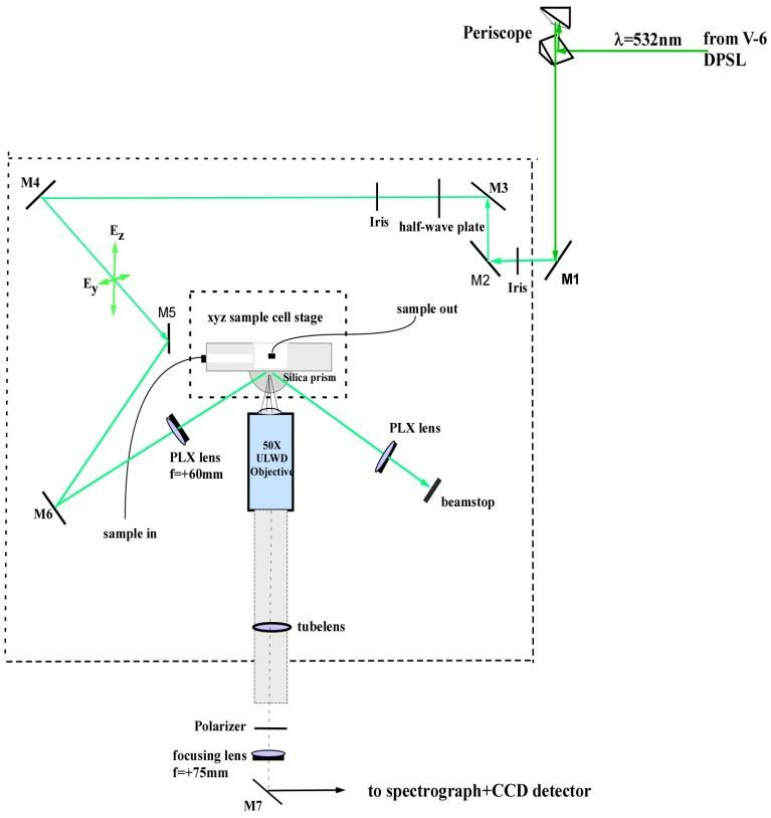

Fig. 4.3.1: Final experimental design and layout of TIR Raman system

The linear relationship between laser output power and collected light intensity of the final TIR Raman set-up was confirmed by a short test that correlated the Raman scattering signal intensity as function of incident power, and verified the relationship between incident angle and the Fresnel transmission coefficient, as discussed in section 2.5.1. A cationic surfactant at known concentration, adsorbed to the silica-water interface, and an octadecyltrichlorosilane (OTS) monolayer at silica-air surface were used as test compounds; the data presented in Fig. 4.3.2. show the signal response of the

dominant CH_2 symmetric stretch of an octadecyltrichlorosilane (OTS) monolayer at the silica surface to variations of the laser output power. The scattering intensities in both S_y and P_{x+y} polarization geometry confirm a linear relationship between incident power and the Raman scattering signals, with collection efficiency in S_y geometry showing a higher signal intensity coefficient vs. P_{x+y}. A comparison of collected signal efficiency as function of acquisition time, however, confirmed that the signal intensity vs. detection or acquisition time is not linear; it depends on CCD or detector specific factors and may be better described by:

$I_{coll} \propto \text{time}_{acq} / \sqrt{a}$

where I_{coll} stands for the collected photons (in counts or counts sec^{-1}), that are inversely proportional to the square root of a detector specific constant.

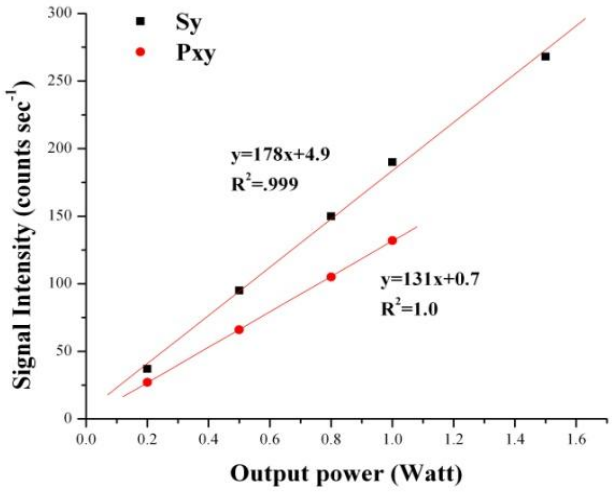

Fig. 4.3.2.: Collected signal intensity (CH_2 ν_s of OTS) as function of laser output power (0.2-1.5 W); angle of incidence: 73˚ - 5 min. acquisition time

The 2nd part of the research study was carried out at 1.0 W laser output and reduced acquisition time of 5 minutes. Increasing the laser power by a factor of 2 (with all other acquisition parameters remaining the same) doubled the intensity of the Raman scattered signals, but reduction from 10 to 5 minutes acquisition time did not reduce the signal intensity by half, with an overall signal increase by approx. a factor of 1.8.

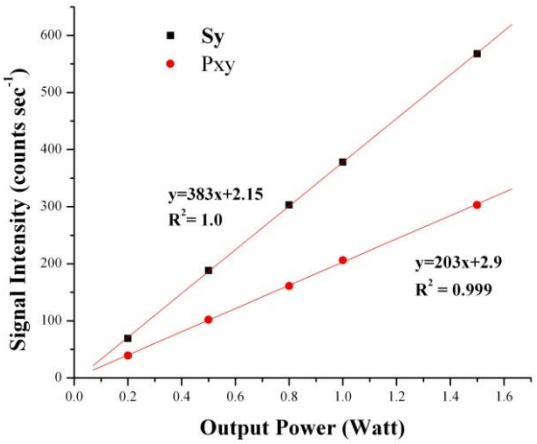

Fig. 4.3.3.: Collected signal intensity (CH_2 ν_s of OTS) as function of laser output power (1.0 W); angle of incidence: 53˚ - 5 min. acquisition time

The graphs above further illustrate the incident angle dependence of the Fresnel coefficient and the evanescent field enhancement. Signal intensities in S_y geometry increased by a factor of 2.15, and by 1.55 for P_{x+y} geometry.

4.4. TIR Raman sampling system – final design

The circular sampling cell (Fig. 4.4.1) was constructed from Teflon® material with an internal diameter of 14.5 mm and a width of 8.5 mm to give a cell volume of 1.23 cm^3. The sample is introduced via a 0.059" dia. bore hole (including the matching fittings, connectors, and Viton® seal rings) at the side wall at mid-height of the cell. It exits at the opposite side, also at mid-height, if a gas sample, or through the top of the cell with liquid samples. The front of the sampling cell contains the TIR hemisphere (ISP Optics) with the flat surface in vertical position, held in position by a Teflon-tape protected metal clamp with an aperture in the center of approx. 12 mm dia. The hemispherical 1" dia. IR grade fused silica prism serves both as the TIR element itself and the silica solid surface. The aqueous solutions containing the respective surfactant concentrations in ultra-pure water (Millipore – 18.2 MΩ) were introduced into the sample cell via 1.5 mm I.D. PTFE lines connected to a peristaltic pump (Lab-Line Peristaltic Inducer) for Raman spectral analysis at stagnation point flow conditions (Fig.4.5.1). The detailed design and flow diagram of the gas/vapor and liquid sampling system integrated into the sample delivery set-up are shown below (Figs. 4.4.1. through 4.4.4.).

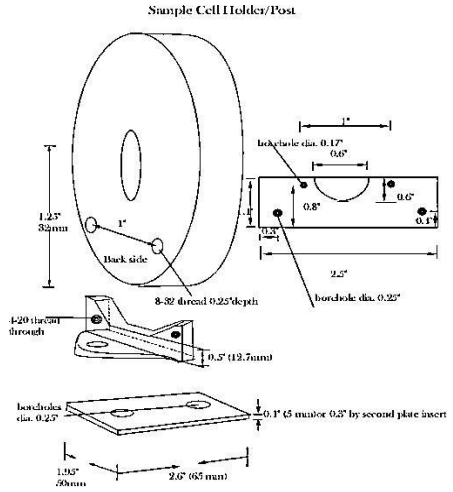

Fig. 4.4.1: Flow Cell Design

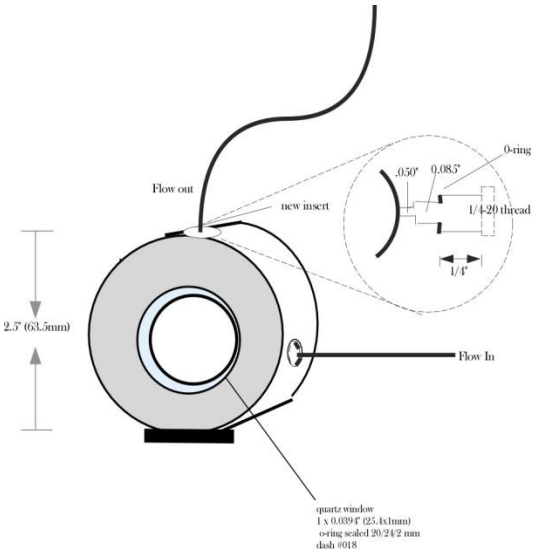

Fig. 4.4.2.: Sample cell – front

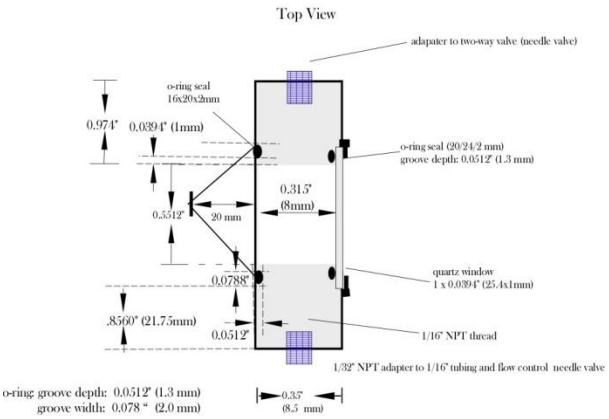

Fig. 4.4.3.: Sample cell - top view

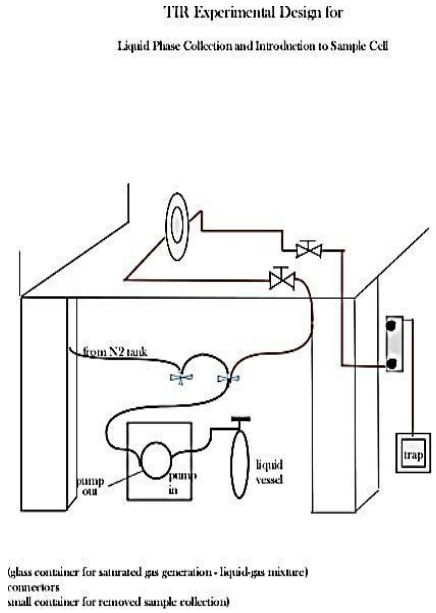

Fig. 4.4.4.: Sampling and delivery system

4.5. Raman focusing and signal collection optics – final design

The Raman signal collection optics consist of a 50X ULWD objective (Mitutoyo, 0.55 N.A., 17 mm working distance) attached at the front of a 250 mm long lens tube, with a 1” dia. bi-convex focusing lens (f= +200 mm), located 230 mm behind the collection objective in the 1” dia. lens tube compartment for collimation of the incoming Raman scattered signals. The collected photons are focused into the spectrograph by a second focusing lens (f = +75mm)

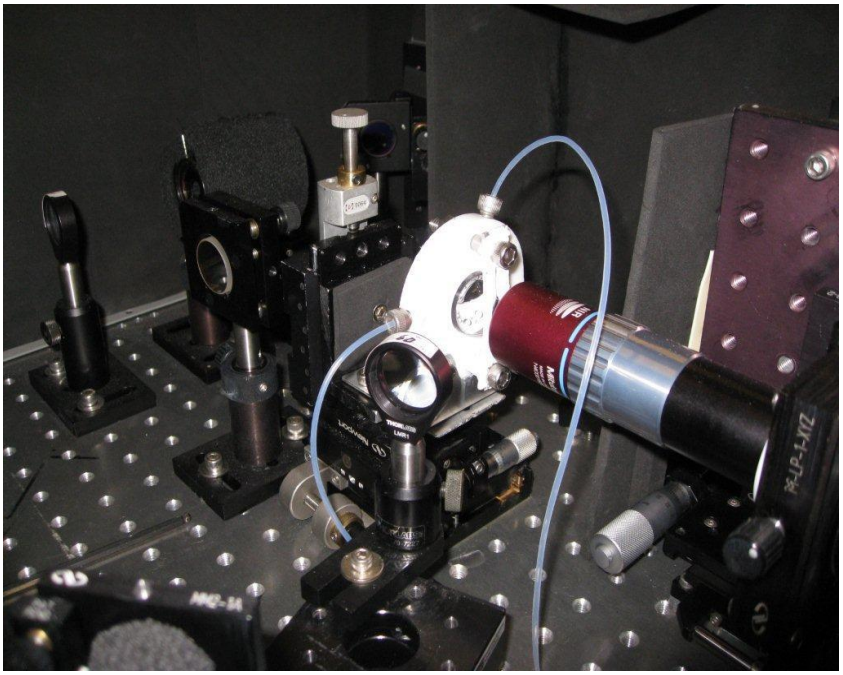

Fig. 4.5.1: Sampling cell and light collection optics

The polarization of the incoming incident laser-beam can be set to horizontally or vertically polarized light by means of a half-wave plate that is placed into the laser beam at the entrance of the TIR set-up. For the kinetic studies and the adsorption isotherms, the

principal orientation at the TIR surface was s-polarization that required re-setting of the incoming horizontally polarized incident light to s-polarized light at the silica surface due to the upright sampling geometry. For specifically S_y polarized Raman scattering experiments, including adsorption isotherms at the hydrophobic silica surface (2^{nd} part of the study), a polarizer was placed between the collection optics and the spectrograph entrance. For p-polarized incident light, chosen for signal intensity ratio experiments, both the half-wave plate and the polarizer were removed, with resulting P_{x+y} sampling geometry.

4.6. TIR Raman detection system

The spectrograph itself contains two pairs of focusing optics. The first pair is located right behind the spectrograph entrance with f=50 mm with a laser line rejection filter for excluding the Rayleigh line of 532 nm. The focused signal is sent through an entrance slit of 100-μm slit width and a second pair of focusing optics with f= 85 mm (Kaiser Optical, 1.8 fi) onto a high-frequency transmission grating with 2400 grooves/mm. The effective spectral range of the spectrograph and high frequency grating extends from 2200 to 4600 cm^{-1} (HF-532 grating, Kaiser Optical Instruments) for analysis of high frequency vibrational modes). The theoretical resolution of the grating in combination with a CCD pixel array of 1024 pixels/26 mm of detector array is specified as 2.1 cm^{-1}/pixel, or in reciprocal resolution, 3.5nm/mm. The actual resolution within the applications of this study was determined as 5 cm^{-1}, based on actual measurements.

Background correction for the intrinsic signal contribution from the water in the bulk was carried out by introducing ultra-pure water into the sample cell and acquiring the background signal with Raman scattering from silica and water only and subtracting it from the subsequent Raman acquisition of the aqueous solutions containing the compounds of interest and converting to counts sec^{-1}, using the background correction algorithm provided with the data acquisition software (Solis ver. 4.16.3). Data acquisition was in multi-track mode (which corresponds to spectroscopy mode), at 1.6 x pre-amplifier gain, and 64.25 μsec vertical pixel shift speed, and 100 kHz readout rate, with an effective resolution of approx. 5 cm^{-1}. The raw background corrected Raman spectral data were further processed with the Origin Ver. 7.0 spectral analysis software to correct for laser drift and consequently baseline drifts. The air-cooled detector (temperature at -70˚C) is a back-illuminated deep-depletion charge-coupled device (CCD) by Andor Technologies, Inc. (DU-BR-DD) with a 70% QE, based on quantum efficiency curves specified for this model, and a dark current of 1 e^{-} $pixel^{-1}sec^{-1}$ at -70˚C detector temperature.

Chapter 5: Research Results from Validation and Optimization Procedures

Initial adsorption studies at the silica-air and silica-water interface were carried out using the argon ion laser as excitation source, powered at 1.0 W output at the laser head, with a measured power density of 0.220 W before focusing. The results from these trial studies and optimization procedures are summarized in the following section:

5.1. Study of a monolayer of octadecyltrichlorosilane (OTS) at the silica-air interface

One of the early studies for testing the capabilities of TIR Raman spectroscopy included the spectral analysis of an OTS monolayer at the silica-air interface using a right-angle prism, with close to 45˚ incident angle of the laser excitation beam, in order to maximize the Fresnel transmission coefficient, and thus achieve the maximum Raman scattering intensity (Fig. 5.1.1). The OTS monolayer was applied by reacting 1 mM of OTS (95% purity) in hexane solvent with a cleaned and piraña solution (70% H_2SO_4/30% H_2O_2) treated fused silica prism surface that leads to spontaneous formation of an OTS monolayer by a substitution reaction of the OTS chloride ions with the silanol (–OH functional groups) on the silica surface. The spectrum of the OTS layer (estimated 2 nm thickness) is shown below. No specific polarization was applied in these experimental trials. The initially low signal intensities were improved in future experiments by making several changes in the sampling configuration.

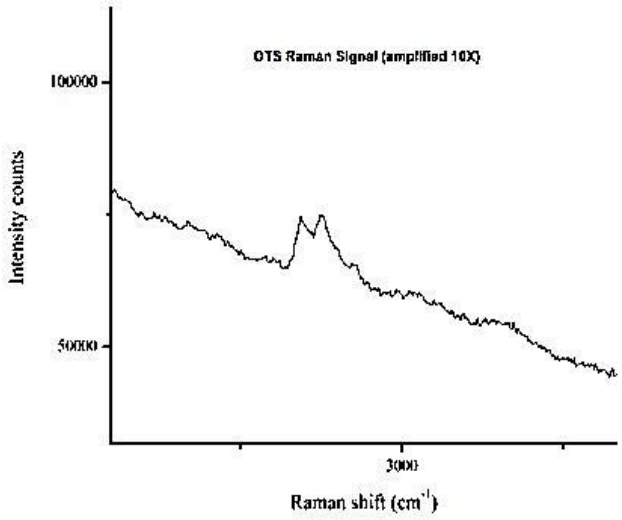

Fig. 5.1.1: TIR Raman spectrum of an OTS monolayer at the air-silica interface

Subsequent experimental work was carried out primarily at the silica-water interface, with the collection objective facing the curved side of the hemispherical TIR element (Fig. 4.1.1.) and collecting the signal through the silica material itself, as compared to the initial signal collection geometry where the signal collection occurred from the opposite side through the aqueous phase; scattering intensity collection through the aqueous resulted in signal intensity losses.

5.2. Adsorption studies of volatile organic compounds at the silica-air interface

After replacement of the right-angle prism with a hemisphere, trial studies tested the potential adsorption of two volatile organic compounds, methanol and acetonitrile, from the gas-phase to the silica-gas interface. The condensation of these volatile organic with

low boiling points, and transfer from gas to liquid phase was not successful. The equilibrium constant for adsorption at room temperature conditions, related to the ratio of the heat enthalpy of adsorption - ΔH^{o}_{ads} and enthalpy of desorption, - ΔH^{o}_{des} was too small to transfer the molecules from the gas phase to the solid silica surface. An alternative approach was coating the silica surface with a thin aqueous layer, by passing water vapor over the silica surface with subsequent condensation of water molecules that facilitated adsorption via diffusion into the water layer. The TIR Raman spectra of methanol and acetonitrile, adsorbed at the silica-air interface, after applying the thin water film, are shown below:

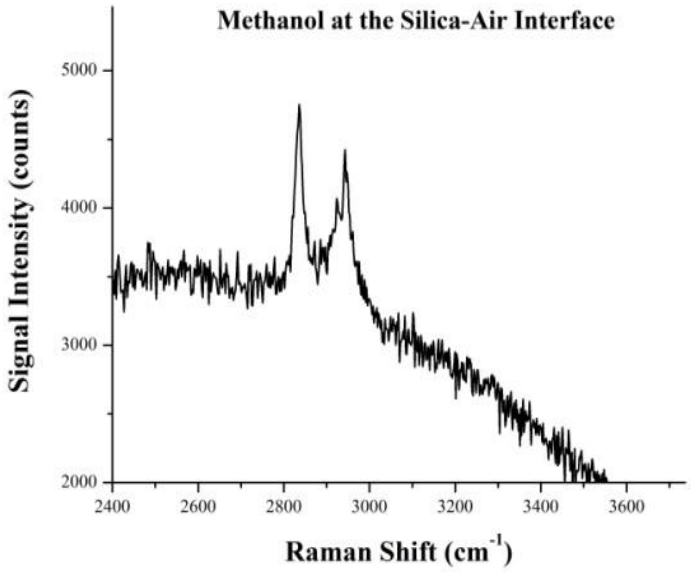

Fig. 5.2.1: Methanol spectrum in TIR geometry at the silica-air interface

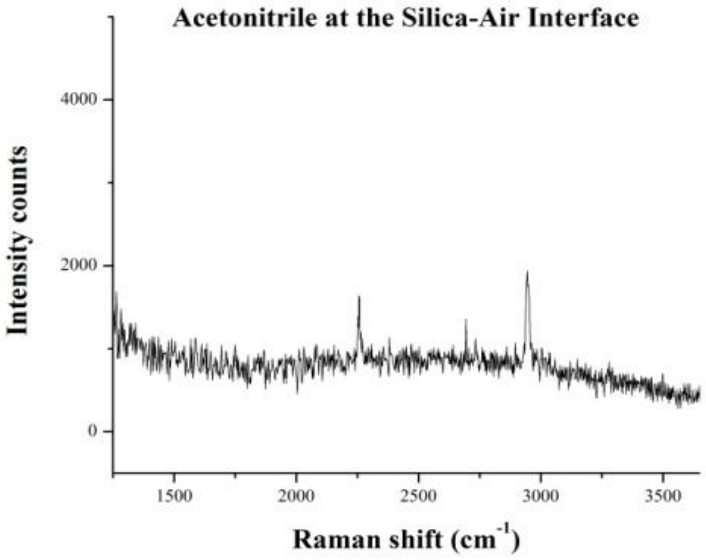

Fig. 5.2.2: Acetonitrile spectrum in TIR geometry at the silica-air interface

A comparison with previous research studies (SFG techniques) confirmed that adsorption to silica-air interfaces is enhanced for low molecular weight alcohols and related compounds as they are retained by the water film and adsorb to the interface.[141] The resulting signal intensities, that were obtained with detector acquisition parameters of 10 x 60 sec acquisition time and 1.6x pre-amplifier gain were relatively weak, but demonstrated the capabilities of the set-up for detecting Raman signals in TIR geometry. Following experimental work primarily focused on the adsorption of molecular species at the silica-water interface, carried out in a closed flow cell as shown in Fig. 4.4.1. and the experimental layout in Fig. 4.5.1.

5.3. Adsorption of ionic liquids at the silica-water interface

Since there is strong interest in studying the adsorption potential of ionic liquids at the silica-water interface, a common and water-soluble ionic liquid, 1-butyl-3-methyl imidazolium dicyanamide [BMIM][DCA], was chosen as a model room temperature ionic liquid (RTIL). Adsorption of [BMIM][[DCA] was studied at the silica-water interface, after several changes were made in the sampling geometry to improve the intensity of the incident laser excitation source, and the scattered signal collection.

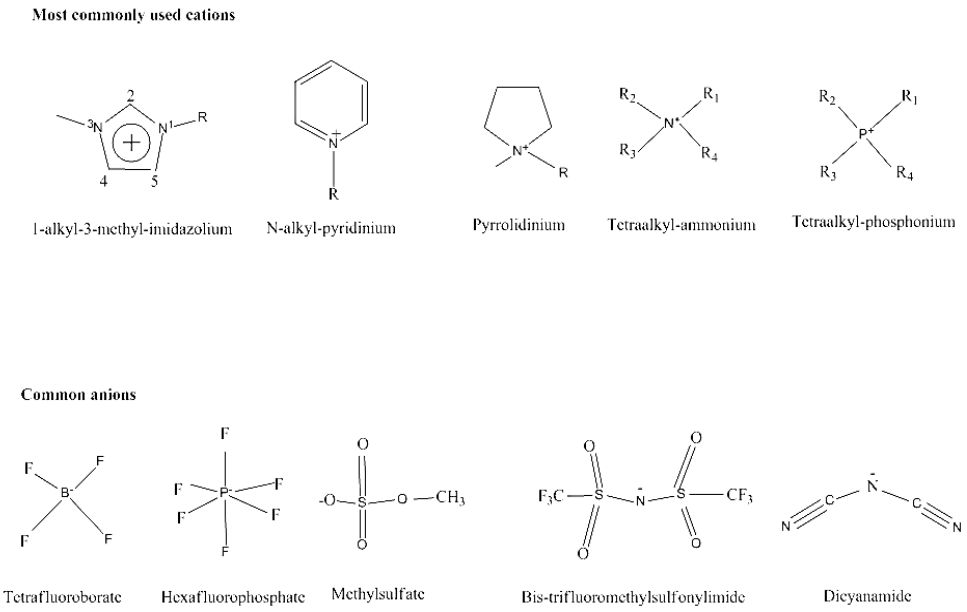

Fig. 5.3.1: Structure of ionic liquids: most commonly used cation and anion types

The structures of typical ionic liquids (Fig. 5.3.1) clearly indicate that the cationic charge is balanced by the accompanying anions. Adsorption to the silica surface was initially

expected under the assumption that the cationic portion of the ionic liquid is attracted to the negatively charged silica surface and adsorption takes place via electrostatic attraction between the cation and the silica surface. The adsorption isotherms obtained for the studied ionic liquid [BMIM][DCA], appeared initially successful. However, the linear relationship between signal intensity and concentration, as shown below, was ultimately proof that the Raman signal measured was representative for the molecules in the bulk – within the probing depth of the TIR Raman configuration – and indeed no adsorption took place, i.e., without surface excess relative to the bulk. The signal intensity vs. concentration departed from linearity only at extremely high ionic liquid concentrations as a consequence of the mole fraction of the ionic liquid reaching high enough levels to affect the refractive index ratios, and the Fresnel transmission coefficients. Correlation between refractive index changes with increasing ionic liquid mole fractions and changes in TIR parameters (Fig. 5.3.2) confirmed that the deviation from linearity was solely a consequence of varying the TIR sampling conditions, and that water soluble short-alkyl-chain ionic liquids would not have any thermodynamic driving mechanism for adsorption to the surface in excess.

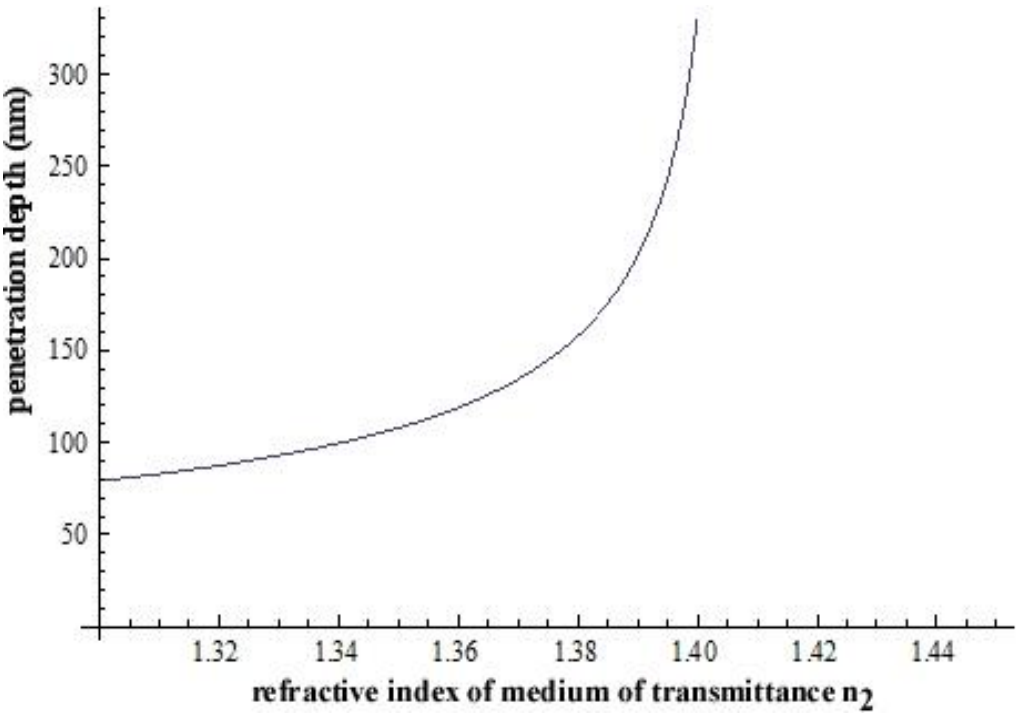

Fig. 5.3.2: Evanescent field penetration depth as function of the refractive index change in solution (n_2)

Increasing the solution pH to 12 in order to deprotonate the silica surface silanols and increase the negative silica surface charge did not have any effects on the ionic liquid adsorption, neither did the coating of the silica with a hydrophobic octadecyltrichlorosilane (OTS) layer. The exponentially increasing signal was indicative of the refractive index ratio change and its optical effects (Fig. 5.3.2.). No significant changes in the evanescent field penetration depth and Fresnel coefficients are expected over a small range of refractive index changes, but significant enhancement of the Fresnel coefficient occurs at high molar volume fractions, due to the smaller than intended refractive index ratio, and larger critical angle. The actual refractive index change again depends on the actual refractive index of the molecules tested vs. the pure water

refractive index, and, if large, may drive the penetration depth theoretically to infinity. A thorough analysis of the TIR parameter settings and their effects on the signal intensity revealed that the TIR geometry was extremely sensitive to variations in the refractive index ratio that results in changes (usually an increase) of the actual critical angle θ_c relative to the intended angle of incidence, and consequently an increase in the evanescent field penetration depth and the Fresnel coefficients (Fig. 5.3.4).

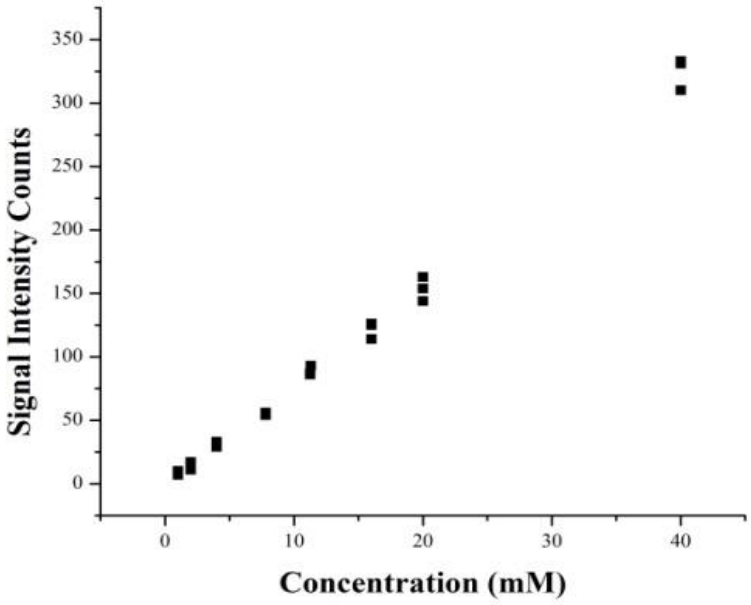

Fig. 5.3.3. Signal intensity vs. concentration of [BMIM][DCA] at the silica-water interface showing linear relationship between concentration and signal

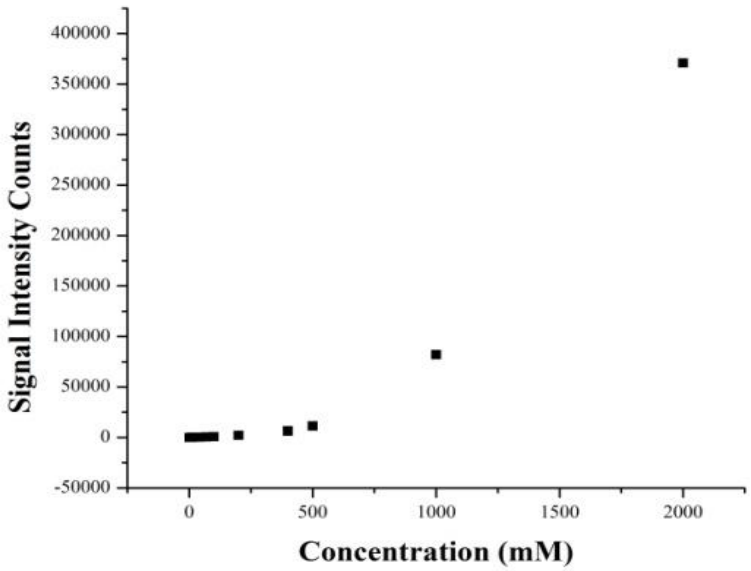

Fig. 5.3.4: Signal departure from linearity at high concentrations of [BMIM][DCA]

The signal vs. concentration relationship (Fig. 5.3.4) clearly indicates that reliable adsorption experiments need to keep the molar volumes within the typically relevant small concentration range and penetration depth to avoid biased signal intensities due to optical effects and probing molecules in the bulk.

Research studies reported the CMC for the related ionic liquid [BMIM][BF_4] as 0.94 mM[141], and 0.8 mM[142, 143] based on conductivity measurements; these values, even if correct, do not represent the typical behavior of a surfactant and aggregate forming agent, and would not qualify for meaningful studies using TIR Raman spectroscopy. The experimental results further emphasized that the linear relationship between the concentration in the solution and the measured Raman scattering signal over a wide

concentration range originates from the molecules in the bulk and does not convey any information on the adsorption behavior of the compound studied.

5.4. Adsorption of anionic surfactants at the silica-water interface

Based on the findings in the experimental work with [BMIM][DCA] at the silica-water interface, an attempt was made to test adsorption properties of long alkyl-chain molecules, i.e., two anionic surface active agents, lithium dodecyl sulfate (LDS), an analog of sodium dodecyl sulfate (SDS), and sodium dodecanoate (also known as sodium laurate). The results confirmed the lack of adsorption seen with ionic liquids, in agreement with classic textbook statements that negatively charged surfactants do not adsorb at the silica surface with a negative charge of -0.013 C/m^2 at neutral pH, although they are amphiphilic molecules with a hydrophobic alkyl chain. Attempts to modulate the intrinsic silica surface charge by adsorption of positively charged divalent metal ions did not give any positive results due to thermodynamically more favorable complexation of the divalent metal ions with the anionic functional groups leading to liquid suspensions of metal-surfactant in the form of MS_2 and no adsorption observed.

Figs 5.4.1. and 5.4.2 below illustrate the linear relationship measured between the surfactant concentrations and the Raman signal intensities confirming that the contribution to the Raman signals is related to the molecules present in the bulk within the penetration depth of the evanescent electric field, that corresponds to 210 nm at the given sampling geometry with the incident angle of 67˚ set close to the critical angle.

Amphiphilic molecules with a hydrophobic portion in the molecular structure, i.e, as found with true surfactants that contain long alkyl chains with twelve carbon atoms or more, and charge compatibility between surfactant head group and surface charge, are required for observing true surface excess at the solid-liquid interface.

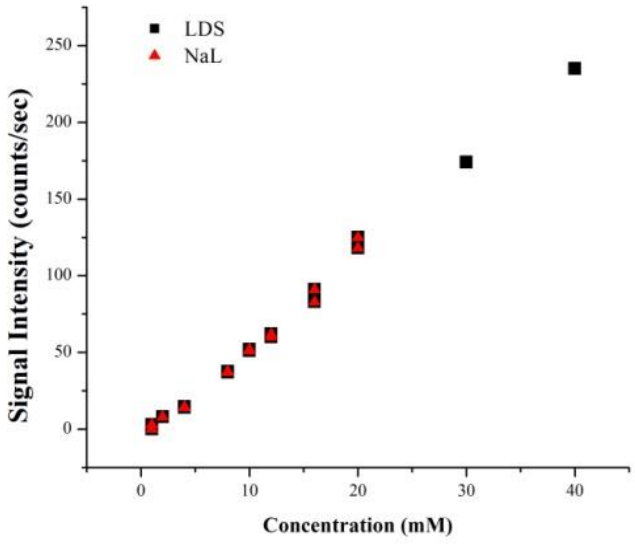

Fig. 5.4.1: Raman signal intensities of LDS and sodium laurate at the silica-water interface

In case of positively or negatively charged head groups in the molecules, the preferred adsorption surfaces are those of opposite charges; however, literature data and the following studies have demonstrated that both cationic and non-ionic surfactants may adsorb at non-polar or hydrophobic surfaces, since charge repulsion is not present, and assuming other thermodynamically favorable mechanisms are available,[15, 59] but no

significant studies have shown the possibility of anionic surfactant adsorption at pristine silica surfaces.

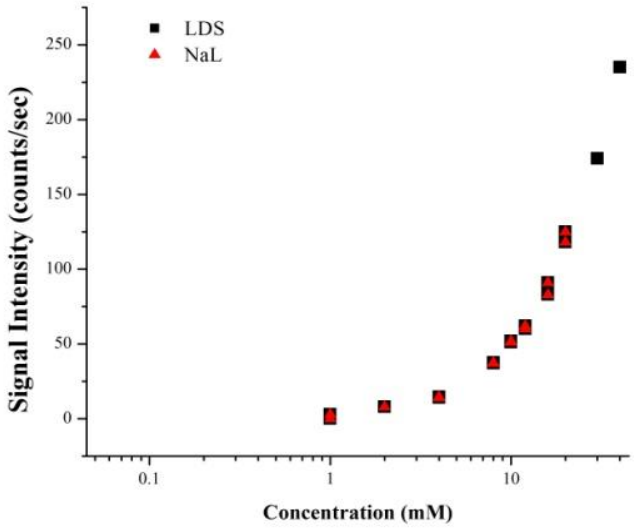

Fig. 5.4.2: Intensity vs. concentration of LDS and sodium laurate - log scale

5.5. Adsorption of dodecylbenzyldimethylammonium chloride ($DDBMA^+Cl^-$)

The first cationic surfactant studied as part of the preliminary experimental work, was dodecylbenzyldimethylammonium chloride, containing an ammonium head group with a methyl substituted benzyl ligand, and an C_{12} alkyl chain. This compound exhibited extremely slow adsorption kinetics due to the bulky benzyl ligand at the ammonium head group. The initially successful experimental outcome, however, was complicated by unusual behavior in the concentration region that corresponds to twice the CMC

concentration. Both the original and duplicate study showed some variation in the adsorption plateau before the CMC – according to previous studies determined between 8.18 mM[144] and 8.8mM[116] for the pure compound - and difficulty to reproduce the equilibrium position; the adsorption isotherm dropped to negligible values at around 10 – 11 mM of surfactant concentration. This unexpected desorption was confirmed by a duplicate experiment, but is inconsistent with the behavior of pure surfactants; the exact impurity or additive that lead to this competing mechanism could not be identified nor could this behavior be rationalized by similar phenomena or confirmed by previous studies. The only study found in literature that showed fluctuations in adsorption behavior was related to adsorption losses in connection with anionic sulfate containing surfactants in a particular solid-liquid-surfactant matrix, that was not directly applicable to the system studied.[5]

Some unknown type of impurities – their presence was confirmed by surface tension measurements (Fig. 5.5.1) – caused desorption of the surfactant from the silica surface starting at a surfactant concentration of 10 mM, that might correspond to a critical concentration of the impurity, or additive, resulting in desorption of the surfactant altogether, via trapping by surfactant aggregates or silica surface property alteration. The surface tension curve shows an almost linear decrease in surface tension with a 2nd depression before the actual CMC at log -2.2 suggesting residual contaminants from production or intentional addition of impurities for surfactant property modulation.

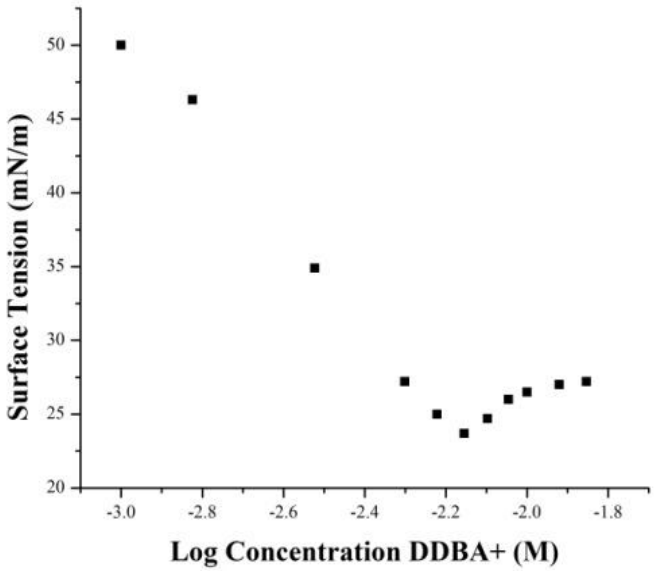

Fig. 5.5.1: Surface tension curve for $DDBA^{+}Cl^{-}$ showing characteristic dip before the CMC at approx. 8mM

The surface tension measured at this concentration is approx. 23 mN m^{-1} that is considerably lower than the values found in literature for related surfactants, and strongly suggests that non-ionic additives, possibly containing [$–O-CH_2$] ethoxy units, have been added. Further additives may consist of inorganic salts, as indicated by white solids found at seal rings that were in contact with the surfactant.

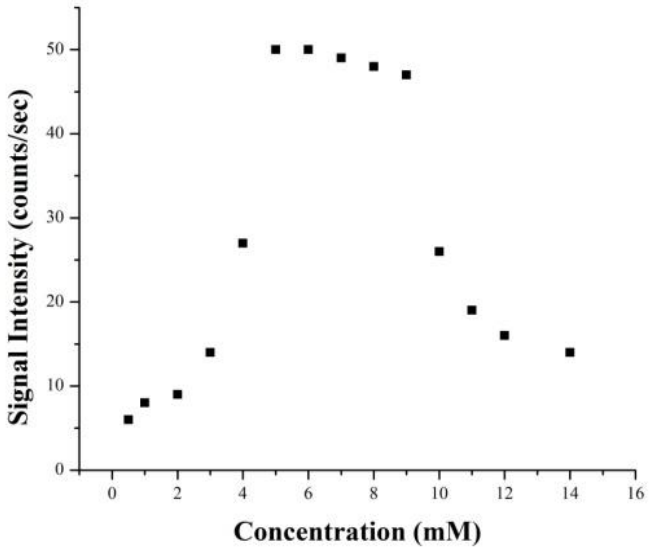

Fig. 5.5.2: Adsorption isotherm of $DDBA^{+}Cl^{-}$ showing adsorption loss at 10 mM

The compound was received from a commercial supplier specializing on production of corrosion inhibiting surfactants and related components, that did not provide any specific information regarding the identity of the additives. Figs 5.5.2. through 5.5.4 show the resulting isotherms and the slow adsorption kinetics as function of time in the concentration range of 0.5 to 14 mM. A newly purchased surfactant was used in future research studies after in-house purification to avoid similar problems with interfering mechanisms of unknown origin. The slow aggregation and adsorption kinetics, however, observed with the trial compound – related to the bulky head group – were confirmed in future studies.

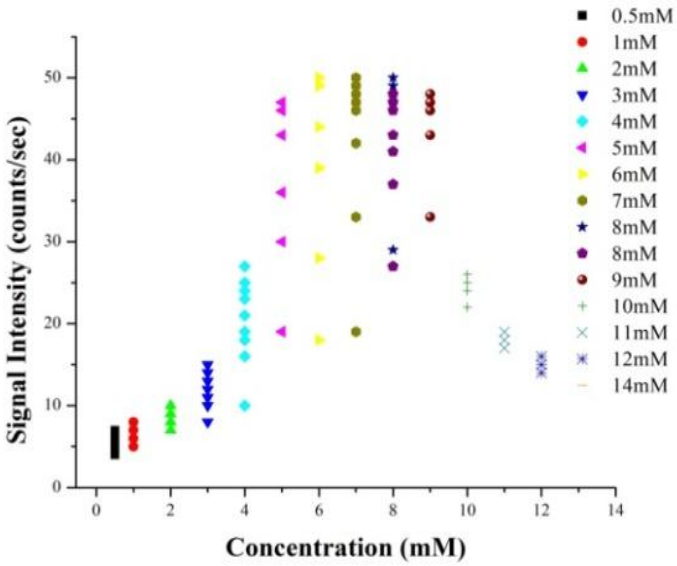

Fig. 5.5.3: Slow adsorption kinetics of $DDBA^{+}Cl^{-}$ in the concentration range of 0.5 to 14 mM of surfactant – shown: signal increase as function of time in increments of 12-13 minutes

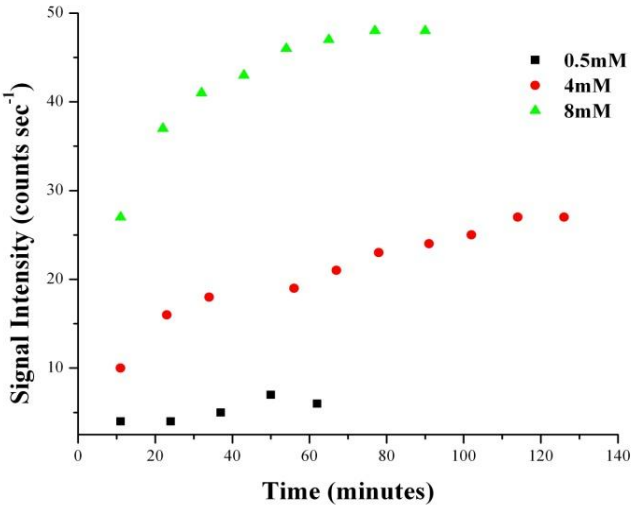

Fig. 5.5.4: Adsorption kinetics: signal increase vs. time (min) for three surfactant concentrations: 0.5 mM (■); 4 mM - on adsorption slope (●); 8 mM – before CMC (▲)

Another draw-back of these initial TIR Raman experiments was the relatively weak Raman scattering due to limited laser power, and laser drift. It complicated correct background signal corrections that were needed to subtract the contributions from the silica vibrational modes found at 1200 to 1600 cm^{-1} and the vibrational water bands between 3200 and 3600 cm^{-1}, as shown by the amplitudes of a typical Raman spectrum of the silica-water background and a typical background corrected spectrum of $DDBA^{+}Cl^{-}$:

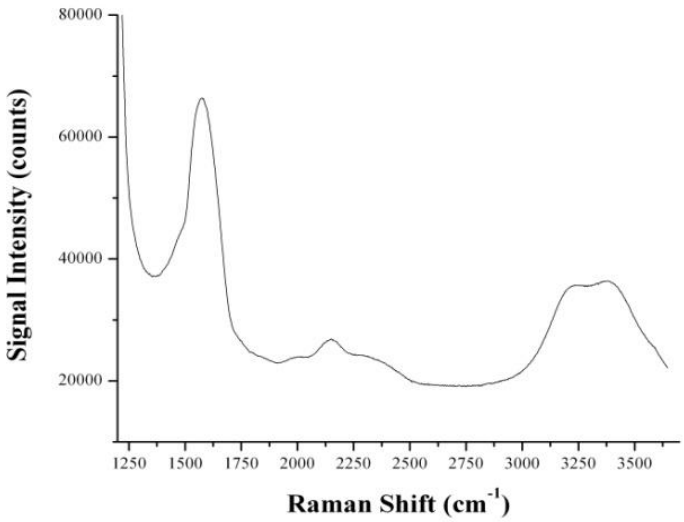

Fig. 5.5.5.: Background signal from the silica-water interface (laser source: argon ion laser – spectral range of 1250 to 3650 cm^{-1}).

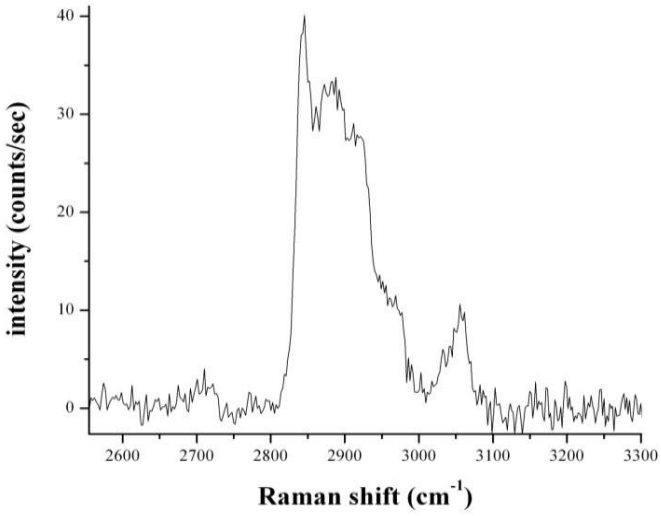

Fig. 5.5.6.: Raman spectrum of $DDBA^{+}Cl^{-}$ (0.5 mM) (laser source: argon ion laser – spectral range of 1250 to 3650 cm^{-1}).

This design and laser system did not allow using p-polarized spectral analysis as the alternative sampling geometry option and as a comparative tool for determining signal intensity ratios. The already moderate signal intensities in s-polarized sampling configuration would be further attenuated, as discussed in Chapter 3.

5.6. Validation of the TIR instrumental set-up

The TIR Raman set-up was validated against available literature data by using cetyl (or: hexadecyl-) trimethylammonium bromide (CTAB) as a test compound to establish an adsorption isotherm under the same relevant experimental settings and acquisition

parameters as subsequently used for the new surfactant under study, with exception of the laser source (Figs 5.6.1. and 5.6.2.).

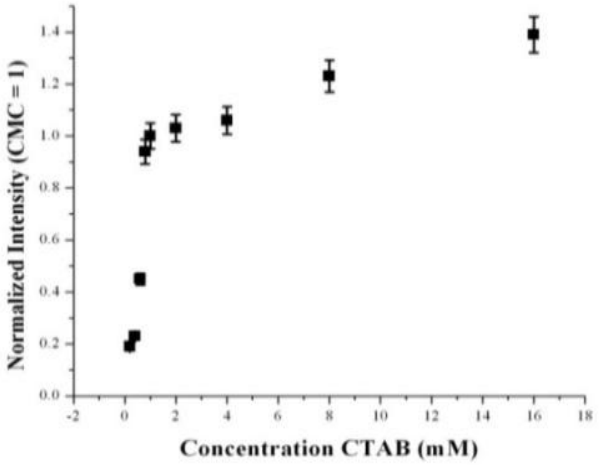

Fig. 5.6.1: Adsorption isotherm of the test compound CTAB – normalized to the CMC

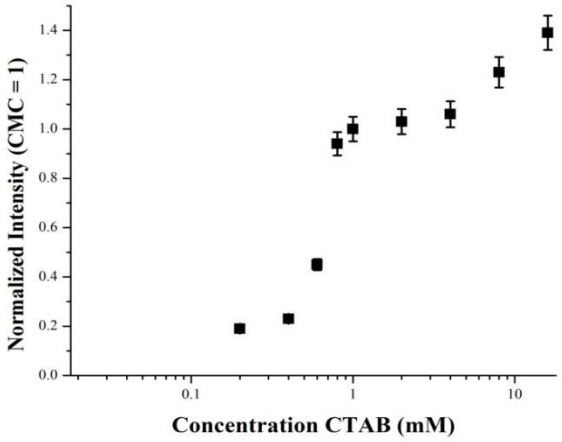

Fig. 5.6.2: CTAB isotherm – normalized to the CMC – log scale

The resulting adsorption isotherm, presented as normalized intensity vs. equilibrium concentration, shows trends and CMC values of 1mM that are in agreement with

previously published data.[101] The CTAB adsorption isotherm is shown without correction for the contribution from the bulk that was estimated at 0.027 mM^{-1} from linear curve fitting of the slope of normalized signal intensity vs. concentration for the concentration region above the CMC (Fig. 5.6.3). The signal contribution from the molecules in the bulk is non-negligible at surfactant concentration above 1mM and need to be factored out.

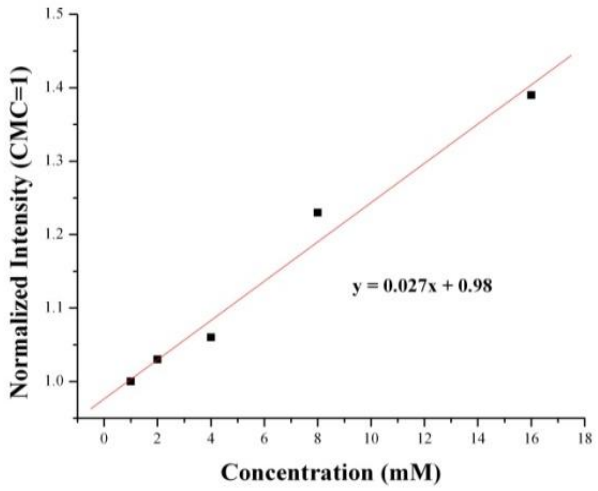

Fig. 5.6.3: Slope representing contribution from the bulk

The following experimental work was related to a surfactant with a CMC of 0.5 mM and adsorption isotherms studied in the range of 1 μM to 1 mM that did not require corrections for bulk contribution. The plots and curve fitted data from the experimentally determined adsorption isotherms confirm this assumption since no significant gradient was observed in the adsorption isotherms within the concentration region of interest.

Chapter 6. Adsorption of the Cationic Surfactant Benzyldimethyl-hexadecylammonium chloride at the Silica-Water Interface

6.1. General aspects of the adsorption of the cationic surfactant benzyldimethylhexadecylammonium chloride ($BDMHA^+Cl^-$)

Knowledge of the surfactant partitioning between the interface of interest and the bulk is of high interest when considering surfactants for applications in environmental and oil recovery operations. Incentives to study the adsorption isotherms of this compound arise from the requirement for minimal consumption of the chemical while maintaining optimum performance. Since quartz or silica are major constituents of soil formations, and also crude oil recovery processes, the adsorption to silica surfaces of this surfactant, containing a benzyl group ligand at the ammonium head group, was investigated in this study with the goal to identify its adsorption related thermodynamic and kinetic properties.[83, 103, 105, 145] The first part of the study evaluated the effects of electrolyte addition on adsorption behavior of the pure surfactant at the negatively charged silica surface, for predicting thermodynamic and kinetic parameters. These include, besides the common surface tension measurements at the air-water interface, adsorption isotherms at the silica-water interface, the concentrations that correspond to the critical micelle concentration (CMC), maximum surface coverage, and equilibrium adsorption constants that have been determined for the pure surfactant and also for the surfactant in the presence of varying concentrations of a divalent metal salt.[4, 86] The 2nd part of the study, related to adsorption behavior of the same surfactant at a hydrophobic silica surface,

identified changes in the relevant adsorption parameters as a function of surface properties.

In this study, the incident angle of the excitation beam was set at 73˚ giving a narrow beam diameter with a small numerical aperture (N.A.) of 0.11 at the focusing point. The polarization of the excitation laser source was chosen as s-polarized light in all experiments related to the adsorption isotherms, since the signal scattering intensity originating from the interaction of the symmetric Raman vibrational modes with s-polarized incident light proved to be stronger in TIR sampling and light collection geometry as compared to the signal intensity in p-polarized sampling geometry. Adsorption isotherms of the surfactant could be determined with a detection limit of 1 μM, for the pure surfactant, that corresponds to a fractional coverage of 0.014. Supporting experiments were carried out with p-polarized incident light that selectively probes the off-diagonal elements of the derived Raman tensor and light scattering along both x- and y-axes.

A major part of this study relates to the surfactant adsorption enhancement induced by a metal salt additive, i.e., the divalent metal salt magnesium chloride. Divalent metal halide salts have previously been studied in combination with anionic compounds where specific adsorption of the selected metals under favorable conditions induced charge inversion at the silica surface and promoted the adsorption of negatively charged species at the silica-water interface.[135] In contrast, the goal of this study was to evaluate the metal halide salt in terms of its enhancement of the hydrophobic effects, due to increased ionic

strength and thus increased polarity of the solvent, and its charge screening properties, that affect surfactant aggregation in solution. The adsorption isotherms and adsorption models for $BDMHA^+Cl^-$ (Fig. 6.1.1.), presented in this study, follow a Langmuir or a modified Langmuir adsorption model that includes an additional interaction energy parameter to account for interactions between neighboring molecules at the surface.[135, 136]

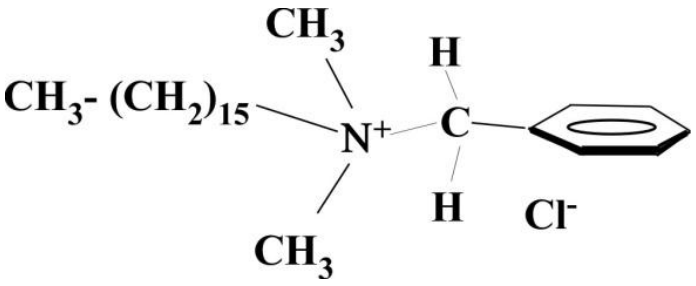

Fig. 6.1.1: Structure of benzyldimethylhexadecylammonium chloride

6.2. Surface tension and surface excess of $BDMHA^+Cl^-$

Benzyldimethylhexadecylammonium chloride (Sigma-Aldrich, purity >97%) was purified by recrystallization (three times) from acetone-methanol (90/10 v/v) and used for surface tension measurements by the "du Noüy ring" method (Ring tensiometer, Kruess GmbH, Hamburg, Germany – equipped with an iridium ring) over a concentration range of 0.1 to 0.8 mM to determine the surface tension curve in the relevant concentration range, in particular, the region before and the flat portion after the CMC, for both the non-purified and purified surfactant (Fig 6.1.1.). The CMC value was extracted from the intersection of the slopes obtained from curve fitting while the maximum surface

coverage at the air-water interface was found by relating the fitted linearized slope right before the CMC value to the thermodynamic expression in eq 3.10.1. A depression or 2nd minimum at a concentration of 0.40 mM is noticeable in the isotherm of the unpurified compound that is indicative of impurities affecting the actual surface tension behavior of a compound.[5, 83, 132]

The surface tension measured at the CMC was determined as 35.5 mN m^{-1}, but the surface excess value was not further used due to the limited number of data points gathered on the upper slope before the CMC. The surface tension slope is expected to decrease exponentially (slightly concave or linearly on a log scale) until it reaches its minimum at the CMC concentration when no further adsorption at the interface is energetically favorable. At this surfactant concentration, the chemical potential in the micelle is equal to the chemical potential of dissolved surfactant molecules present in the aqueous medium and no further aggregation of the surfactant in solution occurs. Surface tension values, determined at the air-water interface at 22.5˚C, reached their minima at the concentration corresponding to a CMC of 0.49 mM. This value is slightly higher than some values reported in literature, 0.34 mM[146], and 0.40 mM,[147] but it agrees well with other literature data that reported almost identical values of 0.485 mM,[109] and 0.49 mM.[91]

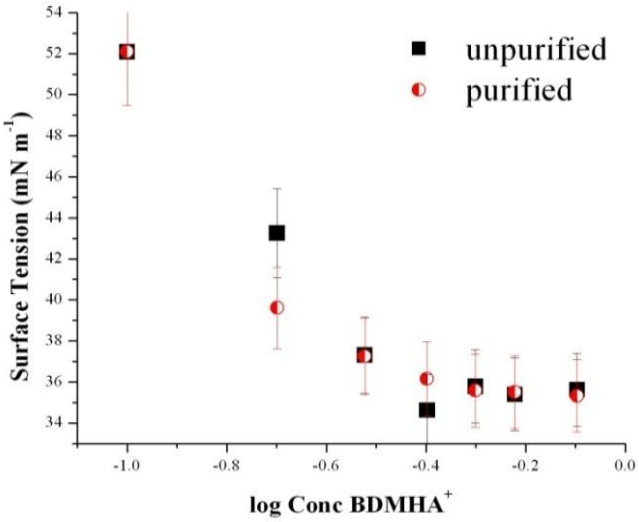

Fig. 6.2.1: Surface tension (mN m^{-1}) in the concentration range of 0.1 to 0.8 mM of purified (red-white circles) vs. unpurified $BDMHA^+$ (black rectangles)

Some of these variations may be explained by differing measuring and analytical techniques, different temperatures, and also by the purity level of the surfactant studied. Impurities may shift the surface tension properties in either direction depending on the concentration and nature of the impurity.[90, 132, 148]

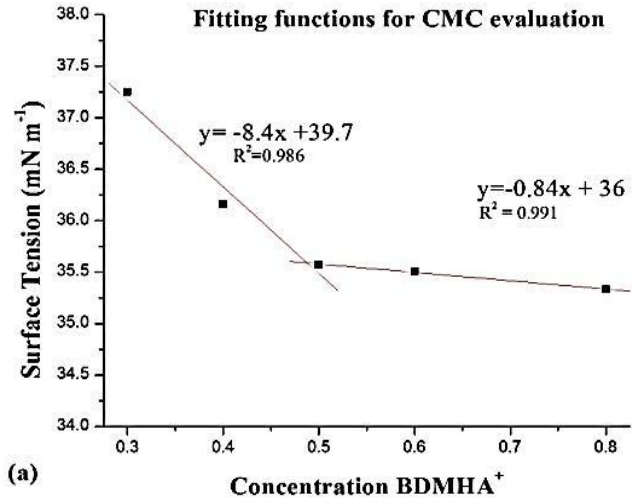

Fig. 6.2.2: Linear fit for CMC evaluation

6.3. Spectral analysis of $BDMHA^+Cl^-$

The symmetric methylene stretching mode at 2852 cm^{-1} was used as the primary indicator of the adsorption behavior. Although other Raman vibrational modes, i.e., the benzyl symmetric vibrations, are clearly visible and reproducible in the collected Raman spectra, the symmetric methylene stretching mode provides the highest signal intensity with a 3 counts sec^{-1} limit of detection at a S/N ratio of 3. This value corresponds to a solution concentration of 1 μM of the pure surfactant, and a fractional coverage of 0.014, relative to the normalized coverage of the pure surfactant with CMC set to 1. The resulting isotherms presented in the following sections (adsorption at the bare silica surface) are based on the amplitudes of the characteristic and dominant symmetric vibrational mode

of the methylene stretch in the alkyl chains that appeared superior in terms of reproducibility as compared to those generated from the integrated area over the C-H stretching region.

A representative Raman spectrum was obtained from the 0.5 mM surfactant concentration – that represents the CMC concentration – and fitted to a Gaussian model that shows the prominent Raman vibrational modes in the C-H stretching region (Fig 6.3.1). The spectral acquisition of the scattering intensity from s-polarized incident light from the 532 nm laser line was carried out without any polarizer in the collection optics; peak assignments for the respective Raman vibrational modes are summarized in Table 6.3. 1.

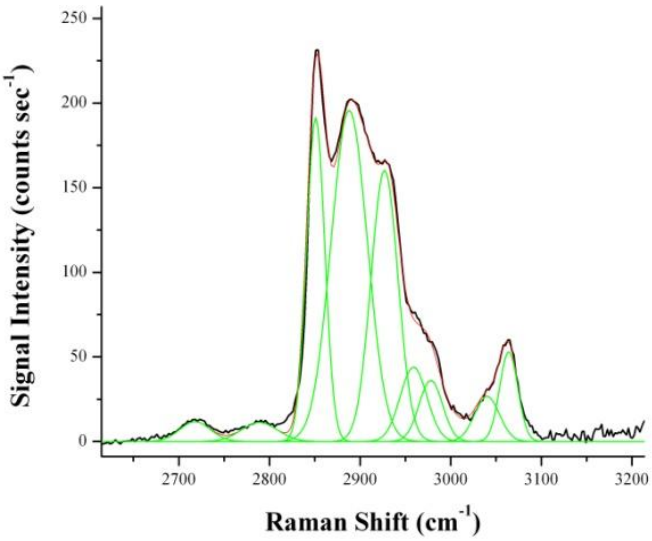

Fig. 6.3.1: Raman spectrum of the C-H stretching region in s-polarized mode for $BDMHA^+$ fitted to a Gaussian model

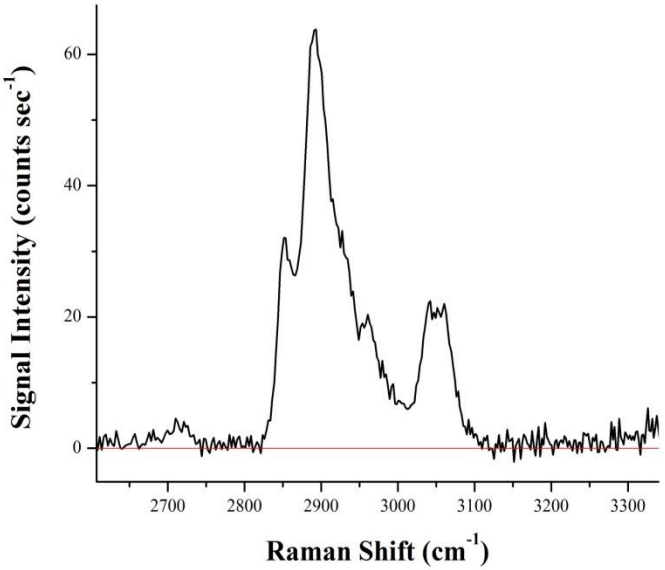

Fig. 6.3.2: Raman spectrum of the C-H region in p-polarized sampling geometry.

The Raman spectrum of the same surfactant molecule in p-polarized sampling geometry is shown side-by-side (Fig. 6.3.2.), to demonstrate the enhanced signal selectivity of this alternative geometry towards the anti-symmetric vibrational C-H stretching modes, but also with overall lower signal strength.

The symmetric methylene stretching modes at 2852 cm^{-1} dominate the Raman spectrum of the surfactant molecule in the C-H region, with high Raman scattering cross sections for the C-H stretching modes, in particular the symmetric vibrational modes. The CH_3- symmetric stretching mode at 2872 cm^{-1} is barely visible in the presented Raman spectrum although its intrinsic Raman scattering cross section is higher than that for the methylene group.

Table 6.3.1: Raman peak assignment [46, 51, 55, 149]

cm^{-1}	Vibrational Mode:	Relative Intensity:
2718	C-H ν_{δ} bend overtone	very weak
2789	C-H ring comb. band	very weak
2852	CH_2 ν_s	very strong
2872	CH_3 ν_s	very weak
2889	CH_2 ν_{as}	strong
2927	CH_2 ν_{sFR}	weak
2965	CH_3 ν_{as}	medium
2980	N-CH_3 ν_s	weak/medium
3040	N-CH_3 ν_{as}	weak
3064	C-H ring ν_s	strong

However, the number density of methylenes per molecule is fifteen methylenes vs. one methyl group in the hexadecyl chain making it the main contributor to the C-H stretching signal. The anti-symmetric modes of both the methylene groups and the methyl terminal group are discernible at 2889 cm^{-1} and 2965 cm^{-1}, respectively, although not well resolved. The peak at 2927 cm^{-1} is assigned to the Fermi resonance of the symmetric methylene stretch. Fermi resonances, that are combination bands of the overtones of fundamental C-H vibrational modes in the low frequency region (around 1300 – 1460 cm^{-1}) and the C-H fundamental stretching modes of the same symmetry in the high frequency region, are strongly represented in the high frequency Raman spectrum[55] as well as the stretching vibrations from the benzyl ring at 3064 cm^{-1}.

Additional minor Raman vibrational modes show in the spectral region between 2700 and 3100 cm^{-1}. The weak peaks at 2718 cm^{-1} and the barely visible peaks at 2789 cm^{-1} are

assigned to the overtone of the fundamental C-H symmetric bending modes (scissoring or symmetric bend), and a combination band of the fundamental in-plane bending mode and the out-of-plane C-H deformations of the benzyl group.[150] Raman vibrational modes appear at 2980 cm^{-1}, for the symmetric N-CH_3, and at 3040 cm^{-1} for its anti-symmetric mode that shifts to lower wavenumber of 3038 cm^{-1} at lower concentrations. This N-CH_3 anti-symmetric band was observed in a previous study of CTAB adsorption[55] , together with a second smaller peak at lower frequency, that appeared to merge into one mode. They were identified as two independent and out-of-phase vibrational modes by a 2D-simulation. In the spectral analysis of this study, both signals at 3017 and 3040 cm^{-1} increase proportional to surface coverage in s-polarized spectra, although the smaller peak at 3017 cm^{-1} is barely distinguishable from the baseline noise at low concentrations, and disappears in p-polarized spectra. Addition of magnesium chloride did not have any modifying effects on the Raman spectra when comparing pure surfactant spectra with spectra of surfactant with metal salt addition. The baseline offset noticeable around 3000 cm^{-1} was not considered a concern in terms of signal intensity interpretation; it is the result of baseline fluctuations and the appearance of small vibrational modes in the frequency region of 3000 – 3042 cm^{-1}, as discussed above.

6.4. Structural and orientational analysis of the pure surfactant

Structural analysis of the pure surfactant was carried out by using signal intensity ratios and potential ratio changes of the CH_2 anti-symmetric/CH_2 symmetric stretching modes

as well as CH_2/CH_3 ratios (Fig. 6.4.1 (a) and (b)), to identify any potential restructuring of the pure surfactant as function of concentration.

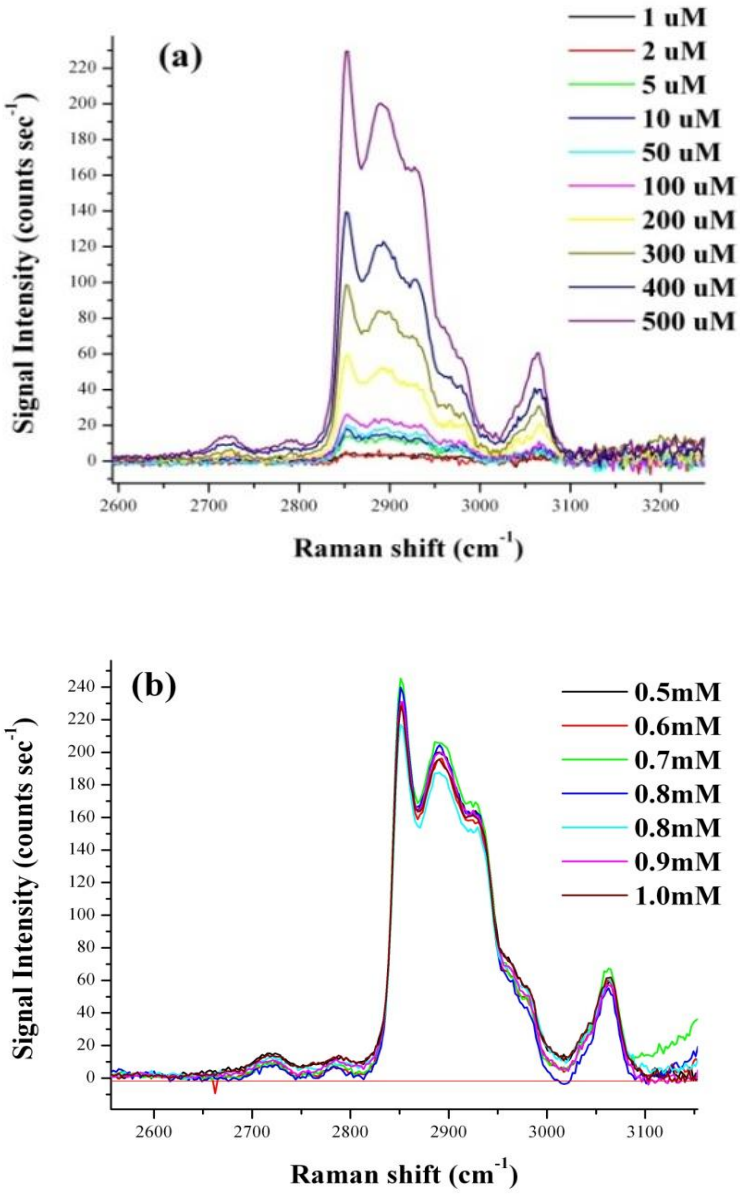

Fig. 6.4.1. : Spectral analysis and comparison of $BDMHA^+$ in the concentration range of (a) 0.001 to 0.5 mM and (b) 0.5 to 1.0 mM at adsorption equilibrium

A second experiment evaluated the intensity ratio changes in p-polarized sampling geometry as function of time at one single concentration (Fig. 6.4.2), but neither did reveal any changes in intensity ratios that might hint towards surfactant reorientation within the TIR probing depth.

Signal intensities in both s- and p-polarization and two different signal collection geometries provided the input to compare the signal intensity ratios: p-polarization in TIR geometry probes the symmetric α'_{xx} and the off-diagonal derived Raman tensors and is most sensitive towards vibrational modes with their oscillating dipoles at the surface aligned with the incident p-polarized electric field. P-polarized incident light with no polarizer in the collection optics (defined as P_{x+y}) probes primarily the scattering intensity of the off-diagonal derived Raman tensor α'_{xz} (= α'_{yz} at the isotropic surface), and $\alpha'_{yx,}$(= α'_{xy}) along both the x-and y-axes;[56, 69] Raman scattering from the α'_{zz} tensor that probes the vibrational modes along the surface are negligibly small in this sampling geometry; no polarizer was integrated in the collection optics, since the collected Raman scattering signals in p-polarized sampling geometry are weaker as compared to s-polarization mode signal collection and would be even more attenuated with selective filtering out of the respective scattering modes.[54, 55] S-polarized incident light sampling geometry with the polarizer set to collect the scattering intensity along the y-axis (S_y) probes primarily the symmetric Raman tensor α'_{yy} (= α'_{xx} at the isotropic surface), i.e., symmetric methylene stretching vibrations, with resulting strong Raman signal intensity. S-polarized incident light without polarizer in the collection optics (S_{x+y}) that gave the strongest Raman

scattering intensity, was the primary sampling geometry for all isotherm related experiments in the 1st part of the study.

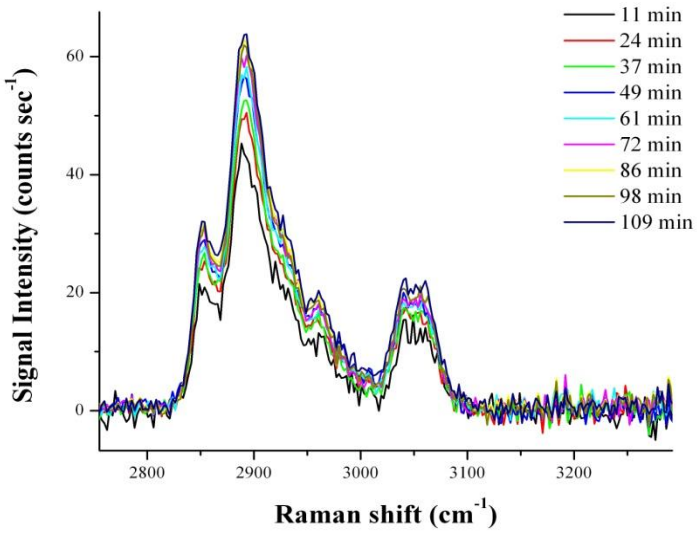

Fig. 6.4.2.: Spectral analysis and comparison of $BDMHA^+$ (0.4mM) in p-polarization mode - signal intensity evolution as function of time

6.5. Adsorption isotherm of the pure surfactant $BDMHA^+Cl^-$

TIR Raman spectral analysis of the respective surfactant concentrations (Figs. 6.4.1. (a) and (b)) provided the input for establishing the isotherms as presented in Figs. 6.5.1 through 6.5.5 on an absolute scale in counts sec^{-1} and a normalized scale (CMC= 1). The trends in the adsorption isotherms, based on the CH_2 symmetric stretching mode of the pure surfactant, are in agreement with the isotherm based on the signal intensities of the benzyl vibrational mode at 3064 cm^{-1}, that were used as secondary reference signals. They both show identical adsorption trends, in terms of the slope of $d\Gamma/d\log C$, and

CMC, with some variability in the low concentration region. The signal intensities observed at concentrations below the CMC and most likely above the CMC up to 1 mM originate from the molecules adsorbed at the surface with negligible contribution from the molecules in the bulk.[55] The spectral information that could be obtained within the concentration region from the detection limit of 1 μM to 1mM appeared sufficient for determining the adsorption isotherm without the need to probe higher surfactant concentrations.

Adsorption at the silica-water interface is presumably initiated by electrostatic attraction between the negatively charged silica surface,[86, 98] estimated as -0.013 C m^{-2} at neutral pH, and the positively charged ammonium head group.[101] The initial onset of adsorption reaches an intermediate plateau region at 10 uM (Figs. 6.5.1. and 6.5.2.), followed by an almost linear slope with low slope of dΓ/d log C in the adsorption isotherm between 10 and 100 μM (Figs.6.5.2 and 6.5.5), that changes abruptly to a higher and almost exponentially increasing adsorption slope arising from hydrophobic effects at the point of the critical surface aggregation concentration csac), and hemi-micelle formation, until the equilibrium plateau with maximum coverage is reached at the CMC. The pure surfactant exhibits two distinguishable plateaus, with the first plateau reached after the electrostatically driven adsorption ceases, most likely due to charge neutralization of the silica surface after initial surfactant adsorption (shown as enlarged view of this segment in Fig. 6.5.5).

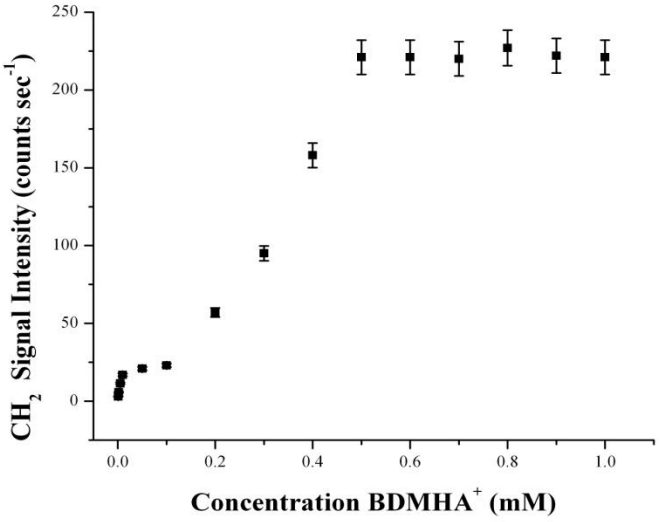

Fig. 6.5.1: Adsorption isotherm based on the absolute CH_2 signal intensity

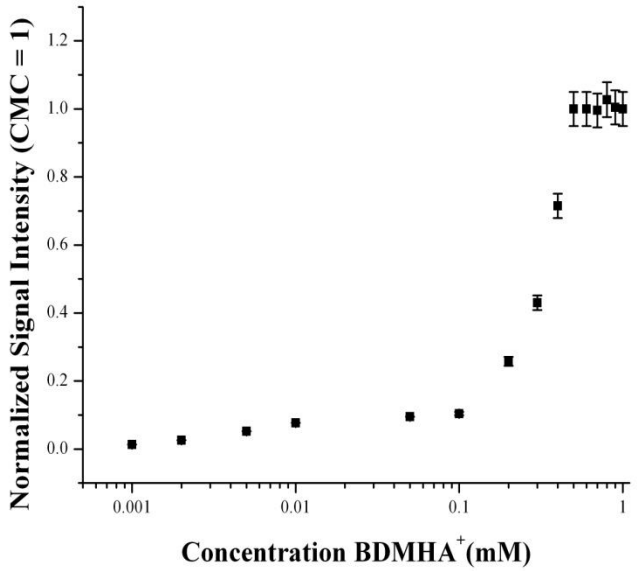

Fig. 6.5.2: Adsorption based on the normalized CH_2 intensity

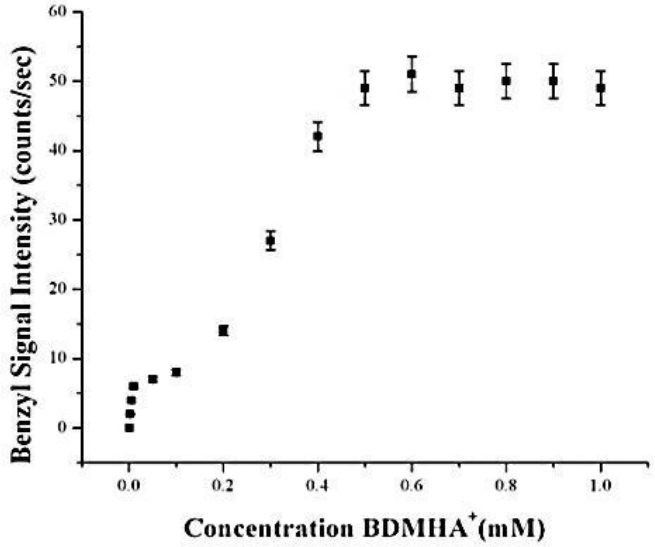

Fig. 6.5.3: Adsorption isotherm based on the absolute benzyl stretch signal intensity

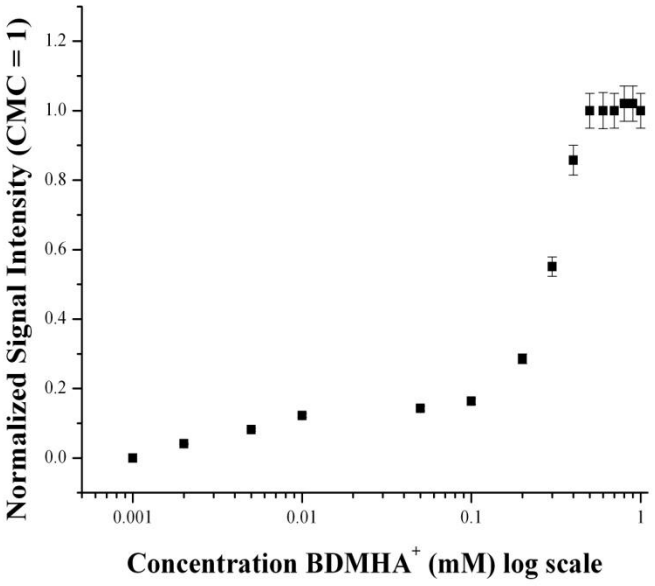

Fig. 6.5.4: Isotherm based on the normalized benzyl stretch signal intensity

This isotherm shape matches the two step adsorption model, suggested by Somasundaran et al., as illustrated in Fig. 3.11.1, in context with formation of spherical or quasi-spherical micelles.[86, 151]

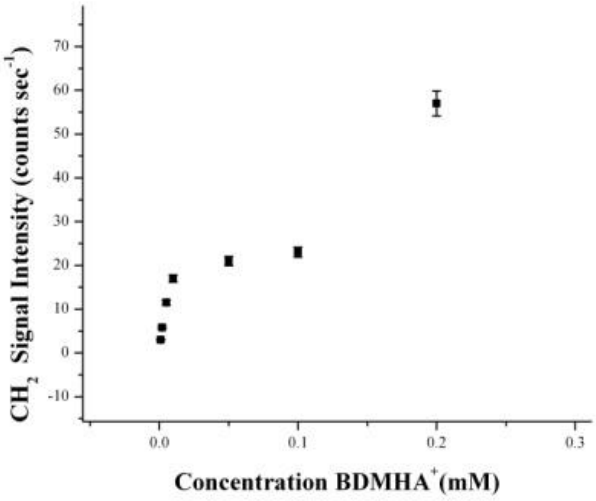

Fig. 6.5.5: Exploded view of the low concentration region of the isotherm

As concentrations increase, a steep adsorption slope of dΓ/d log C is observed that represents the hemi-micelle formation region. Adsorption in this concentration region is primarily driven by hydrophobic interaction of the non-polar long alkyl chains of the surfactant with the water molecules that might be intensified by the benzyl functional group. The benzyl ligand increases the hydrophobic nature of the surfactant's hydrophobic portion counting equivalent to three additional methylene groups being added to the alkyl tail,[93] that would increase its overall hydrophobic property and tendency to reduce contact area with surrounding water molecules by adsorption to the silica surface, thus lowering the Gibbs free energy of the system. The bulky benzyl

ligand, however, may also be responsible for repulsive forces among adjacent and sterically hindered surfactant molecules at the silica-water interface that oppose the hydrophobic driving mechanisms, and contribute to the slow adsorption kinetics observed in the upper region of hemi-micelle formation and above the CMC.

The adsorption isotherm shows a breakpoint at a surfactant concentration of 0.5 mM that forms the intersection between the increasing slope before the CMC and the linear portion of the adsorption slope above the CMC.

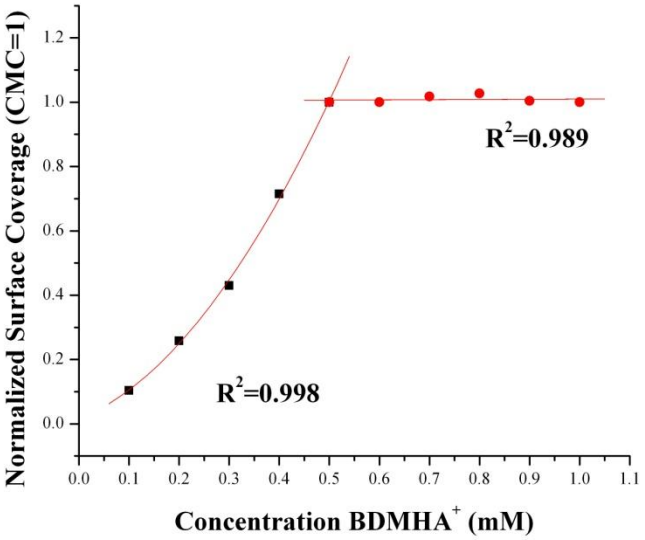

Fig. 6.5.6: Curve fitting of $BDMHA^+$ adsorption isotherm – normalized to CMC=1

The CMC value of 0.50 mM, extracted from curve fitting and taking the point of intersection of the fitted slopes, agrees well with the CMC value found from the surface tension measurements.

One significant difference in the adsorption behavior of $BDMHA^+$ as compared to CTAB and the related cetyltrimethylammonium chloride (CTAC) was the slow adsorption process, or slow adsorption kinetics;[55, 101] that were noticeable throughout the concentration range studied, but most pronounced with the pure surfactant at concentrations right below and above the CMC. The slow adsorption process, with up to 6 hours for the surfactant to reach equilibrium at high concentrations, might reflect the slow kinetics of aggregate formation in solution due to the different head group geometry containing the bulky benzyl group.[111] It increases the interfacial area with the surrounding water molecules and adds more hydrophobic character to the surfactant that favors both micellization and adsorption, but also poses mobility constraints due to its bulky head group ligand. The benzyl ligand is part of the head group function and head groups are not considered a part of the micellar core,[93] with their energetically most favorable conformation suggested as lying parallel to the micellar outer surface of this surfactant.[112]

The kinetic rates of monomer transfer in and out of the micellar core, typically found in the range of μsec, or for long alkyl chain surfactants (> l2 carbons) in the msec range, would not support this interpretation of the surfactant behavior; in contrast, values reported from basic studies show that the kinetics for the forward reaction of monomer transfer into micelles, k_+, increases exponentially, relative to the reverse process of monomer exit from the micellar core, k_-, with corresponding increase of the equilibrium constant K, where K is defined as follows:

$$K = \frac{k+}{k\_/n} \qquad (6.4.1)$$

and n stands for the average aggregation number or number of monomers in the micellar core.[111] A high K value would be consistent with the observations made in this study when extrapolating it to a surfactant with sixteen carbon atoms in the hydrophobic alkyl chain and a hydrophobic benzyl ligand.

The observed slow adsorption kinetics appeared strongly related to slow surfactant aggregation and rearrangement in the respective sample solutions that were prepared for testing in the Raman sampling cell, with a strong dependence on the time elapsed between sample preparation and the actual study in the Raman spectroscopic cell, in particular for surfactant concentrations around and above the CMC. Samples that were prepared and kept overnight before testing, showed extremely slow adsorption and did not reach the adsorption plateau until approx. four to six hours, whereas freshly prepared samples attained their adsorption equilibrium within three hours or less. The Raman signal intensities of freshly prepared samples in the 0.6 to 0.9 mM concentration range (above the CMC) as function of time showed unusual adsorption behavior with an adsorption plateau attained after 2 to 3 hours, at a signal intensity of 221 counts sec^{-1},

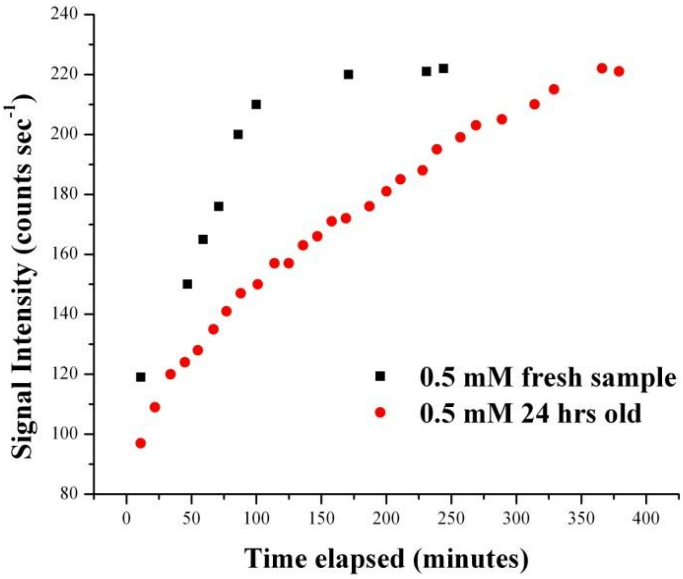

Fig. 6.5.7: Adsorption kinetics for $BDMHA^+$ (0.5mM) of a fresh sample vs. 24 hrs old sample

reproducibly observed in all spectral analyses of surfactant concentrations; surface coverage increased further, and then dropped back to the previously measured surface coverage. It might reflect the kinetic rates of monomer exchange, i.e., transfer of the monomers into or out of the micelle in aqueous solution,[111] required to adopt to changing equilibrium conditions in solution, that occurred at slow rates and lagged behind the actual equilibrium position of the complete system (Fig. 6.5.7.).

6.6. Effects of divalent metal salt addition on $BDMHA^+Cl^-$ adsorption

Addition of 5 mM divalent metal salt, in this experiment, magnesium chloride (as $MgCl_2 \cdot 6H_2O$) was sufficient to modify both thermodynamic properties of the pure surfactant, i.e., free energy of micellization, CMC, surface coverage, and adsorption kinetics in all three distinct adsorption regions, i.e., at very low surfactant concentrations, where attraction to the surface is usually governed by electrostatic forces, in the hemi-micelle formation region, and in the adsorption plateau region with surfactant concentrations above the CMC. The CMC of the surfactant shifted to 0.050 mM or 50 μM, which is 1/10the of the CMC concentration of the pure surfactant, accompanied by an increase of the adsorption slope in the hemi-micelle region (Figs 6.6.1 (a) and (b)), and a simultaneous decrease of the maximum surface coverage to one half of the surface density that was observed for the pure surfactant. Previous research studies of electrolyte effects on surfactant adsorption have demonstrated both increasing and decreasing surface coverage in the presence of an electrolyte relative to the pure surfactant, depending on the investigated systems.[2, 86]

The fractional surface coverage decreases to 0.51 for the surfactant with 5 mM metal salt corresponding to the measured maximum signal intensity of 114 counts sec^{-1} at the CMC relative to the surface coverage of the pure surfactant with a maximum intensity of 221 counts sec^{-1}. This number has been determined with the assumption that the Raman signal intensity is linearly related to the molecules adsorbed at the interface, and that the Raman scattering signal acquisition parameters are kept identical. The surface coverage

decrease might be explained by the change in free energy of adsorption as determined from the adsorption isotherm model and energetically more favorable surfactant aggregation in solution that affects both the number density and structure of the adsorbed surfactant. Similar effects of chloride containing electrolyte have been observed in the adsorption isotherm of cetyltrimethylammonium chloride.[2] This information alone does not allow deducing the exact nature of the structures, but gives hints towards more densely packed aggregates in solution with more favorable lowering of the energy by micellization relative to adsorption at the surface.

Two distinct regions are noticeable in the adsorption isotherm, only vaguely resembling the proposed classic two-step adsorption isotherm models, as observed by Tyrode et al. and Woods et al. with the adsorption of cetyltrimethylammonium bromide (CTAB) on silica surfaces,[55, 59, 60] and by Somasundaran et al. with the adsorption isotherms of non-ionic and anionic surfactants on alumina surfaces.[98] At very low concentrations from 1 μM to 5 μM, the presumably electrostatically driven adsorption mechanism [86] between charged surfactant head groups and the small negative charge on the silica surface almost disappears upon addition of magnesium salt to the solution due to surface charge neutralization by the positively charged magnesium ions. At the onset of the surface critical aggregate concentration (scac),[86] at 10 μM, surfactant adsorption is promoted by the hydrophobic effect, and reaches equilibrium conditions at the CMC of 50 μM, with minimum free energy of micellization in solution and adsorption to the silica surface.[108]

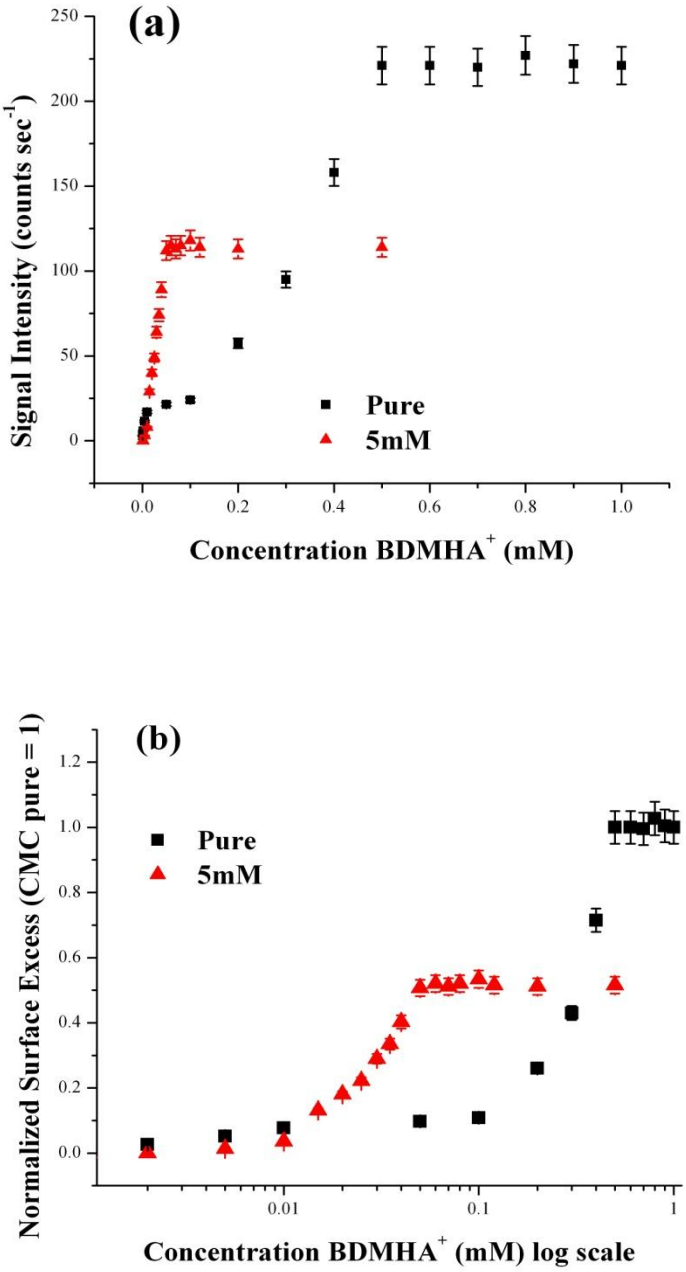

Fig. 6.6.1: Adsorption isotherms of the pure surfactant and surfactant + 5 mM $MgCl_2$

(a) CH_2 intensity in counts sec^{-1} vs. concentration
(b) Normalized surface excess vs. concentration – log scale

Addition of electrolytes to surfactant solutions always leads to exponentially decreasing CMC due to several contributing factors.[108] The magnitude of free energy of micellization decreases due to more favorable packing of the surfactant monomers into aggregates with more efficient screening of the charged head groups by the mono- or divalent electrolyte, resulting in a higher aggregation number: N_{agg}. The average aggregation number N_{agg} for the pure $BDMHA^{+}Cl^{-}$ has been estimated in the range of 90, 102, and 110.[101, 152], depending on the study and the methods employed, and is known to increase with increasing concentration of electrolyte.[108, 152] In case of $BDMHA^{+}$, the effects are already significant at an electrolyte concentration of 5 mM that is actually lower than the typical concentrations of at least 10mM,[86, 153] but sufficient to attenuate the repulsive forces between the head groups of the surfactant monomers and lower the overall free energy of micellization further by transferring a larger fraction of the hydrophobic hydrocarbon chains from solution into the surfactant aggregate interior.[108]

Addition of 10, 50, and 100 mM of $MgCl_2$ leads to further CMC reduction to 0.042 mM, 0.018 mM, and 0.014 mM, respectively, as estimated from the plot and curve fitting (Fig. 6.6.2.); interestingly, an increasing trend of the normalized surface coverage to 0.59, 0.66, and 0.69, is observed for the surfactant containing 10, 50, and 100 mM of metal salt (Table 6.6.1), respectively, with high adsorption slopes ($d\Gamma/d \log [conc]$), that represent the hemi-micelle aggregation region (Figs. 6.6.2. (a) and (b)). The lower plateau region in the adsorption isotherm of the surfactant with 50 mM electrolyte concentration reappears again at a concentration of 2 μM, and also for the surfactant with 100 mM of electrolyte addition at 5 μM (although at the analytical detection limit). This suggests that

hydrophobic effects are already present at these low concentrations, since adsorption due to electrostatic attraction is unlikely.

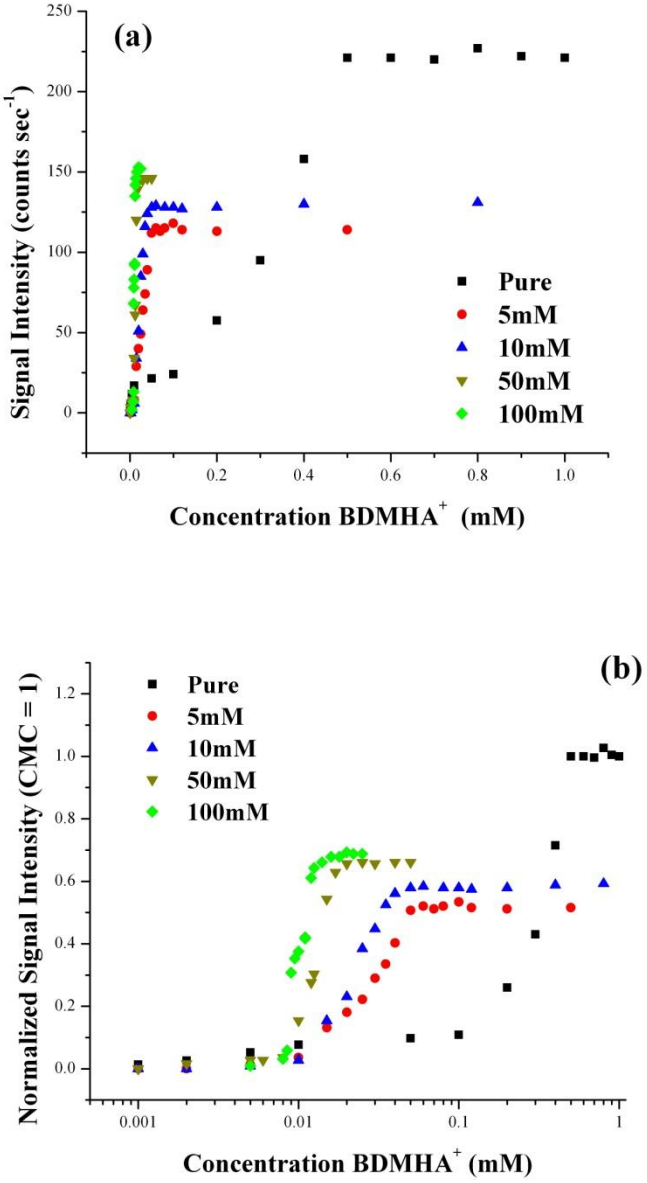

Fig. 6.6.2: Adsorption isotherms of the pure surfactant (■); surfactant + 5 (●); + 10 (▲); + 50 (▼); and + 100 mM (♦) $MgCl_2$ – error bars are omitted for clarity
(a) CH_2 intensity in counts sec^{-1} vs. concentration – linear scale
(b) Normalized signal intensity vs. concentration – log scale

The isotherm of the surfactant with the high metal salt concentration of 100 mM reveals unusual, non-linear behavior in the center portion of the adsorption slope as compared to the remaining isotherms. The critical experiments were duplicated using two independent surfactant mixtures to confirm the validity of the isotherm in the aggregate formation region that exhibits a breakpoint in the usually linear adsorption slope (Fig.6.6.3.) comparable to the four-step adsorption model, proposed by several authors for certain types of surfactant-interface interactions.[4, 98, 101]

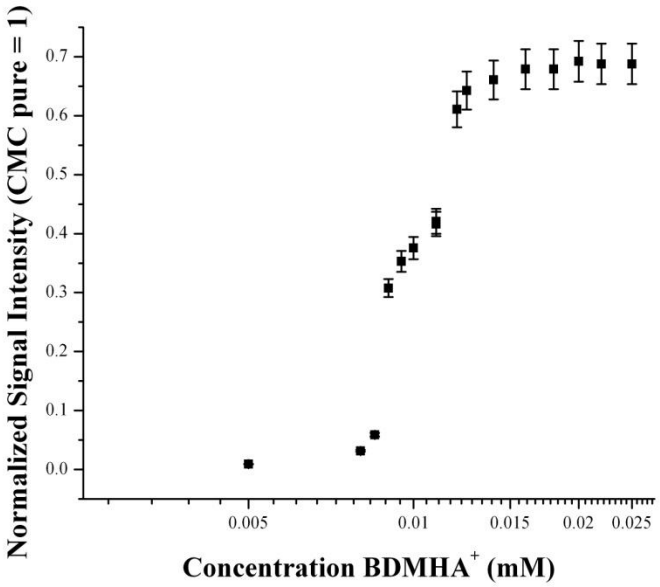

Fig. 6.6.3: Adsorption isotherm of the surfactant+100 mM $MgCl_2$ - normalized intensity

The lowest portion of the genuine four-step-model is, however, absent in the adsorption isotherm of this study, possibly lying below the detection limit of the TIR Raman system, despite its high sensitivity.

The exponentially decreasing CMC value follows the classic description of the CMC vs. electrolyte relationship:

$$\log CMC = a - b \log [C] \qquad (6.6.1) \qquad \text{or} \qquad CMC = C * e^{a-b} \qquad (6.6.2)$$

where "a" and "b" are surface and electrolyte-surfactant specific constants and [C] represents the electrolyte concentration. The value of "b" = - 0.45 (R^2 =0.995), as shown in Fig. 6.6.4, is lower in magnitude than the expected range of -0.6 to -1.2 reported in literature for common surfactant-electrolyte systems, implying less efficient screening of the head group by the magnesium salt.

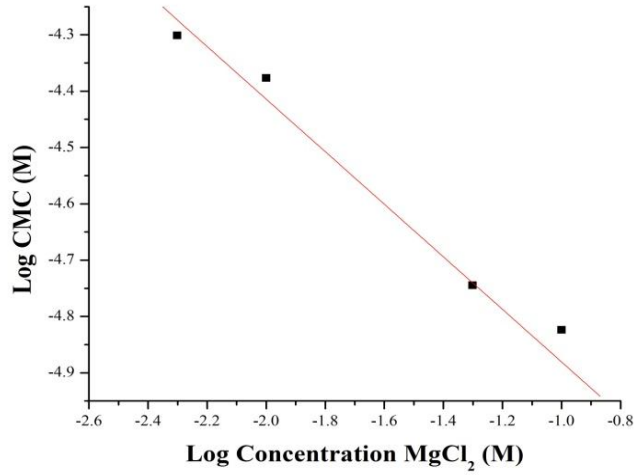

Fig. 6.6.4. : CMC vs. electrolyte concentration for $BDMHA^+$-$MgCl_2$

6.7. Adsorption isotherm models

The adsorption isotherms were fitted to a modified Langmuir isotherm or so-called Frumkin-Fowler-Guggenheim isotherm where the general expressions for the modified Langmuir constant in eqs (3.11.1) and (3.11.2) were rearranged and the exponential energy term n E θ/RT was redefined as g θ, where g = n E/RT. n refers to the number of neighboring molecules at the surface, E is the interaction energy, R and T have their usual meaning, and θ refers to the fractional surface coverage (eq 6.7.1).

$$\ln(\frac{\theta}{1-\theta}) - g\theta = \ln K_{mod} + \ln[C] \qquad (6.7.1)$$

The measured values for the equilibrium constant were determined by plotting ln (θ/(1-θ) – gθ) vs. ln [C] and varying the parameter "g" to obtain the best linear fit correlation and determine the best fit "g" parameter and then the modified adsorption constant from the intercept. The fitted isotherms and computed adsorption equilibrium for the pure surfactant showed a change in Gibbs free energy of adsorption of –19 (±3) kJ mol^{-1}. The free energy of micellization (ΔG°_{mic}) is reported as -43 kJ mol^{-1} in literature for the pure surfactant,[109] and no attempt was made to determine it from the current data, since additional work is required for obtaining an accurate value for "α". The association or dissociation parameter "α", that describes the ratio of bound vs. dissociated counter ions relative to the number of surfactant molecules in the micellar aggregate, needs to be determined by a separate technique, i.e., conductivity measurement.[102] A calculation based on literature values is not informative, since the "α" value has been listed in

literature as varying between 0.22 , 0.40[101] and 0.49,[112, 146], depending on the methods that were used, and would not apply to the surfactant with addition of the metal salt.

The Langmuir adsorption constant determined from the fitted data for the pure surfactant does not indicate any specific deviation from a typical Langmuir adsorption model and no interaction energy parameter was defined. The interaction energy parameter for the surfactant with small addition of the magnesium salt shows only a small value of 0.5, whereas higher metal salt additions of 10 and 50 mM gave an interaction energy parameter of 2.5 and 3.0; the highest metal salt concentration did not exhibit any further increase, it actually decreased again to 2.5, showing a similar trend downward as the equilibrium adsorption constant itself, as observed in other studies with high electrolyte concentrations.[87] The generally increasing interaction energy arises from the high electrolyte concentrations providing the conditions for higher aggregation numbers and denser packing of the surfactant in solution and at the surface, with favorable interaction between the neighboring molecules due to attenuation of the repulsive electrostatic forces by the chloride anions, and increasing equilibrium adsorption constants and the magnitude of free energy of adsorption.

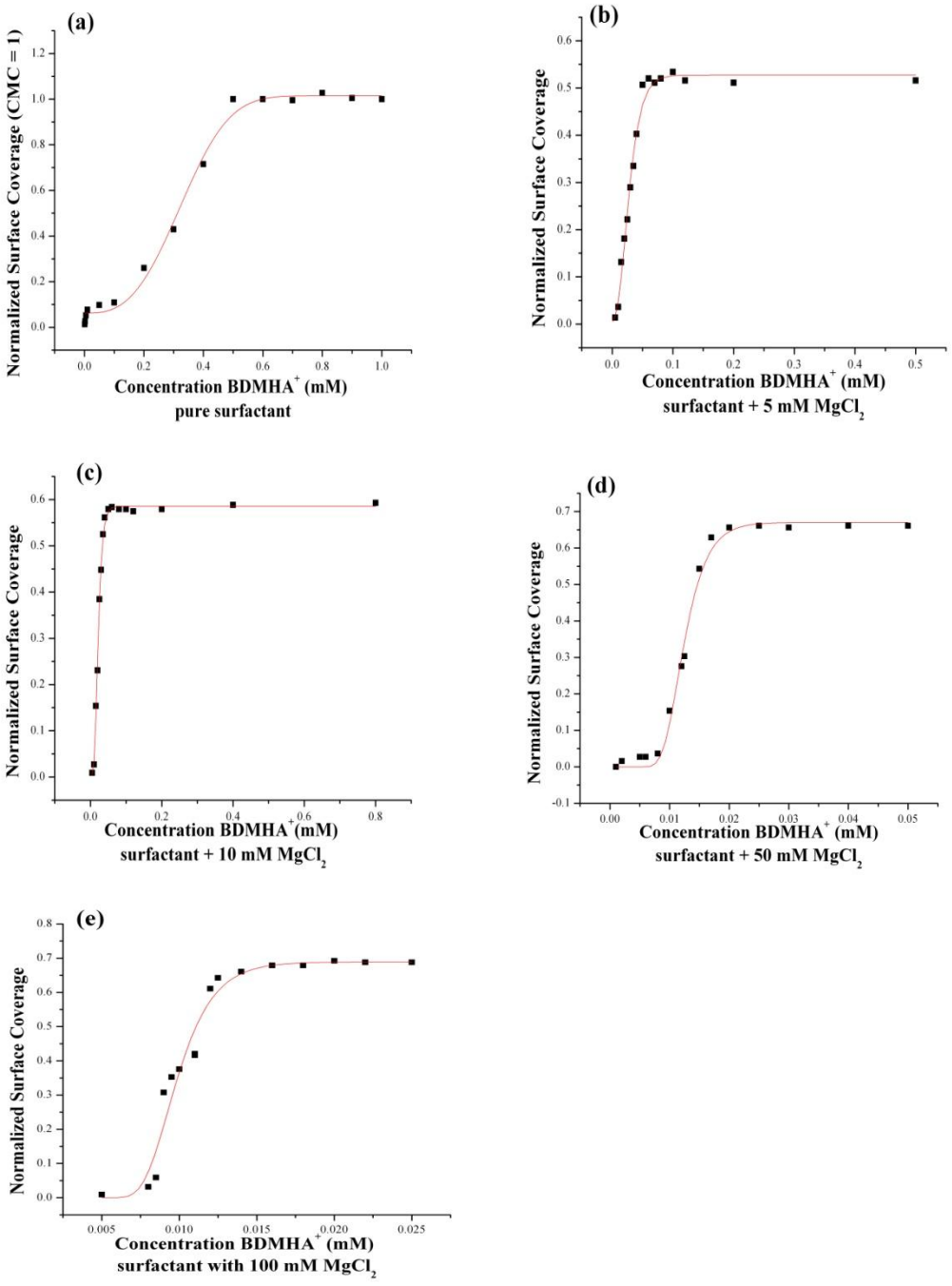

Fig. 6.7.1.: Adsorption isotherms fitted to the FFG adsorption model using sigmoidal fitting models

The change in the Gibbs free energy of adsorption of – 19 (± 3) kJ mol^{-1} for the pure surfactant decreased to -25 (±2) kJ mol^{-1} for the surfactant + 5 mM magnesium salt, and to -39 (± 8) kJ mol^{-1} for surfactant+10 mM of metal salt additive, reaching its minimum with a metal salt addition of 50 mM that showed the most favorable change in free energy of adsorption of -44 (±8) kJ mol^{-1} (Table 2), which is actually comparable to the free energy of micellization, reported in literature for this compound. The change in Gibbs free energy of adsorption of the surfactant with 100 mM of magnesium salt increased again to –42 (±1) kJ mol^{-1}, that is consistent with a decrease of the interaction parameter and indicates a trend reversal of the adsorption behavior at high electrolyte concentrations.

The adsorption isotherms show similar shapes, but with some differences in their plateau regions. Both the pure surfactant, and the surfactant with the highest metal salt addition, show two distinct plateau regions, the surfactant with 50 mM exhibits a minor plateau at low concentrations besides the second plateau region above the CMC, whereas 5 and 10 mM of metal salt addition show one single plateau region beyond the CMC region after maximum surface coverage is attained. The lack of surface excess in the low concentration region suggests absence of the electrostatic attraction mechanism in all isotherms of surfactant with electrolyte addition, and absence of hydrophobic effects at the low surfactant and electrolyte concentrations for the surfactant with 5 and 10 mM of electrolyte.

Table 6.7.1: Adsorption energy parameters from adsorption isotherm fitting

Surfactant System	$\Delta\ \Delta G^{\circ}_{ads}$ (kJ mol^{-1})	K_{mod}	K_{mod} R^2	g	K_L	CMC (μM)	Γ_{max} CMC=1
Pure Surfactant	-19 ± 3	$1.4*10^5$ ±1,400	0.998	N.A.	K_{mod}	500 ± 5	1.00
Surfactant + 5 mM $MgCl_2$	-25 ± 2	$1..4*10^6$ ± $2*10^4$	0.998	0.5	$K_{mod}\, e^{-0.5\theta}$	50 ± 0.5	0.51
Surfactant + 10mM $MgCl_2$	-39 ± 8	$4.2*10^8$ ±$5.8*10^6$	0.990	2.5	$K_{mod}\, e^{-2.5\theta}$	42 ± 0.5	0.59
Surfactant + 50 mM $MgCl_2$	-44 ± 8	$2.6*10^9$ ±$56.6*10^6$	0.991	3	$K_{mod}\, e^{-3.0\theta}$	18 ± 0.5	0.66
Surfactant + 100mM $MgCl_2$	-42 ± 1	$1.9*10^9$ ±$2.7*10^7$	0.998	2.5	$K_{mod}\, e^{-2.5\theta}$	14 ± 0.4	0.69

The isotherms of all five systems studied were curve fitted to the respective Langmuir or modified Langmuir model (Fig. 6.7.1). The adsorption constants K_{mod}, presented in Table 2, increase proportional to the metal salt added, with the exception of the surfactant with 100 mM of magnesium salt, in increments of one to two orders of magnitude with increasing electrolyte concentration, relative to the adsorption of the pure surfactant at the bare silica surface. They are valid under the assumption that the electrolyte activity coefficient is equal to unity and corrections would be negligible at these small concentration if no further interactions between the species in solution are involved; since some interferences might be expected with ionic surfactants, there might be a slight bias in these values.[111]

6.8. Orientational analysis of surfactant with electrolyte addition

Orientational analysis was carried out by evaluating p- and s-polarized spectra intensity ratio changes of the CH_2 and antisymmetric CH_3 vibrational modes of one of the adsorption isotherm studies, namely the surfactant with 50 mM of metal salt addition, in s-polarized sampling geometry with a polarizer integrated in the light collection optics along the y-axis (S_y), and duplicating three of the surfactant concentrations, 0.012, 0.017, and 0.050 mM in p-polarized geometry (P_{x+y}). The three surfactant concentrations chosen represent the critical concentrations at the onset of aggregate formation at the bottom of the adsorption isotherm slope, before the CMC, and in the adsorption equilibrium (plateau) region above the CMC (Figs 6.8.1. (a) and (b)).

It needs to be pointed out that a complete orientational analysis is not feasible, since the necessary weighted factors for s- and p-polarized spectra – on the excitation side, for the electric field strength of the individual field vectors, and on the collection side, grating efficiency - are not available and the absolute signal intensities are concentration dependent. The objective of this orientational and structural analysis was to compare the intensity ratios of the relevant vibrational modes, and to identify potential changes or trends as function of concentrations and time.

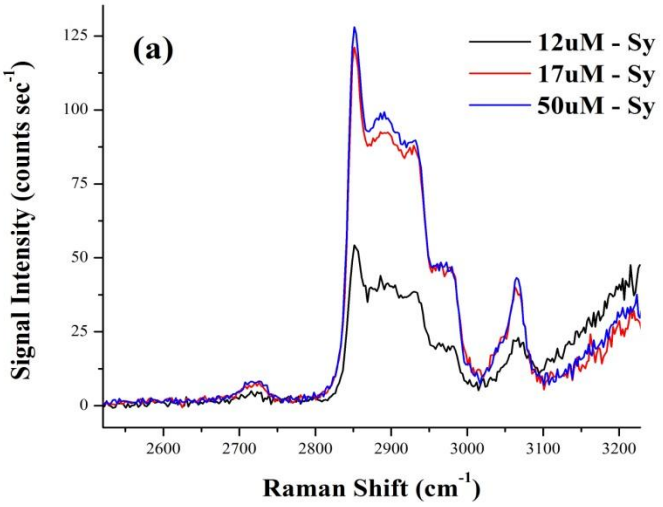

Fig.: 6.8.1 (a): Spectral analysis and comparison of representative spectra acquired at 0.012 mM, 0.017 mM, and 0.050 mM concentrations of the surfactant with 50 mM $MgCl_2$ in (a) s-polarized sampling geometry

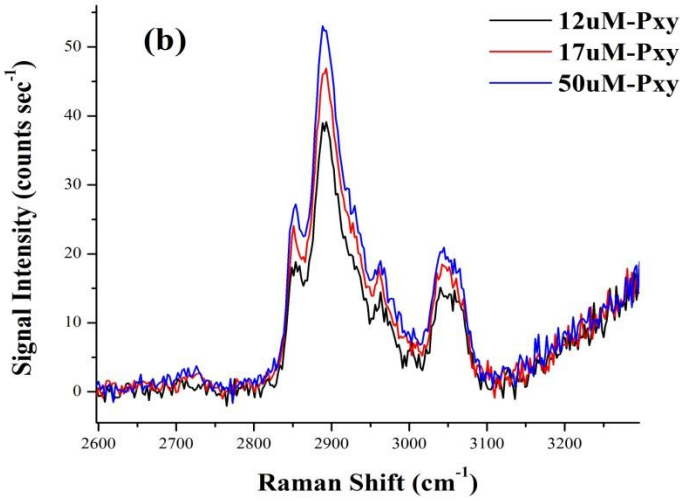

Fig. 6.8.1 (b): Spectral analysis and comparison of representative spectra acquired at 0.012 mM, 0.017 mM, and 0.050 mM concentrations of the surfactant with 50 mM $MgCl_2$ in (b) p-polarized geometry

The overlaid spectral sets in s- and p-polarized modes show a slight decrease in intensity ratio of the anti-symmetric CH_3 stretch vs. the symmetric CH_2 stretching mode in the p-polarized spectra when going from the lowest surfactant concentration of 0.012 mM to 0.050 mM (Table 6.8.1.). An unambiguous interpretation in terms of increased structural ordering, however, is not possible, since the decreasing trend of the signal intensity ratio is only found within the p-polarized spectra. Conformational transitions from a disordered gauche configuration to a more organized trans arrangement of the alkyl-chains are not confirmed due to lacking intensity ratio changes within the s-polarized spectra.

Table 6.8.1: Vibrational mode intensity ratios from p- and s-polarized spectra of surfactant with 50 mM of $MgCl_2$

Concentration Surfactant	**0.012 mM**	**0.017 mM**	**0.050 mM**
Sy/Sy Ratio			
$CH_3\ \nu_{as}/CH_2\ \nu_s$	0.41±0.03	0.41±0.02	0.39±0.01
Pxy/Pxy Ratio			
$CH_3\ \nu_{as}/CH_2\ \nu_s$	0.78±0.15	0.74±0.12	0.69±0.10
$CH_2\ \nu_{as}/CH_2\ \nu_s$	2.01±0.21	1.96±0.20	1.92±0.17
Pxy/Sy Ratio			
$CH_3\ \nu_{as}/CH_3\ \nu_{as}$	0.64±0.11	0.43±0.05	0.36±0.04
$CH_2\ \nu_{as}\ /\ CH_2\ \nu_{as}$	0.85±0.10	0.58±0.03	0.52±0.02
$CH_2\ \nu_s\ /\ CH_2\ \nu_s$	0.33±0.04	0.23±0.02	0.20±0.02

No shift of the Raman peak positions to lower frequency was observed,[77, 117] that would be characteristic for a transition from less ordered molecular surface structures with gauche defects in the alkyl chains to a more rigid and ordered configuration. The signal

intensity ratios of the anti-symmetric vs. symmetric methylene stretching modes of approx. 2, as observed in p-polarization geometry, hint towards more rigid structural arrangement of the surfactant at the surface, but intensity ratio changes within one polarization mode are insufficient for assigning any degree of ordering to the molecules adsorbed at the silica surface.[154-156]

The signal intensity ratios observed between s- and p-polarized geometries might be indicative of increased molecular ordering relative to each other with decreasing average tilt angles from the surface normal, that might point towards transitions to an elongated aggregate or globular micelle, similar to observations made in previous studies related to long alkyl chain surfactants,[55] and cationic surfactants in the presence of electrolytes, where the electrolyte reduces both the effective charge and area of the head group, giving way to more elongated micelle structures.[101] Based on literature data, this structural change is expected to occur at concentrations several times the CMC, that have not been included in this study. Extremely high concentrations might lead to other TIR related interfering signal effects, as discussed in section 2.5. The negligible shifts in frequency or peak positions, observed with the prominent vibrational modes, do not confirm conformational or orientational change to a more organized structure; these shifts – some of them being positive - are much smaller than those reported in literature for a typical transition to a more ordered arrangement (Table 4).[77, 156] This finding is also in agreement with the known behavior of surfactants with long alkyl chains that adopt the energetically most favorable configuration for optimum packing that requires bending of the alkyl chains and accommodation of the benzyl ligand.[92, 112, 157]

Table 6.8.2: Frequency shift observed in the concentration range of 0.012 to 0.050 mM

Δ cm^{-1}	P_{xy}	S_y
CH_2 ν_{vs}	-1.5	+0.5
CH_2 ν_{as}	-1.8	+4.0
CH_3 ν_{as}	-2.0	-1.0

6.9. Effects of magnesium chloride ions on the interfacial water structure

The Raman spectral baseline that usually exhibits a straight line with the water background signal corrected, showed a positive offset of the water band in the frequency

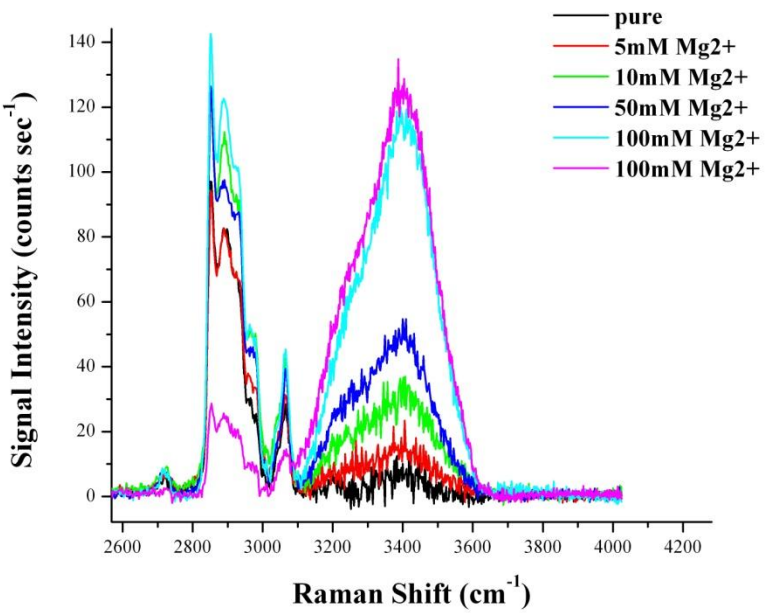

Fig. 6.9.1: Offset water signal as function of magnesium ion concentration.

region of 3300-3400 cm^{-1}, that increased reproducibly and proportional to the increase in magnesium chloride concentration, but was independent of the surfactant concentration (Fig. 6.9.1.). This offset water signal cannot have its origin in the surfactant adsorption, since no water signal deviation was observed in experimental work that involved the pure surfactant. It typically indicates a change at the silica-water interface relative to the background signal obtained from a pure silica-water interface, and, in this experimental set-up, a change in the water structure within the electrical double-layer and the bulk within the probing depth of 100 nm, due to the water structure modifying properties of magnesium chloride.

The spectral analysis reproducibly shows an increase of the vibrational band (peak maximum at 3400 cm^{-1}) that corresponds to the less symmetric and less ordered water-like structure,[128] but without significant effects on the more symmetric, ice-like band (at 3200 cm^{-1}) in s-polarized geometry. This unusual enhancement of the less symmetric vs. the more symmetric bands emphasizes the magnesium ion's water-structure breaking property that causes reorientation of the water molecules in the electrical double layer at the interface and in the bulk to a less H-bonded water structure with higher susceptibility of the water molecule's low symmetry vibrational modes to the incident electric field. These phenomena at the silica-water interface have previously been reported in context with divalent metal ion effects, showing water signal attenuating effects for magnesium ion at the silica-water interface at neutral pH conditions.[129] The enhancement of the liquid-like low symmetry vibrational bands due to increased disruption of the tetrahedral

H-bonded water structure is consistent with previous studies of the water structure at silica-water interfaces using SFG techniques.[158-160]

IR and Raman spectroscopic studies by Allen et al. of the symmetric vs. asymmetric vibrational water signal intensities as a function of metal salt addition in the bulk aqueous solution found a similar decline of the ice-like water vibrational signal relative to the more liquid-like band. Parallel polarized Raman spectra as well as perpendicularly polarized analysis showed similar trends, as observed in the present study, of the water vibrational response to metal salt addition in the bulk solution,[161] from the solvation of both cationic and anionic species and their H-bonding disrupting properties. IR spectra did not show any change in the spectral distribution, most likely due to different IR selection rules with lower sensitivity for symmetric vibrational modes.[161, 162]

Both cationic and anionic species present at the interface and in the bulk might be responsible for the signal ratio change of the ice-like water band at 3200 cm^{-1} vs. the liquid-like band that decreased proportional to the solute concentration added to the neat liquid.[163] Studies using X-ray absorption spectroscopy (XAS) for specifically studying the anion function, confirm that the anionic halide ions contribute to the water structure distortion,[164] as much as other anionic species of relatively small size, i.e., nitrates, that, according to early research studies affect the liquid-like band at 3400 cm^{-1}.[162, 165] These findings would agree with the TIR Raman spectra that show no significant deviation of the pure water background signal (neat water) vs. the signal with surfactant added, since the surfactant concentrations did not exceed 1mM in solution and the contributions from

the chloride originating from the surfactant itself, are negligible. This is not the case with addition of magnesium chloride in the concentration range of 5 to 100 mM, where both cation and anions exceed by far the surfactant concentrations, and both contribute to ionic species in solution.

6.10. Effects of magnesium chloride on adsorption kinetics

The overall adsorption kinetics may be summarized as follows: magnesium salt addition favored faster adsorption kinetics with faster attainment of the adsorption equilibrium, in particular, in the concentration region close to and above the CMC. These faster kinetics are, however, referenced to the pure surfactant, where the typical equilibration times were in the range of 2 hours for concentrations below the CMC, and around 4 – 6 hrs for concentrations close and above the CMC, that could be reduced to 1 – 2 hrs or less depending on the amount of metal salt added (Fig. 6.10.1 (a)). The slow adsorption kinetics cannot be explained by electrostatic effects, but better by energy constraints (also enthalpy and entropy) related to the surfactant monomers rearrangement within the micellar core,[2] that are attenuated by electrolyte charge screening properties. The kinetic enhancement is most pronounced for the surfactant with 10 mM of electrolyte addition, followed by surfactant with 5 mM and 50 mM of $MgCl_2$ addition, as shown in Fig. 6.10.1. (a). Addition of higher amounts of metal salt did not show any improvement on the adsorption kinetics, but again longer equilibration times that are comparable to the pure surfactant at low concentrations below the CMC. This trend reversal is reflected

both in the decreasing value of the adsorption constant, decreasing interaction parameter, and confirmed by the short time scale study that covers only the initial phase of the adsorption process (Fig. 6.10.1. (b)). It implies that adsorption is enhanced by moderate addition of the metal salt that attenuates the repulsive interaction between the charged head groups, but further increase of the electrolyte concentrations and thus the ionic strength of the solution does not result in faster equilibration times, due to steric hindrance and surfactant monomer packing constraints.

A more detailed kinetic analysis focused on the initial adsorption rates of all five systems under modified experimental conditions. This independent part of the study was conducted with increased signal intensity by doubling the laser power to 1.0 W at the laser head, and short acquisition times of 30 sec for each spectrum, to probe the initial adsorption behavior that could not be covered with 10 min acquisition intervals. A significant portion of the surfactant adsorbs within the first minute, (Fig. 6.10.1. (b)) and subsequent adsorption is extremely slow, even after one or two minutes. The surfactant, both in its pure form and with low metal salt added, shows initial fast adsorption of a major fraction of the monomers present in solution followed by slower adsorption kinetics before equilibrium conditions are reached, that are slow for the pure surfactant, and increase in the order of 10 mM addition, then followed by 5 and 50 mM of metal salt addition, with decreasing kinetics again observed for the surfactant with 100 mM of additive. For illustration, the adsorption kinetics of the five systems are shown side-by-side for comparison of the adsorption kinetics on two different time scales; once, at 10-minute intervals, analogue to the isotherm experiments, and in the second part, at 30-

second intervals, that covers the initial time frame of adsorption under modified experimental conditions, after normalizing the signal intensities by setting the maximum signal equal to unity.

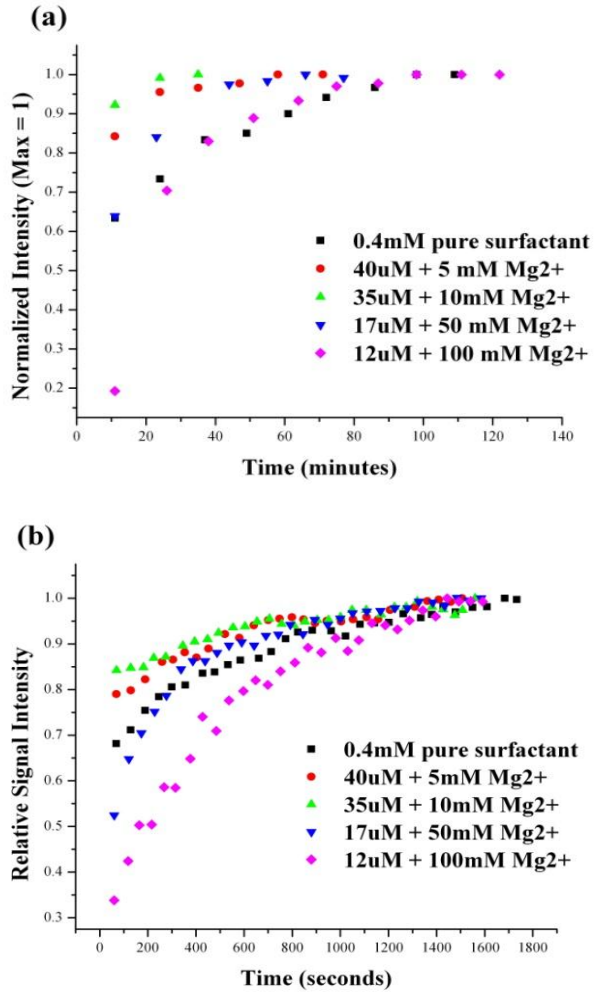

Fig. 6.10.1: Adsorption kinetics of 0.4 mM pure surfactant and
0.040 mM surfactant+ 5 mM $MgCl_2$;
0.035 mM surfactant+ 10 mM $MgCl_2$;
0.017 mM surfactant + 100 mM $MgCl_2$;
0.012 mM surfactant + 100 mM $MgCl_2$

(a) 10 min. acquisition times (b) 30 sec acquisition times

The trends of kinetic enhancement and the trend reversal when adding 100 mM of electrolyte are apparent from both plots, despite some fluctuations in the measurements, since the gradient of signal intensity vs. time in seconds, is almost of the same magnitude as the standard deviation of the spectral base line noise.

6.11. Adsorption at the OTS-coated hydrophobic silica surface

6.11.1. Characterization of the OTS-coated silica surface

Silica surface properties were modulated by coating the bare silica surface with an OTS monolayer: the OTS monolayer was deposited onto the silica surface by reacting the pretreated and thoroughly cleaned silica surface (in 70/30 v/v H_2SO_4/H_2O_2) with 1 mM of OTS in toluene for 30 minutes. The silica surface was rinsed with pure solvent to remove unreacted material followed by several rinses with 18.2 MΩ ultra-pure Millipore water. Confirmation of the OTS monolayer presence (monolayer thickness estimated at 2 nm) was obtained by Raman spectral analysis of the OTS-silica-air interface before introducing the aqueous phase into the sample cell (Fig. 6.11.1). The difference in absolute signal intensities in s-polarized vs. p-polarized Raman spectra demonstrates the higher susceptibility of the symmetric derived Raman tensor and increased Raman scattering collection efficiency in Sy sampling geometry, as seen with the stronger symmetric methylene vibrational modes in s-polarized geometry vs. the p-polarized incident light. Both spectra in S_y and P_{x+y} sampling geometry were taken at 1.0 W laser output power and a smaller incident angle of 53˚ as compared to the angle of incidence of

73˚ used for experiments at the silica-water interface, since the critical angle for the silica-air interface is determined as 43.2˚. The intensity ratio of 0.95 obtained from the anti-symmetric vs. symmetric methylene stretching modes (S_y geometry) at the silica-air and also silica-water interface, a ratio of 2 in P_{x+y} sampling geometry, and the P_{x+y}/S_y intensity ratio of the anti-symmetric methylene vibrations of 0.5 (that would correspond to a ratio of 1, if factoring in the lower scattering intensity in p-polarized spectra), supports a relatively ordered OTS monolayer. The Raman spectrum in Fig. 6.11.2 illustrates the background signal of the OTS-silica-water interface, as obtained with the typical acquisition settings of the experimental study, at 1.0 W laser output power and an incident angle of 73˚C. The refractive index and thus the critical angle are not expected to change after application of the OTS monolayer with a layer thickness reported between 1.7 and 2.33 nm[15, 166, 167] depending on the surface coverage[156] and a refractive index of 1.48 that is very close to the silica material itself.[157]

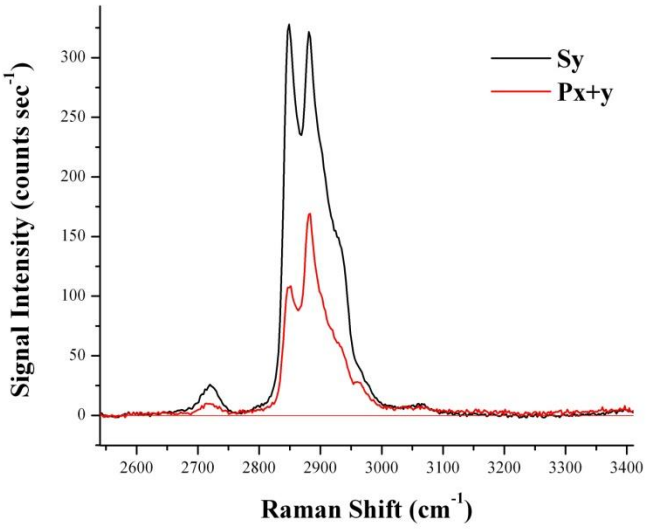

Fig. 6.11.1.1: OTS-silica-air interface in S_y and P_{x+y} sampling geometry

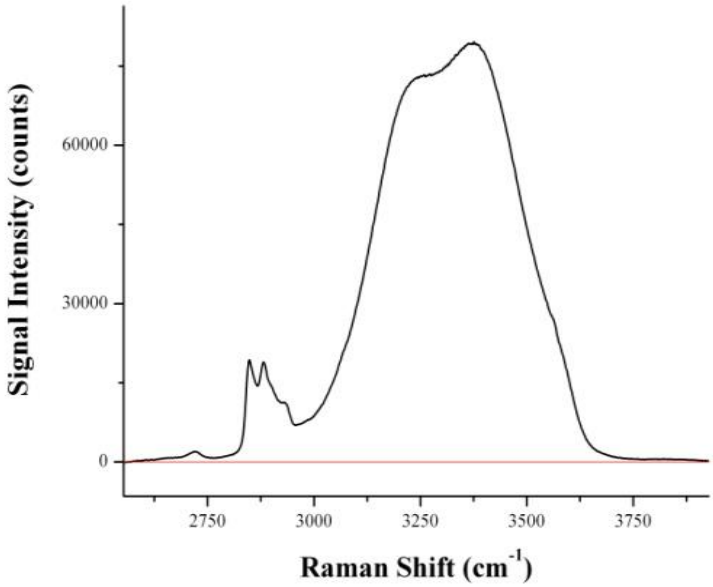

Fig. 6.11.1.2: OTS-silica-water background signal in S_y sampling geometry

The signal in p-polarized geometry is reduced by 40-50% relative to the s-polarized sampling configuration; both the symmetric nature of the Raman polarizability tensor, the sampling geometry and the grating efficiency might contribute to this intensity loss. First: the Raman tensor is a symmetric tensor that favors the interaction of the derived symmetric Raman tensor elements with incident polarized light. Raman signals are further attenuated, since signals originating from P_z polarization are not scattered into the solid angle of the collection optics, as discussed in section 2.4. Second: signal strength further depends on the grating efficiency relative to the respective modes of polarization of incident light. The currently used holographic grating (Kaiser Optical Instruments) is not specified for a particular polarization direction. Separate experimental work is required to evaluate grating efficiency relative to the polarization of the incident signal intensities. Typical variations of up to 20% have been reported for grating efficiencies of p- vs. s-polarized incident light, but vary with grating type, and need to be determined individually.

Monolayer presence was further confirmed by a non-linear and highly surface specific spectroscopic technique, sum frequency generation (SFG), with spectra taken in the two most relevant polarization combinations, ssp and asymmetric (ppp) modes (Figs. 6.11.1.3 (a) and (b)).

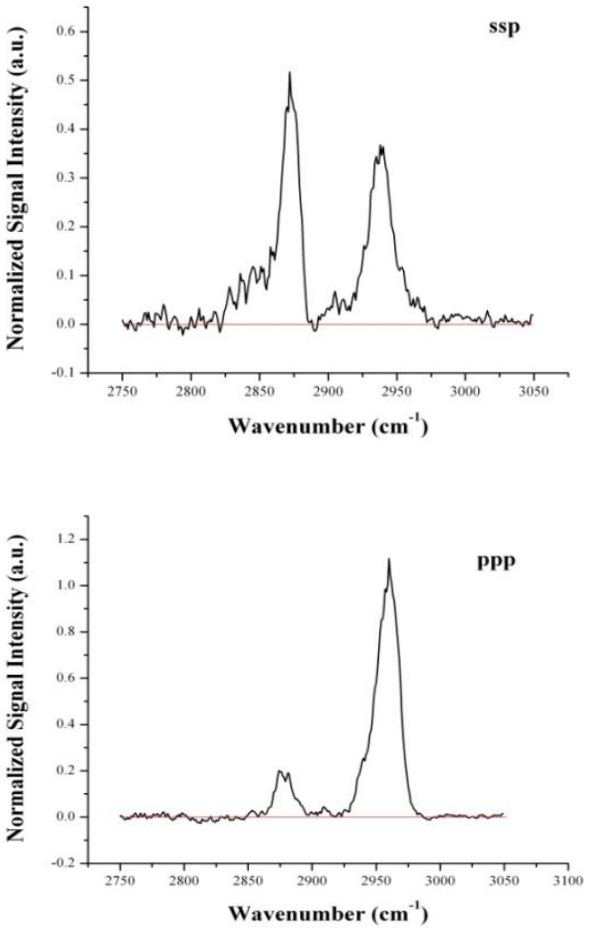

Fig. 6.11.1.3: SFG analysis of the OTS-silica-air interface: (a) ssp polarization
(b) ppp polarization

The symmetric and anti-symmetric vibrational methylene stretching modes are not present in the SFG spectrum obtained from the OTS-silica-air interface indicating that these groups are centro-symmetric relative to the surface. The non-linear SFG technique is sensitive towards vibrational modes that are both IR and Raman active, i.e., vibrational modes that do not possess an inversion center.[27, 51, 75] The lack of the methylene stretching modes supports an ordered arrangement of the long alkyl chain molecules at

the silica-air interface with the methylene vibrational modes being centrosymmetric relative to the surface, and signals cancel each other. The dominant vibrational modes seen both in ssp and ppp polarization modes are the anti-symmetric terminal methyl vibrational mode at 2871 cm^{-1}, and its Fermi resonance at 2938 cm^{-1} that agree reasonably well with literature values and SFG spectra of OTS monolayers on silica substrates.[167, 168]

6.12. Spectral analysis of $BDMHA^{+}Cl^{-}$ at the hydrophobic silica-water interface

The amplitudes of the benzyl stretching mode at 3060 cm^{-1} were used as the primary indicators of the adsorption behavior. The signal intensities of these vibrational stretching modes were sufficiently strong to obtain the desired information in s-polarized geometry with a 3 counts sec^{-1} limit of detection at a S/N ratio of 3 (noise standard deviation of 1.0 counts sec^{-1}) that corresponds to a minimum surfactant concentration of 0.5 μM of adsorption of the surfactant with metal salt added (Figs 6.13.1. and 6.14.1). The intensities of the symmetric CH_2 vibrational modes, although dominating the Raman spectra, were not used as input for the adsorption isotherms, since they coincide with the same vibrational modes of the OTS monolayer and might introduce a bias in the isotherms, even with reliable laser stability and adequate background correction. Fig.6.12.1. presents the fitted Raman spectrum obtained with s-polarized incident laser excitation from the 0.32 mM surfactant concentration in S_y sampling geometry (apparent CMC of the pure surfactant at the OTS-silica interface), with the polarizer in the

collection optics set along the y-axis. The spectral range covers the C-H stretching region with peak assignments for the relevant vibrational modes in the high frequency C-H stretching region summarized in Table 6.12.1. The fitted Gaussian spectrum is shown from the analysis of the compound adsorbed at the OTS-coated silica surface, after background correction; its primary purpose is to illustrate the spectral similarity between

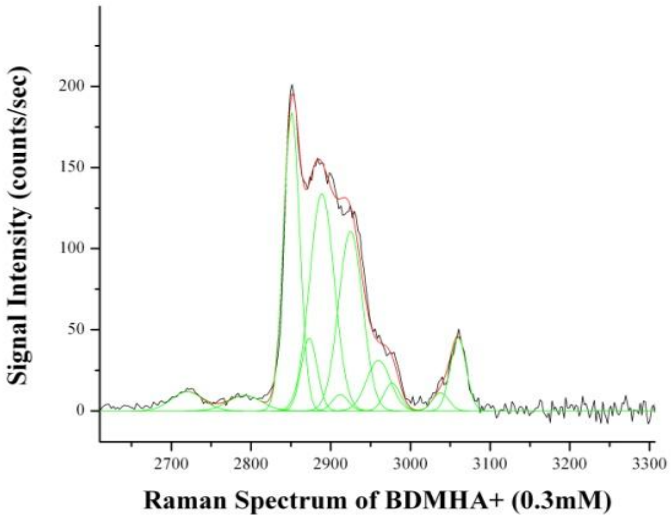

Fig. 6.12.1: Raman spectrum of the C-H stretching region (s-polarization)

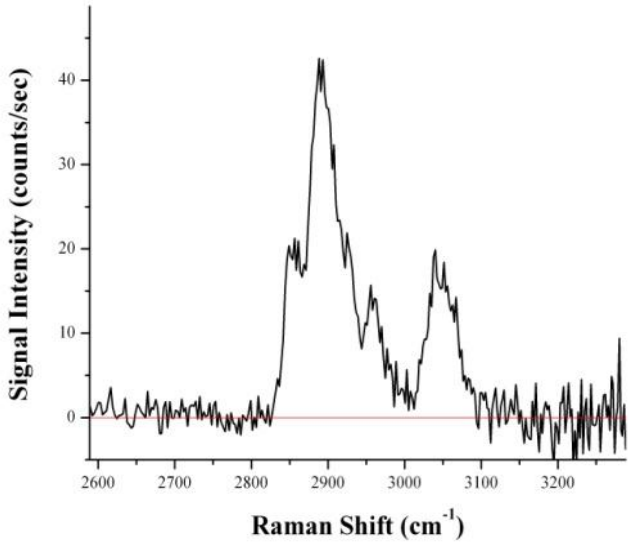

Fig. 6.12.2: Raman spectrum of the C-H stretching region (p-polarization)

the compound at the bare and at the hydrophobic silica, once background signals and their interference is accounted for. However, since methylene stretching vibrations are abundant in both OTS and the studied surfactant molecule, the most reliable signal is the unique benzyl stretching modes. Methylene signal intensities have been used for additional monitoring purposes. A Raman spectrum of a surfactant concentration of 0.040 mM with 5 mM of magnesium chloride addition, taken in P_{x+y} sampling geometry, is shown for comparison of both the overall signal intensity decrease and the signal intensity ratio change of the symmetric methylene vibrational modes vs. their anti-symmetric stretching modes (Fig. 6.12.2).

Table 6.12.1: Raman peak assignment [46, 51, 55, 169]

cm^{-1}	**Vibrational Mode:**	**Relative Intensity:**
2720	C-H ν_{δ} bend overtone	weak
2790	C-H ring comb. band	very weak
2851	CH_2 ν_s	strong
2873	CH_3 ν_s	very weak
2889	CH_2 ν_{as}	strong
2925	CH_2 ν_{sFR}	weak
2960	CH_3 ν_{as}	medium
2977	N-CH_3 ν_s	weak/medium
3038	N-CH_3 ν_{as}	weak/medium
3060	C-H ring ν_s	strong

The frequencies and peak assignments are comparable to those discussed for the surfactant at the bare silica surface. However, it appears that all vibrational modes shifted to lower frequencies by 1-4 cm^{-1}, relative to those observed at the bare silica. The symmetric methylene stretching modes at 2851 cm^{-1} are clearly dominating the Raman spectrum of the surfactant molecule in the C-H region, with high Raman scattering cross sections for the C-H stretching modes, in particular the symmetric vibrational modes (Table 6.12.1). The CH_3- symmetric stretching mode at 2873 cm^{-1} is barely distinguishable in the C-H stretching region and disappears in the fitted spectrum although its intrinsic Raman scattering cross section is higher than that for the methylene group, as discussed in section 6.3. The remaining vibrational modes have been assigned as described above in section 6.3. It should be pointed out, however, that the vibrational frequencies down-shifted by 1 – 2 cm^{-1}, possibly related to the different surface property. No spectral changes were observed after addition of the electrolyte to the sample

solution, with exception to those seen in the water signal offset, as previously discussed in section 6.9.

6.13. Structural analysis of $BDMHA^+Cl^-$ at the hydrophobic silica-water interface

Changes in signal intensity ratios were studied as part of the structural analysis of the pure surfactant. Signal intensity ratio changes of the CH_3 antisymmetric/CH_3 symmetric stretching modes as well as CH_2/CH_3 modes could not be identified in the s-polarized spectra btained from the pure surfactant at the OTS-silica-water interface in the concentration range of 20 μM to 0.6 mM (spectral overlays in Fig. 6.13.1. and 6.13.2.).

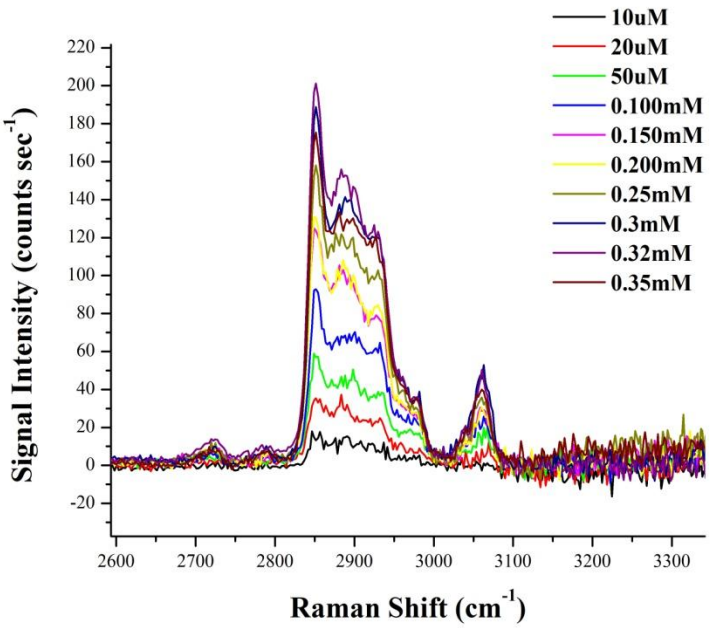

Fig. 6.13.1: Spectral overlay for surfactant concentrations ≤ **CMC**

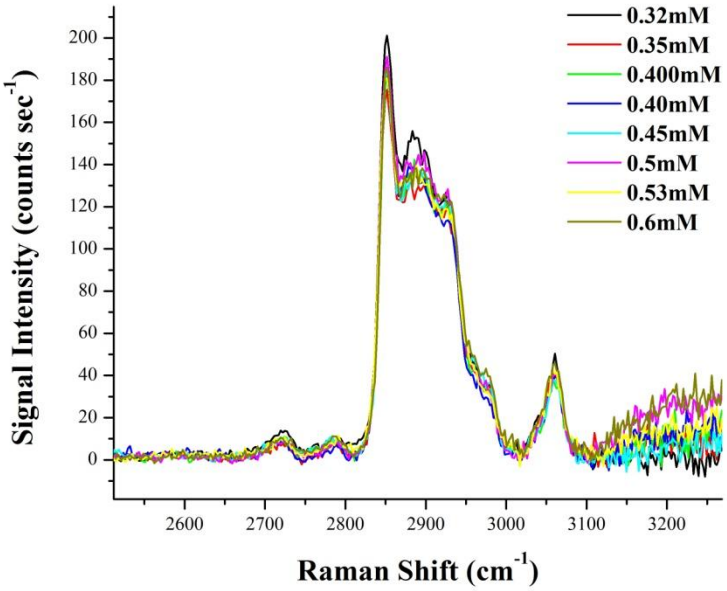

Fig. 6.13.2: Spectral overlay for surfactant concentrations ≥ CMC

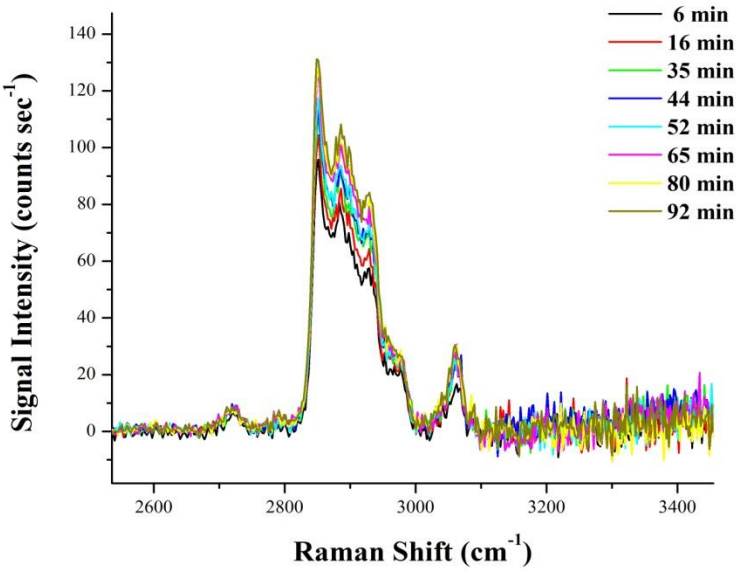

Fig. 6.13.3: $BDMHA^+$ at 0.20 mM: spectral evolution as function of time

No trends could be identified within the S_y polarized spectral set, neither as function of concentration (Figs. 6.13.1 and 6.13.2.), and thus increased surface coverage, nor as a function of time, demonstrated by the analysis of one single concentration (Fig. 6.13.3) of 0.20 mM. It represents the surfactant concentration in the upper portion of the adsorption slope with the most pronounced and slow adsorption kinetics.

6.14. Adsorption of pure $BDMHA^+Cl^-$ at the hydrophobic silica-water interface

Adsorption isotherms of the surfactant $BDMHA^+$ and adsorption models were based on the Raman scattering intensity of the benzyl vibrational mode at 3060 cm^{-1} obtained from spectral analysis (Fig. 6.13.1. and 6.13.2.).

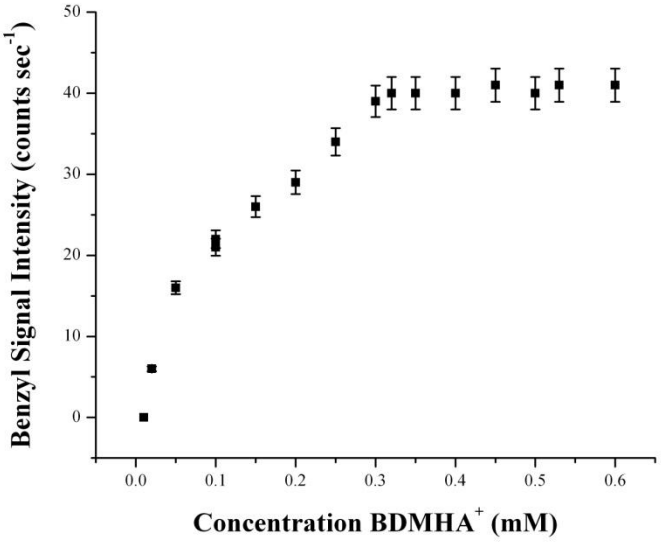

Fig. 6.14.1: Adsorption isotherm based on signal intensities of the benzyl vibrational mode

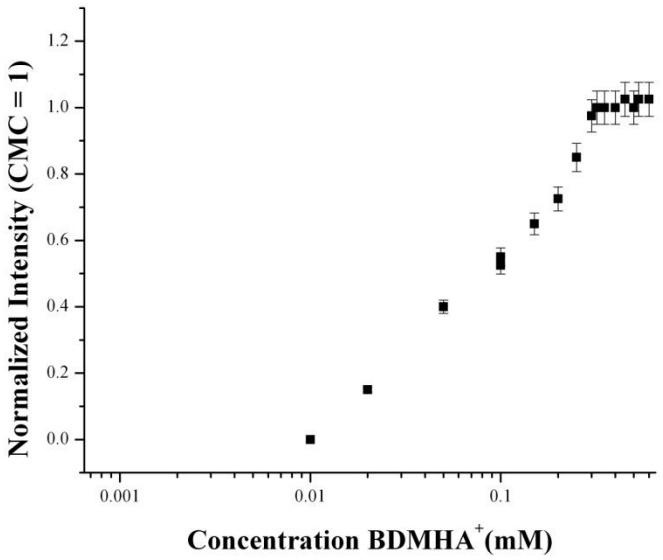

Fig. 6.14.2: Adsorption isotherm based on the normalized signal intensity of the benzyl stretch – CMC = 1 -log scale – point at 10 μM is shown as zero.

The adsorption isotherms at the OTS-coated silica, based on the benzyl stretch signal intensity vs. concentration, are compared to the adsorption isotherm of the pure surfactant at the bare silica (Figs and 6.14.3 (a) and (b)) over the concentration range from the detection limit of 1 μM up to 0.6 mM.

The surface excess of the pure surfactant at the hydrophobic silica surface is reduced by more than 50% with a fractional coverage of 0.46 relative to the surface coverage at the bare silica, assuming linear relationship between the molecules adsorbed at the surface and the Raman scattering intensity. The isotherms obtained at the hydrophilic vs. hydrophobic silica surfaces (Fig. 6.14.3) clearly demonstrate the lack of adsorption in the low concentration region at the hydrophobic silica surface, where electrostatic attraction

mechanisms are expected to be the dominating adsorption driving force, but are completely absent at the OTS-coated surface.

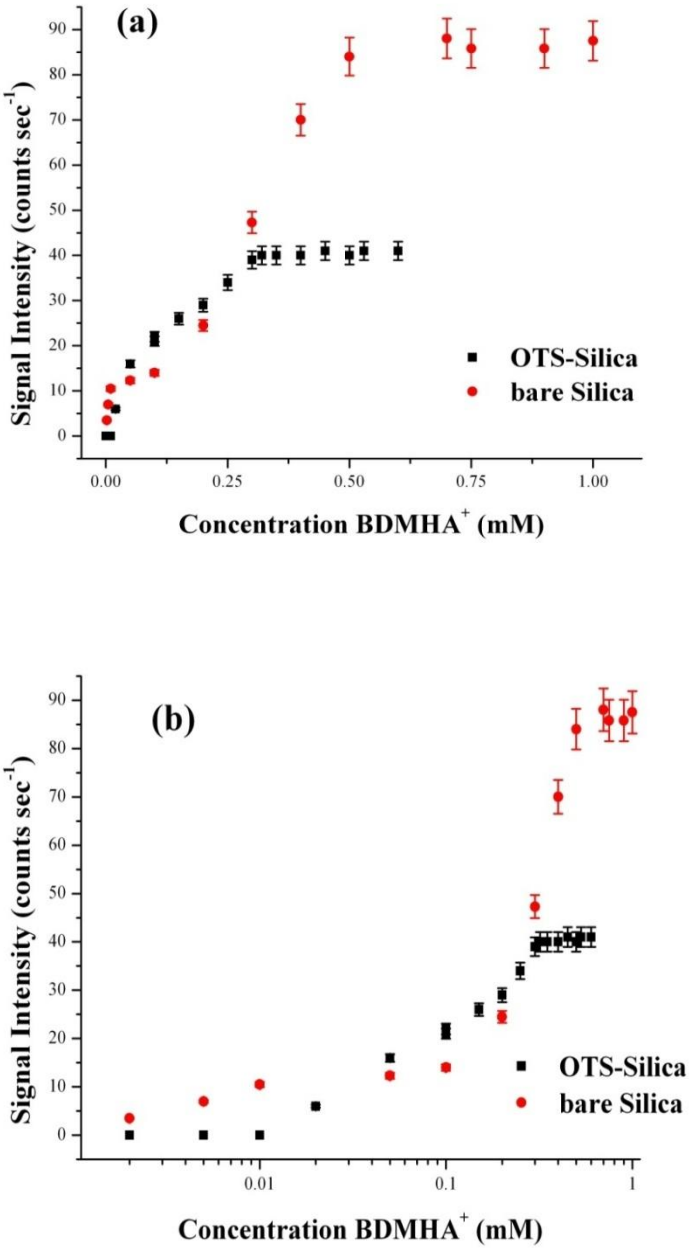

Fig. 6.14.3: Adsorption isotherm for $BDMHA^{+}$ at the bare silica (●) vs. the hydrophobic silica surface (■); (a) linear scale (b) log scale

The values shown in the isotherms in the concentration region between 1 and 10 μM in both graphs have values of zero; they are included intentionally to demonstrate that these concentrations were analyzed without any surface signal observed.

Adsorption via electrostatic mechanisms, expected between 1 and 10 or possibly 20 μM as observed for the pure surfactant at the bare silica surface, is absent at the OTS-coated silica-water interface, with adsorption dominated by the hydrophobic effect. It does not take place until 20 μM of initial surfactant concentration is reached. At the point of the critical surface aggregate concentration (csac),[101] surface coverage increases with a moderate slope of dΓ/dlog [C], proportional to increasing surfactant aggregate formation in solution; hemi-micelle formation is reached at the equilibrium plateau with maximum surface coverage at the apparent CMC of 0.32 mM. This value of 0.32 mM was obtained from curve fitting and taking the point of intersection of the fitted slopes before and beyond the apparent CMC or upper plateau region (Fig. 6.14.4.).

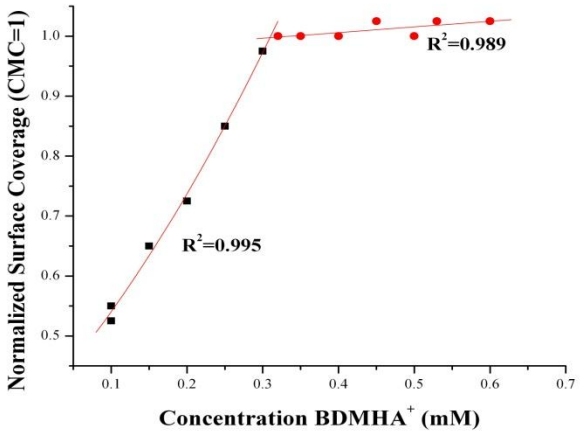

Fig. 6.14.4: Curve fitting of the $BDMHA^+$ adsorption isotherm – normalized to CMC=1

The moderate adsorption slope reveals two distinct adsorption regions where adsorption is driven by hydrophobic interaction of the non-polar long alkyl chains of the surfactant with the water molecules; the onset of adsorption occurs at a relatively high surfactant concentration with a moderately high adsorption slope of dΓ/dlog [C] between 20 and 50 μM, followed by a second adsorption region with a slightly lower and linear adsorption slope or coefficient, until the adsorption plateau is reached with completion of the hemi-micelle type structures.

The signal intensities and the shape of the isotherm relative to the pure surfactant at the bare silica suggest the formation of a hemi-micelle as the proposed structure at the OTS surface with the hydrophobic alkyl chain facing the equally hydrophobic alkyl portion of the OTS monolayer and the polar head groups shielding against the polar surrounding water molecules. This assumption is consistent with the reduced signal intensity of the surfactant at the OTS-coated surface with reduced coverage by 0.5 vs. the pure surfactant at the bare silica and is supported by previous studies related to the adsorption of cationic surfactants at hydrophobic surfaces. Adsorption isotherms with similar shapes, i.e., linearly increasing adsorption slopes, have been reported as characteristic for adsorption of cationic surfactants at uncharged or non-polar surfaces along with a hemi-spherical or hemi-cylindrical surfactant aggregate as the most likely structure.[170-172] An analytically supporting argument for reduced surface coverage, from spectral analysis, is the complete absence or presence at only trace levels of a benzyl combination band at 2780 cm^{-1}, that had previously been detected at the bare silica, at trace levels at concentrations < CMC, and with a visible amplitude in the adsorption

plateau region. In addition, formation of a spherical micelle would require contact of the polar head groups of the surfactant with a non-polar alkyl chain layer that does not appear feasible.

The isotherm of the pure surfactant normalized to the apparent CMC (maximum surface coverage) was fitted to a Langmuir adsorption model without the need to account for additional interaction between neighboring molecules. The lowest detectable concentration of 20 μM for the pure surfactant (based on the benzyl signal intensity) corresponds to a minimum detectable fractional surface coverage of 0.15, which is higher than the fractional coverage of 0.014 reported for the pure surfactant at the bare silica surface. These differences emphasize that detection limits are controlled both by instrumental sensitivity and the surface excess.

One significant difference in the adsorption behavior of $BDMHA^+$ as compared to CTAB and the related CTAC was the adsorption process, or slow adsorption kinetics;[55, 101] that were noticeable throughout the concentration range studied, but faster relative to the pure surfactant at the bare silica surface. The relatively slow adsorption process, with up to 30 to 60 minutes to reach steady state, depending on the surfactant concentration, reflects the slow kinetics of aggregate formation in solution, and is attributed to the bulky benzyl ligand at the surfactant head group. In comparison to the surfactant adsorption kinetics at the bare silica, kinetics are considerably faster, attributed to some extent to the increased hydrophobic nature of the system, including the surface, as discussed in more detail in section 6.15 and 6.16.

6.15. Effects of electrolyte addition on $BDMHA^+Cl^-$ adsorption

Addition of 5 mM divalent metal salt, in this experiment, magnesium chloride (as $MgCl_2 \cdot 6H_2O$) was sufficient to affect thermodynamic properties of the surfactant, i.e., free energy of micellization, the concentration corresponding to Γ_{max}, and adsorption kinetics in all three distinct adsorption regions, but with attenuated effects at very low surfactant concentrations, the adsorption slope region starting at the critical surface aggregate concentration, and in the upper adsorption plateau region for surfactant concentrations above the apparent CMC. This value shifted to 0.040 mM, with early onset of adsorption at 0.5 μM, but without any substantial increase of the adsorption slope $d\Gamma/d\log [C]$ in the hemi-micelle region (Figs 6.15.1. and 6.15.2.), as previously observed for the surfactant at the bare silica surface.

The characteristic adsorption features of the surfactant and its response to electrolyte addition are retained, but with attenuated adsorption behavior and loss of the typical sigmoidal shape in the adsorption isotherm, due to the missing electrostatic attraction mechanism between surfactant head group and surface charge. The lowest surface excess, observed at 0.5 μM in the low surfactant concentration region, corresponds to a fractional coverage of 0.075 relative to the pure surfactant. It originates from hydrophobic mechanisms, enhanced by the presence of the divalent metal salt. Maximum fractional surface coverage of 0.78 for the surfactant with 5 mM metal salt is based on the measured maximum signal intensity of 31 counts sec^{-1} at the maximum surface coverage, relative to the surface coverage of the pure surfactant with a scattering intensity of 40 counts sec^{-1}.

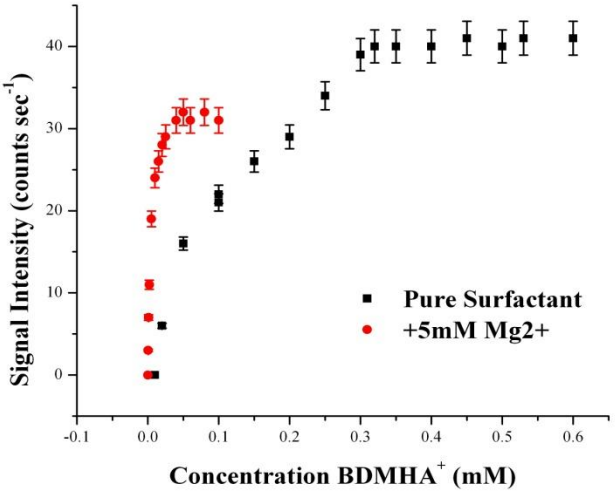

Fig. 6.15.1: Adsorption isotherm of pure surfactant and surfactant with 5 mM $MgCl_2$ at the hydrophobic silica-water interface: absolute signal intensities

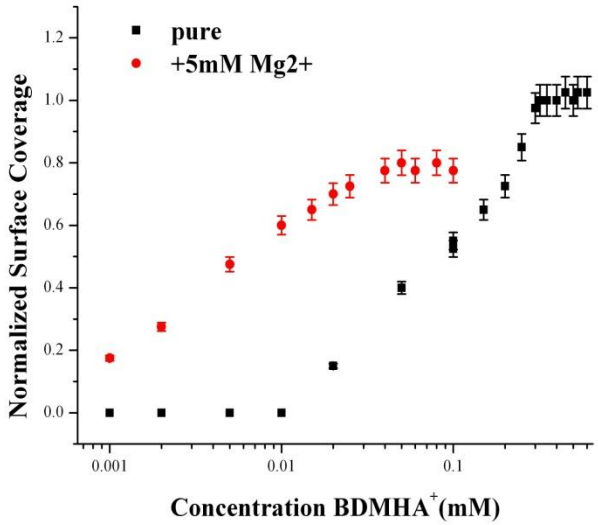

Fig. 6.15.2: Adsorption isotherm of pure surfactant and surfactant with 5 mM $MgCl_2$ at the hydrophobic silica-water interface: normalized signal intensities – log scale

This number has been determined with the assumption that the Raman signal intensity, again, is linearly related to the molecules adsorbed at the interface, and that the Raman scattering signal acquisition parameters remain constant. The adsorption trend, similar to the surface coverage decrease at the bare silica, might be explained by energetically more favorable surfactant aggregation in solution that affects both the number density and structure of the adsorbed surfactant. The prevailing adsorption mechanism arises from the so-called hydrophobic effect throughout the adsorption isotherm, with simultaneous enhancement of micellization in solution, due to the charge screening effects of the metal salt.

Addition of 10, 50, and 100 mM of $MgCl_2$ leads to further apparent CMC reduction of 0.030, 0.015, and 0.010 mM, respectively, as determined from the isotherm plots and curve fitting (Fig. 6.15.3. (a) and (b)); again, an increasing trend in the maximum surface coverage to 0.88, 0.9, and 0.95 relative to the normalized coverage of the pure surfactant at the hydrophobic surface is observed, for the surfactant containing 10, 50, and 100 mM of metal salt (Table 6.15.1.). Fractional coverage values are higher relative to the pure surfactant at the hydrophobic silica as compared to those found for the surfactant and electrolytes at the bare silica, as presented in section 6.6. The adsorption slope that represents the aggregate formation region is characterized by moderate increasing adsorption slopes of $d\Gamma/d \log [C]$, with increasing slope coefficients proportional to the electrolyte concentration.

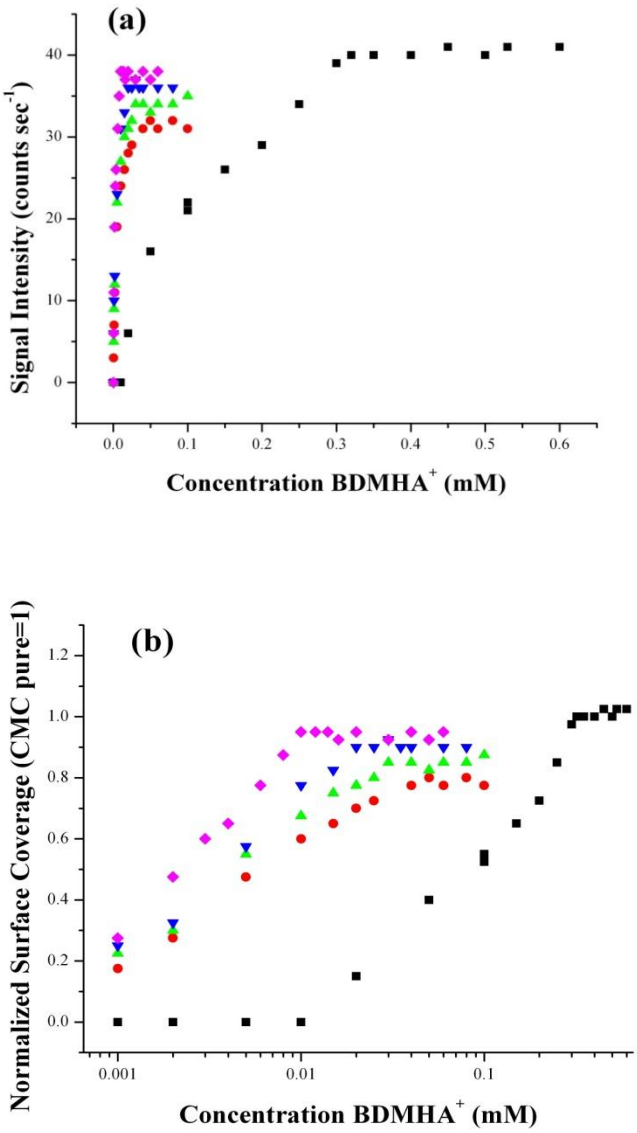

Fig. 6.15.3. : Adsorption isotherms of the pure surfactant (■); surfactant + 5mM (●); + 10mM (▲); + 50mM (▼); and + 100 mM (♦) $MgCl_2$ – error bars are omitted for clarity

(a) Benzyl intensity in counts sec^{-1} vs. concentration – linear scale
(b) Normalized signal intensity vs. concentration – log scale

Simultaneous reduction of the apparent CMC and increase in fractional surface coverage with increasing electrolyte concentrations suggest that hydrophobic effects from the electrolyte addition enhance both pathways that are available for lowering the energy of the complete system, micellization and adsorption. Increasing the ionic strength and thus the polarity of the solvent promotes both increasing aggregation numbers N_{agg} in solution and surface excess.

The apparent CMC or concentration corresponding to Γ_{max} vs. electrolyte concentration decreases again exponentially according to the classic relationship:

$$\text{Log CMC} = a - b \log [C] \qquad (6.15.1.)$$

The trends in adsorption and concentrations corresponding to the adsorption equilibrium at the bare silica vs. hydrophobic silica surface imply that surface properties, i.e., the maximum attainable surface coverage, influence the apparent CMC, as much as other thermodynamic and kinetic properties.

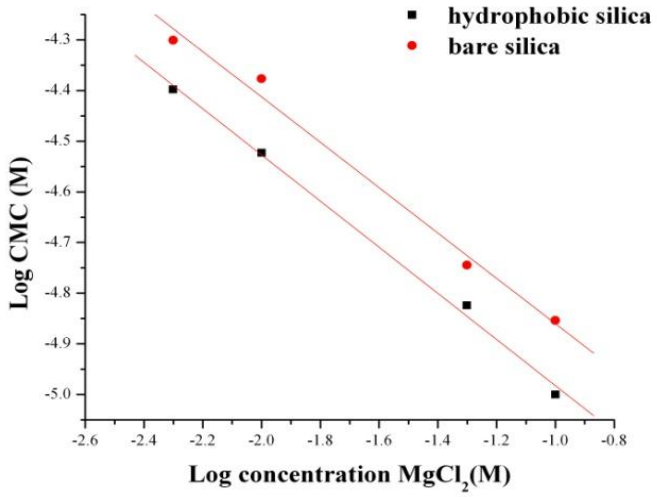

Fig. 6.15.4.: Apparent CMC vs. electrolyte at the bare vs. hydrophobic silica surface

The slope for the surfactant at the bare silica surface had been determined as -0.45 in the 1st part of the study; the fitted data show an identical slope of -0.45 for the surfactant at the hydrophobic silica, but with an overall lower CMC as given by the lower intercept of Δ -0.13 (Fig. 6.15.4.).

The downward shift of the log apparent CMC - log [C] correlation with retention of the slope gives rise to questions whether bulk depletion from transfer of surfactant molecules to the surface gives biased results that are related to the small sampling cell and small volume to surface area ratio of 1.23 cm^3/1.00 cm^2. A calculation based on full monolayer coverage, and a molecular number density of $1*10^{15}$ cm^{-2} relative to $6.7*10^{17}$ molecules present in the cell (at 0.5 mM surfactant concentration) shows that a fraction of 0.0027 molecules could be transferred from bulk to the surface; these aspects of volume/surface area ratio have to be considered when describing the thermodynamics of the system, i.e., CMC and change in Gibbs free energy of adsorption; it appears that these numbers are still too small to explain the downward apparent CMC shift, and should not affect the change in free energy within the framework of this experiment. These shifts in CMC values in the presence of a hydrophobic surface, strongly indicate that within a given volume/surface area regime, the observed, apparent CMC's are not only controlled by the solution properties, but surface effects, i.e., surface charge, and attainable surface coverage, need to be accounted for. The reduced surface coverage, 50% of the value observed at the negatively charged surface, leads to the following statement: the nature of the surface does not allow exceeding the maximum coverage controlled by the hemi-micellar structure; this limitation of energy lowering via the adsorptive pathway enhances

the alternative mechanism for reduction of the free energy of the system via micellization, indicated by the apparent CMC lowering properties. This assumption is valid for both the pure surfactant, as shown in the CMC lowering of pure surfactant at the hydrophobic vs. the hydrophilic silica surface, and also for the surfactant in the presence of electrolyte. It also implies that the true CMC values need to be determined by more suitable techniques, i.e., conductivity or surface tension measurements that measure solution properties, since the breakpoint observed in the adsorption isotherms may not coincide with the true CMC.

6.16. Adsorption isotherm models and parameters

The isotherm shapes do not show the characteristic features of sigmoidal growth adsorption isotherms in the lower portion that normally represents the 1st plateau originating from electrostatic adsorption mechanisms and is missing in all isotherms; however, adsorption isotherms for the surfactant with electrolyte addition show moderate sigmoidal growth behavior on the adsorption slope, in accordance to the modified Langmuir model, making it still an appropriate model for describing the overall adsorption process.

$$\ln\left(\frac{\theta}{1-\theta}\right) - g\theta = \ln K_{mod} + \ln[C] \qquad (6.16.1)$$

Using the linearized expression in eq (6.16.1) with the natural logarithm on both sides, the interaction energy parameter $g\theta$ was determined by adjusting its value to converge to

the best linear fit correlation. The modified equation gave the equilibrium constant K_{mod} from the intercept of the linearized logarithmic correlation after referencing it to the molarity of water (Table 6.16.1).

The fitted isotherms and computed adsorption constant for the pure surfactant showed a change in Gibbs free energy of adsorption of -17 (±1) kJ mol^{-1}. The adsorption constant determined from the fitted data for the pure surfactant does not include any interaction energy parameter, since no deviation from a typical Langmuir adsorption model was identified. The interaction energy parameter for the surfactant with small addition of the magnesium salt shows a small value of 0.5, whereas higher metal salt additions of 10, 50 and 100 mM gave an interaction energy parameter of 1, 3, and 2.5; The moderately increasing interaction energy arises from the higher aggregation numbers and denser packing of the surfactant in solution and at the surface, with favorable lateral interaction between the neighboring molecules.[134]

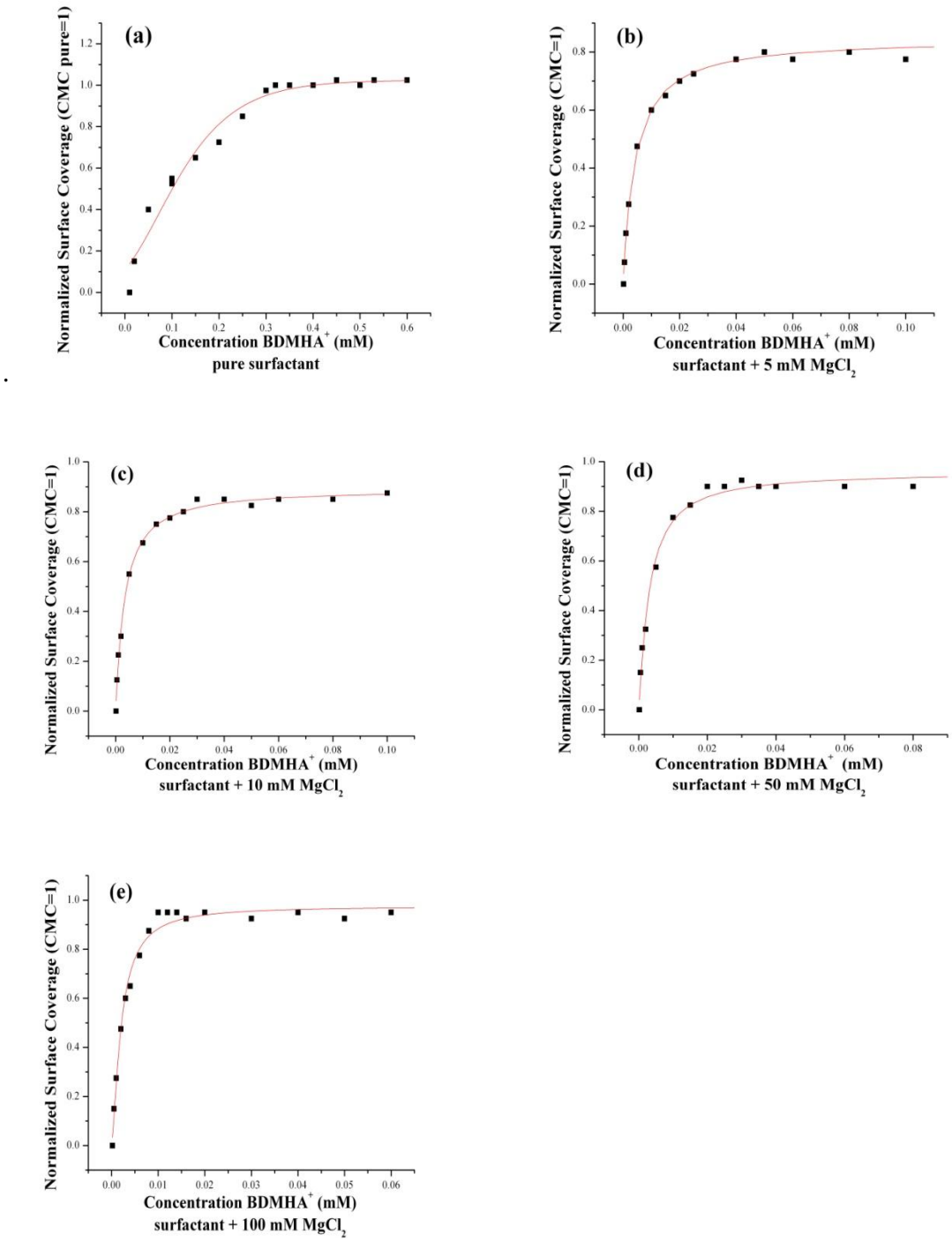

Fig. 6.16.1.: Adsorption isotherms fitted to a Langmuir or modified Langmuir adsorption model

The change in Gibbs free energy of adsorption was determined as -17 (±1) kJ mol^{-1}, for the pure surfactant, decreased only to -18 (±1) kJ mol^{-1} for the surfactant + 5 mM magnesium salt, to -20 (±2) kJ mol^{-1} for surfactant + 10 mM of metal salt additive (Table 2), and to -33 (±14) kJ mol^{-1} for the surfactant with 50 mM of metal salt, reaching its minimum with a metal salt addition of 100 mM that showed the most favorable change in free energy of adsorption of -34 (±3) kJ mol^{-1} (Table 6.16.1.).

Table 6.16.1: Adsorption energy parameters from adsorption isotherm fitting

Surfactant System	$\Delta\Delta G_{ads}$ (kJ/mol)	K_{mod}	K_{mod} R^2	g	K_L	CMC (μM)	Γ_{max} CMC = 1
Pure Surfactant	-17 ± 1	$9.4*10^4$ $\pm 7.2*10^3$	0.994	N.A.	K_{ads}	320 ± 10	1.00
Surfactant + 5 mM $MgCl_2$	-18 ± 1	$1.4*10^5$ $\pm 5*10^3$	0.994	0.5	$K_{mod}\, e^{-0.5\theta}$	40 ± 3	0.78
Surfactant + 10mM $MgCl_2$	-20 ± 2	$4.4*10^5$ $\pm 3.2*10^4$	0.992	1.0	$K_{mod}\, e^{-1.0\theta}$	30 ± 2	0.80
Surfactant + 50 mM $MgCl_2$	-33 ± 14	$6.7*10^7$ $\pm 2*10^7$	0.994	3.0	$K_{mod}\, e^{-3.00\theta}$	15 ± 2	0.90
Surfactant + 100mM $MgCl_2$	-34 ± 3	$1.0*10^8$ $\pm 10*10^6$	0.998	2.5	$K_{mod}\, e^{-2.5\theta}$	10 ± .4	0.95

The overall change in Gibbs free energy of adsorption for the pure surfactant is only slightly lower than the one determined for the equivalent system at the bare silica surface, as reflected in the adsorption constant. This can be rationalized by the fact that in both

processes the hydrophobic mechanism is the primary force across the major portion of the adsorption slope. Addition of the electrolyte leads to moderate increase of adsorption constant; increasing the polarity of the solvent does not enhance the hydrophobic effect as previously observed at the bare silica; this surfactant reverts to the alternative mechanism of micellization with decrease in ΔG_{mic} when correlated to the decreasing apparent CMC. This parameter gradually shifts to lower surfactant concentrations proportional to the concentrations of the divalent metal salt and is consistently lower than the apparent CMC values determined for the surfactant at the bare silica (Fig. 6.15.4). The fractional surface coverage given in Table 6.16.1 is related to the pure surfactant at the hydrophobic surface. Relative to the surface coverage at the bare silica, the fractional coverage is actually 0.46, 0.35, 0.37, 0.41, and 0.44 for the pure surfactant, and the surfactant with 5, 10, 50, and 100 mM of electrolyte, respectively.

The adsorption isotherm shape compares well with isotherms reported in literature for cationic surfactant adsorption at hydrophobic surfaces where the electrostatic attraction is missing. These systems are characterized by lack of the lower adsorption plateau at very low concentrations, with a relatively steep slope already seen at the onset of adsorption, followed by a moderate linear slope, until the equilibrium plateau with maximum surface coverage is reached.

The correlation between thermodynamic and kinetic parameters and surface properties is illustrated below by a graphic representation of the trends related to (a) change in free energy of adsorption, (b) fractional surface coverage, with surface

coverage at the apparent CMC of the pure surfactant at the hydrophilic silica surface used as reference value, and (c) adsorption constant K_{mod}, as function of surface properties, and electrolyte addition. The free energy of adsorption at the bare silica increases almost exponentially with increasing electrolyte addition up to electrolyte concentrations of 50 mM, followed by a trend reversal.

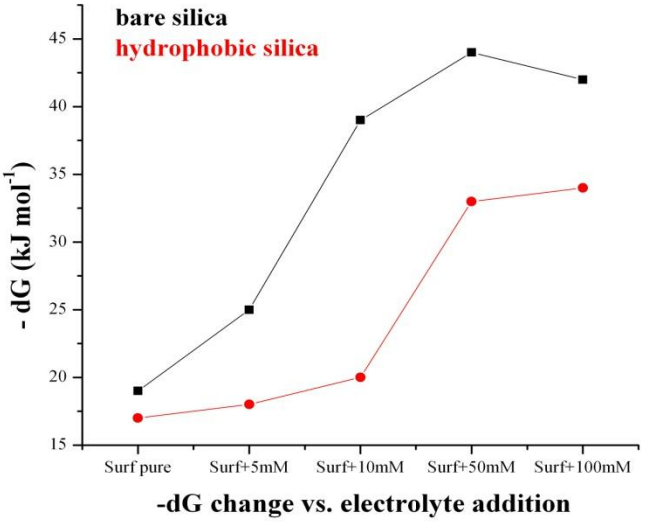

Fig. 6.16.2.: Change in Gibbs free energy of adsorption as function of surface and **e**lectrolyte addition

In contrast, the change in free energy of adsorption at the hydrophobic silica surface is moderate at low electrolyte concentrations, increases abruptly at 50 mM of electrolyte addition, but without any significant increase when doubling the electrolyte concentration to 100 mM. These trends, as emphasized previously in connection with the adsorption kinetics, imply that moderate electrolyte addition of 50 mM leads to optimum enhancement of thermodynamic and kinetic surfactant properties. Coverage on the bare

silica and hydrophobic silica surface follow similar trends: after initially reduced adsorption by about 50% upon addition of electrolyte to the solution, surface coverage increases at a high rate at the hydrophilic surface, and with moderate increase at the hydrophobic silica surface, but in each case, proportional to electrolyte concentrations.

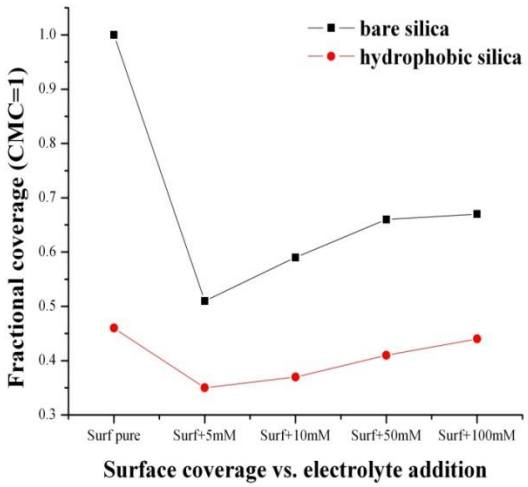

Fig. 6.16.3: Fractional surface coverage as function of surface properties and electrolyte

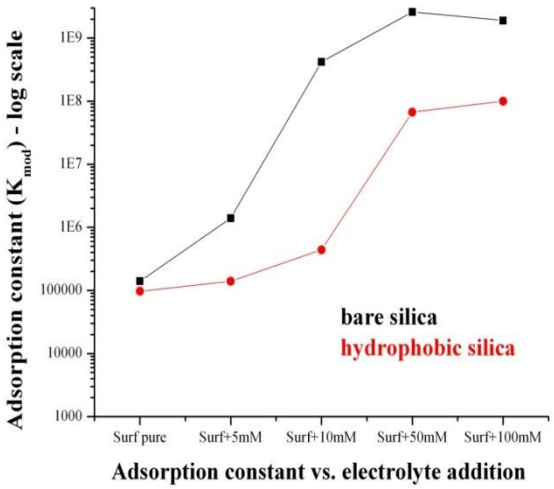

Fig. 6.16.4: Adsorption constant as function of surface properties and electrolyte

Adsorption trends at the hydrophobic surface show a similar pattern, but with attenuated effects. It is evident that the electrolyte addition, despite its charge screening effects, enhances the hydrophobic adsorption mechanism on both surfaces with increasing electrolyte concentration; the surface coverage at the hydrophobic surface is, however, only 50% of the initial coverage at the hydrophilic silica, and adsorption enhancement occurs at lower rates, emphasizing the competitive nature of the two energy lowering pathways, as confirmed by the trends in the equilibrium adsorption constants (Table 6.7.1. and Fig. 6.16.3.)

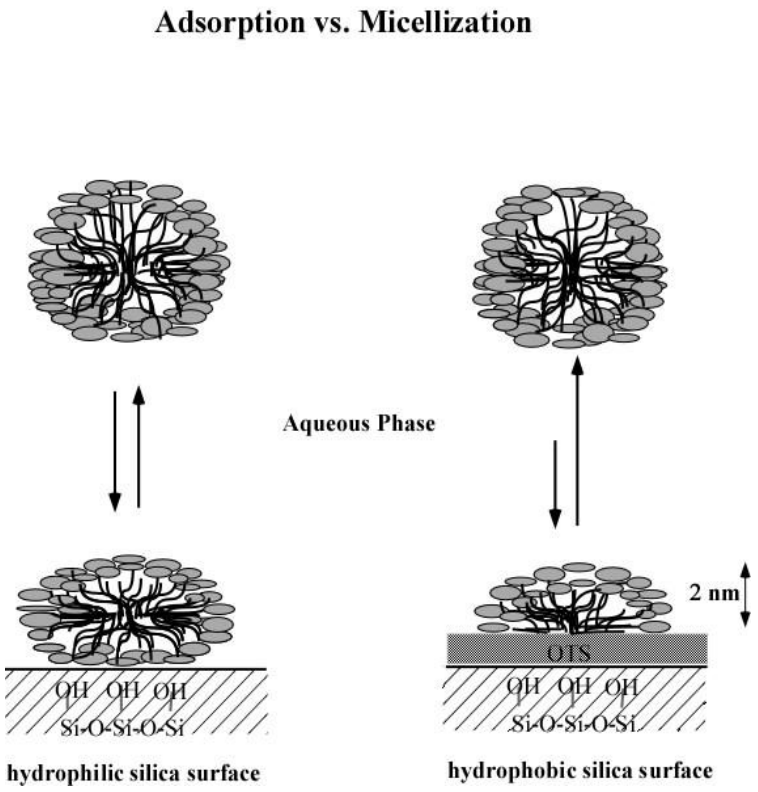

Fig. 6.16.5: Two competing processes in the surfactant-silica-solution system

Electrolytes enhance the micellization mechanism as the primary energy lowering mechanism, in particular at lower electrolyte concentrations. As electrolyte concentrations increase, both micellization and adsorption are positively influenced by the hydrophobic effect that is stronger for the bare silica relative to the hydrophobic surface (Fig. 6.16.5).

6.17. Orientational analysis of surfactant with electrolyte addition

P-polarized sampling geometry was used in separate experiments for the analysis of selected surfactant concentrations between 0.005 and of 0.040 mM to identify possible orientational or structural changes according to the criteria that were described in detail in sections 2.4, 6.4, and 6.8. for the respective scattering modes.[54, 55] The set from p-polarized spectra (P_{x+y}) and their s-polarized (S_y) counterparts, that are presented in this section, include the surfactant with 10 mM of metal salt addition at three relevant concentrations, 0.005 mM at the onset of adsorption, 0.015 mM at the adsorption slope, and 0.040 mM of surfactant above the apparent CMC. A spectral overlay (Figs. 6.17.1. and 6.17.2.) of both s- and p-polarized spectra serves as a representative set for demonstrating the intensity ratios of the symmetric vs. anti-symmetric stretching modes and their potential use for identifying orientational or structural changes of the surfactant molecules as function of increasing concentrations.

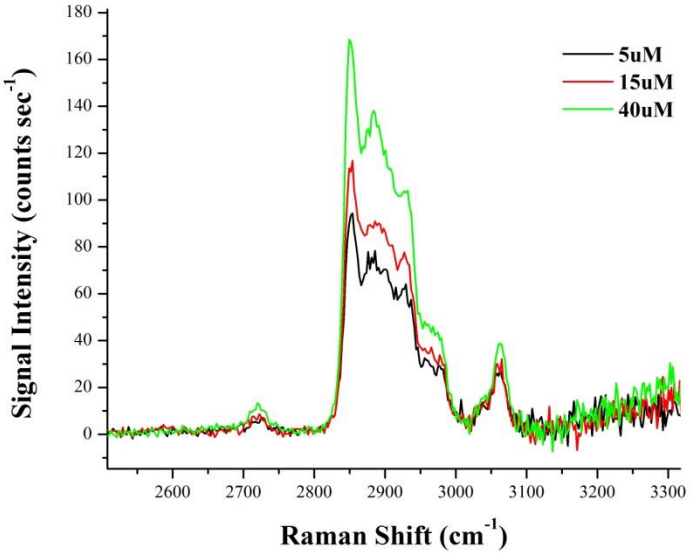

Fig. 6.17.1: Spectral overlay of surfactant + 10 mM $MgCl_2$ (s-polarization)

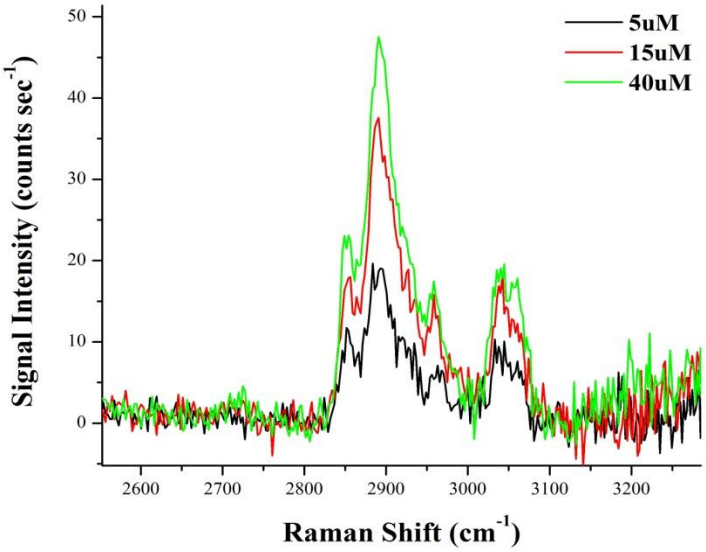

Fig. 6.17.2: Spectral overlay of surfactant+ 10 mM $MgCl_2$ (p-polarization)

The ratios of the corresponding signals obtained for the methylene symmetric and anti-symmetric modes showed small changes in signal intensity ratios (Figs 6.17.1. and 6.17.2.) with a generally increasing trend of the anti-symmetric stretching vs. the symmetric stretching modes when going from the lowest surfactant concentration of 0.005 mM to 0.040 mM (Table 3), with exception of the intensity ratios observed within the s-polarized spectra, that do not confirm this trend[154, 155] (Table 6.17.1.).

The signal intensity ratios of the anti-symmetric vs. symmetric methylene stretching modes, observed in p-polarized sampling geometry, increase from 1.7 to 2.04, from 0.12 to 0.15 for the symmetric methylene stretching modes, and from 0.21 to 0.40 for the antisymmetric methyl stretch, from p- vs. s-polarized spectra, that suggest a slight transition to more ordered structural arrangement of the surfactant at the surface, despite the high margin of error, in particular in the latter data set.[156, 157] This assessment is in agreement with the assumptions made in the first part of the experiment relative the surfactant at the bare silica, that might form micellar type aggregates at the silica surface.[92, 112, 173,55] In contrast, the signal intensity ratios in this section may suggest a more organized hemi-micellar structure at the hydrophobic surface.

Table 6.17.1: Signal intensity ratios from s- and p-polarized spectral analysis:

Surfactant Concentration	0.005	0.015	0.040 mM
Sy/Sy Ratio			
$CH_3\ \nu_{as}/CH_2\ \nu_s$	0.33±0.03	0.33±0.03	0.28±0.03
Pxy/Pxy Ratio			
$CH_3\ \nu_{as}/CH_2\ \nu_s$	0.56±0.31	0.88±0.24	0.77±0.17
$CH_2\ \nu_{as}/CH_2\ \nu_s$	1.68±0.54	2.13±0.4	2.04±0.28
Pxy/Sy Ratio			
$CH_3\ \nu_{as}/CH_3\ \nu_{as}$	0.21±0.05	0.40±0.07	0.37±0.06
$CH_2\nu_{as}\ /\ CH_2\ \nu_{as}$	0.25±0.03	0.41±0.03	0.34±0.01
$CH_2\nu_s\ /\ CH_2\ \nu_s$	0.12±0.02	0.15±0.02	0.13±0.02

Since the signal intensities are directly proportional to concentrations, only ratios and their trends are considered in this analysis. The shifts in frequency or peak positions observed with the prominent vibrational modes as the surfactant concentrations are increased, although small compared to the frequency shifts reported in previous studies, confirm the above assumptions (Table 4).[155, 157]

Table 6.17.2: Frequency shift observed in the concentration range of 0.005 to 0.040 mM

max Δ cm^{-1}	P_{xy}	S_y
CH_2 ν_s	-2.0	-3.0
CH_2 ν_{as}	-2.0	-5.0
CH_3 ν_{as}	-6.0	-5.0

6.18. Effects of magnesium chloride on the interfacial water structure

The Raman spectral baseline that usually exhibits a straight line with the water background signal corrected, showed a positive offset of the water band in the frequency region of 3300 - 3400 cm^{-1}, that increased reproducibly and proportional to the magnesium chloride concentrations in the spectra taken from the samples that contained both surfactant and metal salt, but was independent of the surfactant concentration (Fig. 6.18.1). A similar offset water signal was observed in the previous study of surfactant adsorption at the bare silica surface with a detailed discussion regarding its origin. The contribution from the symmetric ice-like water vibrational modes to the signal offset was negligible at the bare silica-water interface, but cannot be ignored in the analysis of the spectra from the OTS-coated silica surface, due to its interference with the benzyl stretching modes at high electrolyte concentrations (Fig. 6.18.1 (a)).

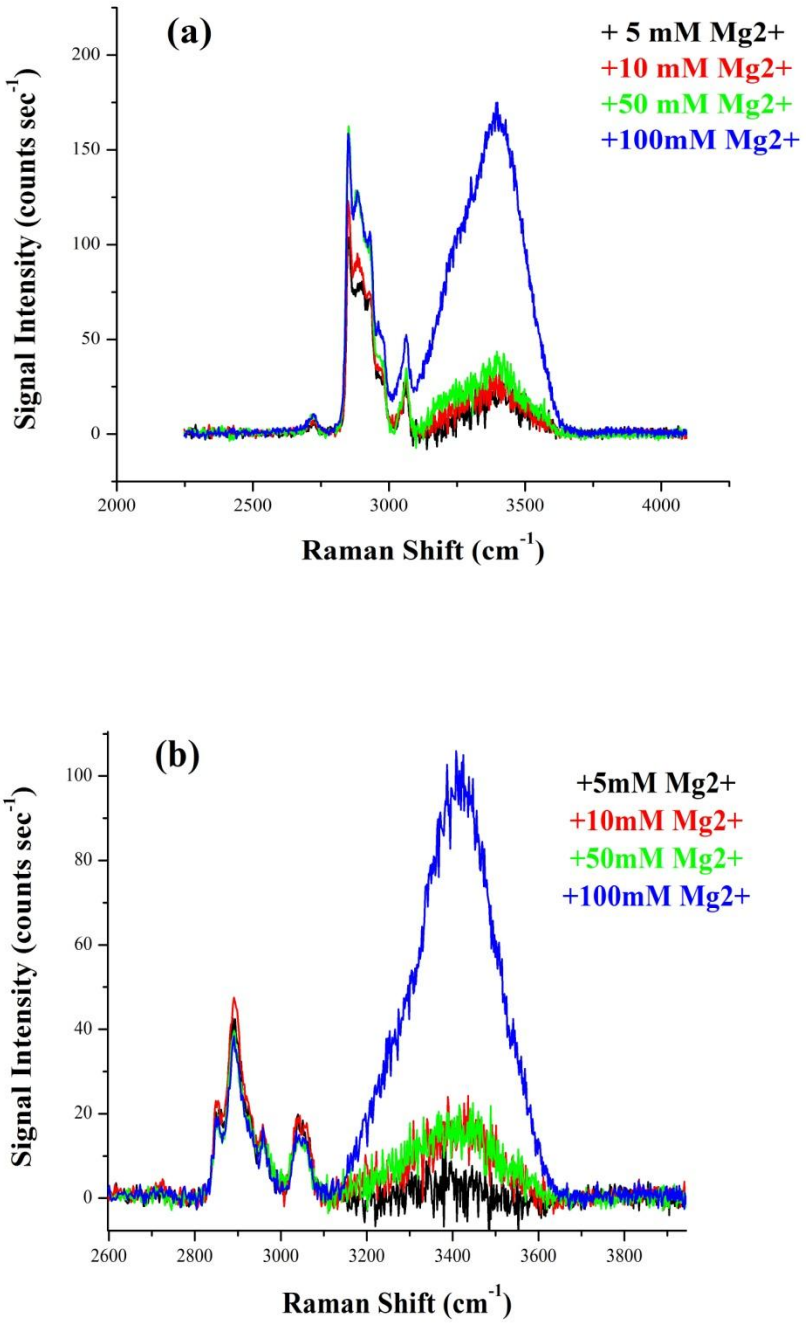

Fig. 6.18.1. : Offset water signal as function of magnesium ion concentration (a) s-polarized and (b) p-polarized sampling geometry

The spectral overlay (Fig. 6.18.1.(a)) presents selected spectra with background correction applied only to the surfactant with 50 mM of metal salt in s-polarized sampling geometry to emphasize the increased signal offset, and its effect on the spectral baseline and interference with the benzyl vibrational modes, especially for the surfactant with addition of 100 mM of magnesium chloride. The background signals in all other experimental work involving adsorption isotherm of the surfactant with 50 and 100 mM metal salt addition were corrected for this offset in s-polarized sampling geometry. The background was taken from aqueous solutions in the sample cell that contain electrolyte comparable to amounts of the sample to be studied. Signal correction was not required for p-polarized sampling geometry since the more symmetric modes of the ice-like water structure show less susceptibility towards p-polarized incident light.

6.19. Effects of head group properties on surfactant behavior

An imidazolium-based surfactant-like ionic liquid containing a hydrophobic alkyl tail of sixteen carbons, identical to the hydrophobic portion of $BDMHA^+$, served as a model compound to (a) identify the adsorption isotherm of these types of cationic compounds and (b) compare their adsorption behavior as function of varying head group properties. Both compounds (Fig. 6.19.1) contain identical hydrophobic C_{16} alkyl chains as well as identical halide counterions; the major differences in thermodynamic and kinetic properties arise from the head group properties and their differences in aqueous solubility and geometric factors. The isotherm established for $[C_{16}MIM][Cl]$ was taken at lower laser power setting of 0.5 W and longer acquisition times of 10 minutes. A conversion

factor was applied to the raw experimental data to adjust for the difference in acquisition parameters before establishing its final adsorption isotherm. Both cationic compounds demonstrate unique surfactant-solvent interaction and adsorption characteristics that are solely a function of the head group properties.

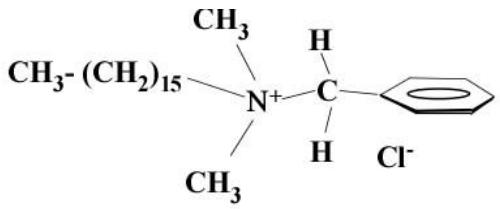

Benzyldimethylhexadecylammonium chloride

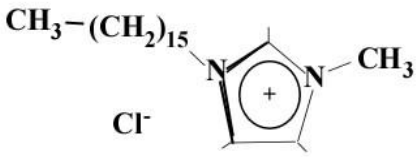

1-n-Hexadecyl-3-Methyl Imidazolium chloride

Fig. 6.19.1: Molecular structure of benzyldimethylhexadecylammonium chloride ($BDMHA^+Cl^-$) and $[C_{16}MIM][Cl]$

The surfactant-like ionic liquid showed higher water solubility[174] consistent with the lower Krafft point at room temperature, as compared to $BDMHA^+Cl^-$ that required additional heat input to approx. 35˚C to solubilize in the aqueous phase.

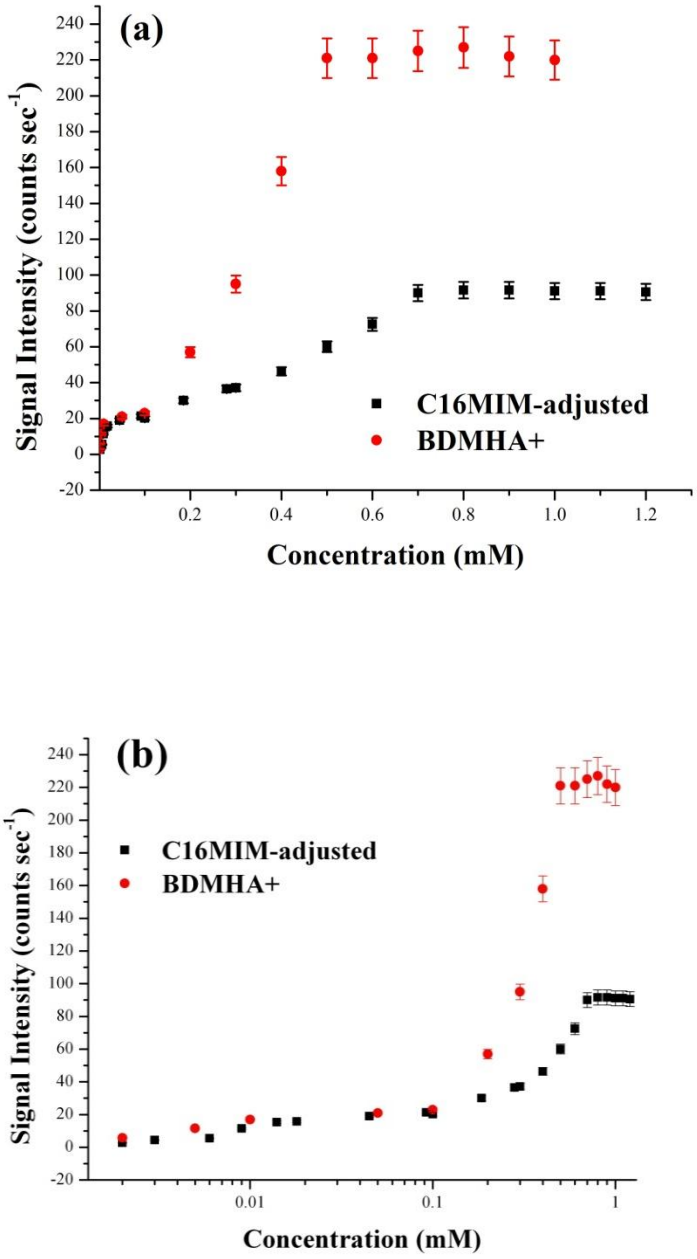

Fig. 6.19.1.: Adsorption isotherms for $[C_{16}MIM][Cl]$ and $BDMHA^{+}Cl^{-}$ at the silica-water interface: (a) linear and (b) log scale

These differences in aqueous solubility arise from the different physico-chemical properties of the head group function, since the hydrophobic alkyl tail and the counter ions are identical in both compounds. It manifests itself in decreased adsorption trends seen in the adsorption isotherms (Fig. 6.19.1.) where the more water soluble [C_{16}MIM][Cl] favors micellization in solution vs. adsorption to the substrate. Fig. 6.19.1. (b) reveals that electrostatic adsorption mechanisms are identical for both compounds in terms of surface coverage in the low concentration region spanning the range from 1 uM to possibly 0.100 mM, followed by increased adsorption due to hydrophobic effects of $BDMHA^+$ relative to the surfactant-like ionic liquid and a surface coverage twice the value of [C_{16}MIM][Cl]. The CMC of [C_{16}MIM][Cl] was determined as 0.7 mM along with a lower adsorption slope showing its different thermodynamic properties that favors aggregate formation in solution for lowering the free energy of micellization over the free energy of adsorption, but to lower extent relative to the aggregation behavior of the more hydrophobic $BDMHA^+$. This assumption is valid within the context of identical silica surface properties. $BDMHA^+$ reverts to micellization as the more advantageous energy lowering mechanism at hydrophobic surfaces, with an increased tendency towards micellization as confirmed by its lower apparent CMC.

The surfactant-like ionic liquid exhibited faster adsorption kinetics with generally 20 to 30 minutes required to reach equilibrium, irrespective the concentration, which is in contrast to the pure $BDMHA^+$ that required several hours before equilibrium was reached at concentrations close to and above the CMC.

Chapter 7: Discussion and Conclusion

7.1. Study of surfactants at the bare silica-water interface

The study presents a detailed description of adsorption behavior of the surfactant $BDMHA^{+}Cl^{-}$ by taking advantage of long acquisition times and strong incident excitation power to enhance the signal strength and study the slow adsorption kinetics and adsorption isotherm of the pure surfactant at the silica-water interface; this system provides a set of reference values in contrast to its modified adsorption behavior induced by metal salt addition. The results are consistent with previous findings that conformational order or restructuring of the surfactant molecules in the hemi-micelle and monolayer forming region is not significant for this surfactant; the most likely structure is a spherical or elongated globular aggregate with optimum packing of the monomers for minimization of the free energy of adsorption. Additional and complementary techniques, i.e., light scattering techniques, that directly probe the process in solution, might be helpful to support the results from this study, and get information on the surfactant aggregation in solution.

The overall results confirm that surfactant adsorption behavior can be modulated by controlling interfacial properties. In the presence of metal salt, the structure may evolve into a more organized arrangement at the silica-water surface due to more efficient screening of head group charges and increased hydrophobic effects that are offset by opposing mechanisms when increasing the salt content above 50 mM. The fractional surface coverage does not explicitly indicate the exact number density of the surfactant

aggregates at the interface; its maximum surface coverage may be lower than found for cationic surfactant with smaller and more symmetric head group functions. However, the adsorption constants as function of electrolyte concentration indicate favorable adsorption mechanisms in the presence of low electrolyte concentrations, despite the competitive alternative mechanism of micellization.

7.2. Surfactant at the hydrophobic silica-water interface

Consistent with previous findings, adsorption is feasible at the hydrophobic silica surface, since no repulsive forces are involved, but both thermodynamic and kinetic parameters show changes in the three critical surfactant concentration regions. At low surfactant concentrations, adsorption can be initiated by electrolyte addition, even at surfactant concentrations below 1 μM..

The surface properties affect practically all thermodynamic and kinetic parameters; they influence the aggregation in solution as much as they modulate the adsorption behavior. Correlation of the two systems involving surfactant - solution – electrolyte – surface properties emphasizes that several competing and co-existing mechanisms affect the interaction of the various components in this system. Surface properties, such as hydrophilic vs. hydrophobic silica surfaces, affect the surface coverage, and thus may influence, thermodynamic parameters, i.e., CMC, that are normally considered a function of solution components only.

7.4. Summary

Raman spectroscopy in TIR geometry proves a viable tool for studying molecular adsorption mechanisms at interfacial regions, if both phases have dielectric properties with realistic refractive index ratios. The sampling geometry dictates surface and spectroscopy related selection rules for Raman signal scattering; these selection rules can be somewhat limiting, but also used as a tool to interpret signal intensities within the framework of the sampling geometry and detection system.

Draw-backs in TIR applications arise from the constraints found with the individual dielectric substrates used as the TIR element. The use of silica surfaces, i.e., limits the spectral range to the high frequency region, since the low frequency range contains too much interfering signals from Si-OH and Si-H vibrational modes besides the background signal contributions from the transmitted medium itself. A comprehensive understanding of the research goals, identification of the most appropriate substrate, is desirable, when designing a TIR experimental instrument. It provides a useful tool to study molecule-substrate interactions, obtain new information on a molecular level and simultaneously gather data related to thermodynamic and kinetic properties.

Bibliography

1. Butt, H. J.; Graf, K.; Kappl, M., Physics and Chemistry of Interfaces. *Wiley Publishing, Weinheim* **2011,** 2nd Ed., (4th reprint), 1-3.
2. Atkin, R.; Craig, V. S. J.; Wanless, E. J.; Biggs, S., The Influence of Chain Length and Electrolyte on the Adsorption Kinetics of Cationic Surfactants at the Silica–Aqueous Solution Interface. *J. Colloid Interface Sci.* **2003,** 266, 236-244.
3. Fainerman, V. B.; Miller, R.; Moehwald, H., General Relationships of the Adsorption Behavior of Surfactants at the Water/Air Interface. *J. Phys. Chem. B* **2002,** 106, 809-819.
4. Fuerstenau, D. W., The Adsorption of Surfactants at Solid-Water Interfaces. *The chemistry of Biosurfaces, Vol.1* **1971**, 143-176.
5. Somasundaran, P.; Zhang, L., Adsorption of Surfactants on Minerals for Wettability Control in Improved Oil Recovery Processes. *J. Petroleum Sci Eng* **2006,** 52, 198-212.
6. Wei, X.; Hong, S.-C.; Lvovsky, A. I.; Held, H.; Shen, Y. R., Evaluation of Surface vs Bulk Contributions in Sum-Frequency Vibrational Spectroscopy Using Reflection and Transmission Geometries. *J. Phys. Chem. B,* **2000,** 14, (14), 3349-3354.
7. Haumann, M.; Jakuttis, M.; Wasserscheid, S. W. P., Supported Ionic Liquid Phase (SILP) Catalyzed Hydroformylation of 1-Butene in a Gradient-Free Loop Reactor. *J of Catalysis* **2009,** 263, 321-327.
8. Haumann, M.; Riisager, A., Hydroformylation in Room Temperature Ionic Liquids (RTILs): Catalyst and Process Developments. *Chem. Rev.* **2008,** 108, 1474-1497.
9. Kolbeck, C.; Killian, M.; Maier, F.; Paape, N.; Wasserscheid, P.; Steinrueck, H.-P., Surface Characterization of Functionalized Imidazolium-Based Ionic Liquids. *Langmuir 2008* **2008,** 24, 9500-9507.
10. Riisager, A.; Wasserscheid, P.; Hal, R. v.; Fehrmann, R., Continuous Fixed-Bed Gas-Phase Hydroformylation Using Supported Ionic Liquid-Phase (SILP) Rh Catalysts. *J of Catalysis* **2003,** 219, 452-455.
11. Sobota, M.; Nikiforidis, I.; Hieringer, W.; Paape, N.; Happel, M.; Steinruck, H.-P.; Goerling, A.; Wasserscheid, P.; Laurin, M.; Libuda, J., Toward Ionic-Liquid-Based Model Catalysis: Growth, Orientation, Conformation, and Interaction Mechanism of the [Tf2N]- Anion in [BMIM][Tf2N] Thin Films on a Well-Ordered Alumina Surface. *Langmuir* **2010,** 26, (10), 7199-7207.
12. Zhao, Y.; Li, M.; Lu, Q., Tunable Wettability of Polyimide Films Based on Electrostatic Self-Assembly of Ionic Liquids. *Langmuir* **2008,** 24, 3937-3943.
13. Holland, J. G.; Jordan, D. S.; Geiger, F. M., Divalent Metal Cation Speciation and Binding to Surface-Bound Oligonucleotide Single Strands Studied by Second Harmonic Generation. *J. Phys. Chem. B 2011, 115, 8338–8345* **2011,** 115, 8338-8345.
14. Chen, E. H.; Hayes, P. L.; Nguyen, S. T.; Geiger, F. M., Zinc Interactions with Glucosamine-Functionalized Fused Silica/Water Interfaces. *J. Phys. Chem. C* **2010,** 114, 19483-19488.
15. Zhang, X. L.; Penfold, J.; Thomas, R. K.; Tucker, I. M.; Petkov, J. T.; Bent, J.; Cox, A., Adsorption Behavior of Hydrophobin and Hydrophobin/Surfactant Mixtures at the Solid Solution Interface. *Langmuir* **2011,** 27, 10464-10474.
16. Orendorff, C. J.; Pemberton, J. E., Alkylsilane-Based Stationary Phases via a Displaceable Surface Template Approach: Synthesis, Characterization, and Chromatographic Performance. *Anal. Chem.* **2005,** 77, 6069-6077.

17. Gordon E. Brown, J.; Henrich, V. E.; Casey, W. H.; Clark, D. L.; Eggleston, C.; Felmy, A.; Goodman, D. W.; Gra¨tzel, M.; Maciel, G.; McCarthy, M. I.; Nealson, K. H.; Sverjensky, D. A.; Toney, M. F.; Zachara, J. M., Metal Oxide Surfaces and Their Interactions with Aqueous Solutions and Microbial Organisms. *Chem. Rev.* **1999,** 99, 77-174.
18. Ying, G.-G., Fate, Behavior and Effects of Surfactants and Their Degradation Products in the Environment. *Environment International* **2006,** 32, 417-431.
19. Kweskin, S. J.; Rioux, R. M.; Habas, S. E.; Komvopoulos, K.; Yang, P.; Somorjai, G. A., Carbon Monoxide Adsorption and Oxidation on Monolayer Films of Cubic Platinum Nanoparticles Investigated by Infrared-Visible Sum Frequency Generation Vibrational Spectroscopy. *J. Phys. Chem. B* **2006,** 110, 15920-15925.
20. Goray, L. I.; Seely, J. F., Efficiencies of Master, Replica, and Multilayer Gratings for the Soft-X-Ray–Extreme-Ultraviolet Range: Modeling Based on the Modified Integral Method and Comparisons with Measurements. *Applied Optics* **2002,** 41, (7), 1434.
21. Linehan, J. C.; Stiff, C. M.; Fryxell, G. E., Simple Determination of Alkylsilane Monolayer Population Density. *Inorg. Chem. Communications* **2006,** 9, 239-241.
22. Manifar, T.; Rezaee, A.; Sheikhzadeh, M.; Mittler, S., Formation of Uniform Self-Assembly Monolayers by Choosing the Right Solvent: OTS on Silicon Wafer, a Case Study. *Applied Surface Sci* **2008,** 254, 4611-4619.
23. Parida, S. K.; Dash, S.; Patel, S.; Mishra, B. K., Adsorption of Organic Molecules on Silica Surface. *Advances in Colloid and Interface Science* **2006,** 121, 77-110.
24. Su, Y.-H.; Zhu, Y.-G.; Sheng, G. Y.; Chiou, C. T., Linear Adsorption of Nonionic Organic Compounds from Water onto Hydrophilic Minerals: Silica and Alumina *Environ. Sci. Technol* **2006,** 40, 6949-6954.
25. Matzke, M.; Thiele, K.; Müller, A.; Filser, J., Sorption and Desorption of Imidazolium Based Ionic Liquids in Different Soil Types. *Chemosphere* **2009,** 74, 568-574.
26. Jain, A. K.; Gupta, V. K.; Jain, S.; Suhas, Removal of Chlorophenols Using Industrial Wastes. *Environ. Sci. Technol.* **2004,** 38, 1195-1200.
27. Aliaga, C.; Baker, G. A.; Baldelli, S., Sum Frequency Generation Studies of Ammonium and Pyrrolidinium Ionic Liquids Based on the Bis-trifluoromethanesulfonimide Anion. *J. Phys. Chem. B* **2008,** 112, 1676-1684.
28. Aliaga, C.; Baldelli, S., Sum Frequency Generation Spectroscopy of Dicyanamide Based Room-Temperature Ionic Liquids. Orientation of the Cation and the Anion at the Gas-liquid Interface. *J. Phys. Chem. B* **2007,** 111, 9733-9740.
29. Romero, C.; Baldelli, S., Sum Frequency Generation Study of the Room-Temperature Ionic Liquids/Quartz Interface. *J. Phys. Chem. B* **2006,** 110, 6213-6223.
30. Fitchett, B. D.; Conboy, J. C., Structure of the Room-Temperature Ionic Liquid/SiO2 Interface Studied by Sum-Frequency Vibrational Spectroscopy. *J. Phys. Chem. B* **2004,** 108, 20255-20262.
31. Santos, C. S.; Baldelli, S., Gas–liquid Interface of Room-Temperature Ionic Liquids. *Chem. Soc. Rev.*, **2010,** 39, 2136–2145.
32. Waring, C.; Bagot, P. A. J.; Slattery, J. M.; Costen, M. L.; McKendrick, K. G., O(3P) Atoms as a Chemical Probe of Surface Ordering in Ionic Liquids. *J. Phys. Chem. A* **2010,** 114, 4896-4904.
33. Nakajima, K.; Ohno, A.; Suzuki, M.; Kimura, K., Observation of Molecular Ordering at the Surface of Trimethylpropylammonium Bis(trifluoromethanesulfonyl)imide Using High-Resolution Rutherford Backscattering Spectroscopy. *Langmuir* **2008,** 24, 4482-4484.

34. Hashimoto, H.; Ohno, A.; Nakajima, K.; Suzuki, M.; Tsuji, H.; Kimura, K., Surface Characterization of Imidazolium Ionic Liquids by High-Resolution Rutherford Backscattering spectroscopy and X-ray photoelectron spectroscopy. *Surface Science* **2010,** 604, 464-469.
35. Jeon, Y.; Sung, J.; Seo, C.; Lim, H.; Cheong, H.; Kang, M.; Moon, B.; Ouchi, Y.; Kim, D., Structures of Ionic Liquids with Different Anions Studied by Infrared Vibration Spectroscopy. *J. Phys. Chem. B* **2008,** 112, 4735-4740.
36. Hoefft, O.; Bahr, S.; Himmerlich, M.; Krischok, S.; Schaefer, J. A.; Kempter, V., Electronic Structure of the Surface of the Ionic Liquid [EMIM][Tf2N] Studied by Metastable Impact Electron Spectroscopy (MIES), UPS, and XPS. *Langmuir* **2006,** 22, 7120-7123.
37. Krischok, S.; Eremtchenko, M.; Himmerlich, M.; Lorenz; Uhlig, J.; Neumann, A.; Oettking, R.; Beenken, W. J. D.; Hoefft, O.; Bahr, S.; Kempter, V.; Schaefer, J. A., Temperature-Dependent Electronic and Vibrational Structure of the 1-Ethyl-3-methylimidazolium Bis(trifluoromethylsulfonyl)amide Room-Temperature Ionic Liquid Surface: A Study with XPS, UPS, MIES, and HREELS. *J. Phys. Chem. B* **2007,** 111, 4801-4806.
38. Harada, Y.; Masuda, S.; Ozak, H., Electron Spectroscopy Using Metastable Atoms as Probes for Solid Surfaces. *Chem. Rev*. **1997,** 97, 1897-1952.
39. Nishi, T.; Iwahashi, T.; Yamane, H.; Ouchi, Y.; Kanai, K.; Seki, K., Electronic Structures of Ionic Liquids [Cnmim]+[BF_4]- and [Cnmim]+[PF_6]- Studied by Ultraviolet Photoemission, Inverse Photoemission, and Near-Edge X-ray Absorption Fine Structure Spectroscopies. *Chem. Physics Letters* **2008,** 455, 213-217.
40. Zhang, Y., Dynamic Ellipsometry Study on Curved Thin Films at Pendent Droplet Surfaces. *Rev Scientific Instruments* **2010,** 81, 085101.
41. Atkin, R.; Fina, L.-M. D.; Kiederling, U.; Warr, G. G., Structure and Self Assembly of Pluronic Amphiphiles in Ethylammonium Nitrate and at the Silica Surface. *J. Phys. Chem. B* **2009,** 113, 12201-12213.
42. Aguilar, J. F.; Lera, M.; Sheppard, C. J. R., Imaging of Spheres and Surface Profiling by Confocal Microscopy. *Applied Optics* **2000,** 39, (25).
43. Winterflood, C. M.; Thomas Ruckstuhl; Verdes, D.; Seeger*, S., Nanometer Axial Resolution by Three-Dimensional Supercritical Angle Fluorescence Microscopy. *Physical Review Letters* **2010,** 105, 108103.
44. Gao, X.; Chorover, J., Adsorption of Sodium Dodecyl Sulfate (SDS) at ZnSe and a-Fe2O3 Surfaces: Combining Infrared Spectroscopy and Batch Uptake Studies. *J. Colloid and Interface Sci* **2010,** 348, 167-176.
45. Chung, E.; Kim, D.; Cui, Y.; Kim, Y.-H.; So, P. T. C., Two-Dimensional Standing Wave Total Internal Reflection Fluorescence Microscopy: Superresolution Imaging of Single Molecular and Biological Specimens. *Biophysical Journal* **2007,** 93, 1747-1757.
46. Aliaga, C.; Baldelli, S., A Sum Frequency Generation Study of the Room-Temperature Ionic Liquid-Titanium Dioxide Interface. *J. Phys. Chem. C* **2008,** 112, 3064-3072.
47. Rivera-Rubero, S.; Baldelli, S., Surface Characterization of 1-Butyl-3-methylimidazolium Br-, I-, PF6 -, BF4 -, (CF3SO2)2N-, SCN-, CH3SO3 -, CH3SO4 -, and (CN)2N- Ionic Liquids by Sum Frequency Generation. *J. Phys. Chem. B* **2006,** 110, 4756-4765.
48. Bain, C. D., Sum-frequency Vibrational Spectroscopy of the Solid/Liquid Interface. *J. Chem.Soc. Faraday Trans.* **1995,** 91, 1281-1296.
49. Gan, W.; Wu, B.-h.; Zhang, Z.; Guo, Y.; Wang, H.-f., Vibrational Spectra and Molecular Orientation with Experimental Configuration Analysis in Surface Sum Frequency Generation (SFG). *J. Phys. Chem. C* **2007,** 111, 8716-8725.

50. Ma, G.; Allen, H. C., Surface Studies of Aqueous Methanol Solutions by Vibrational Broad Bandwidth Sum Frequency Generation Spectroscopy. *J. Phys. Chem. B* **2003,** 107, 6343-6349.
51. Santos, C. S.; Baldelli, S., Surface Orientation of 1-Methyl-, 1-Ethyl-, and 1-Butyl-3-methylimidazolium Methyl Sulfate as Probed by Sum-Frequency Generation Vibrational Spectroscopy. *J. Phys. Chem. B* **2007,** 111, 4715-4723.
52. McKee, K. J.; Smith, E. A., Development of a Scanning Angle Total Internal Reflection Raman Spectrometer. *Rev Scientific Instruments* **2010,** 81, 043106.
53. Novotny, L.; Hecht, B., *Principles of Nano-Optics . Cambridge University Press* **2008,** reprint.
54. Woods, D. A.; Bain, C. D., Total Internal Reflection Raman Spectroscopy. *Analyst* **2012,** 137, 35-48.
55. Tyrode, E.; Rutland, M. W.; Bain, C. D., Adsorption of CTAB on Hydrophilic Silica Studied by Linear and Nonlinear Optical Spectroscopy. *J. Am. Chem. Soc.* **2008,** 51, 17434-17445.
56. Iwamoto, R.; Miya, M.; Ohta, K.; Mima, S., Total Internal Reflection Raman Spectroscopy as a New Tool for Surface Analysis. *J. Am. Chem. Soc. Communincations to the editor* **1980**, 1212.
57. Greene, P. R., *Ph.D. Thesis, University of Oxford* **2003**.
58. Ekhoff, J. A.; Rowlen, K. L., Effect of Interfacial Refractive Index on Optical Molecular Orientation Measurements. *Anal. Chem.* **2002,** 74, 5954-5959.
59. Woods, D. A.; Petkov, J.; Bain, C. D., Surfactant Adsorption Kinetics by Total Internal Reflection Raman Spectroscopy. 2. CTAB and Triton X-100 Mixtures on Silica. *J. Phys. Chem. B* **2011**, DOI: 10.1021/jp201338s
60. Woods, D. A.; Petkov, J.; Bain, C. D., Surfactant Adsorption Kinetics by Total Internal Reflection Raman Spectroscopy. 1. Pure Surfactants on Silica. *J. Phys. Chem. B* **2011**.DOI: 10.1021/jp2011340j.
61. Okamura, E., Umemura, J. and Takenaka, T. , High-Sensitivity Raman Spectroscopic Study on Surface-Pressure Dependence of the Structure in Thin Langmuir–Blodgett Films of Dipalmitoylphosphatidylcholine. *J. Raman Spectrosc.* **1991,** 22, 759-762.
62. Lee, C.; Bain, C. D., Raman spectra of Planar Supported Lipid Bilayers. *Biochim. Biophysica Acta* **2005,** 1711, 59-71.
63. Beattie, D. A.; Winget, S. A.; Bain, C. D., Raman Scattering from Confined Liquid Films in the Sub-Nanometre Regime. *Tribol Lett* **2007,** 27, 159-167.
64. Beattie, D. A.; Haydock, S.; Bain, C. D., A Comparative Study of Confined Organic Monolayers by Raman Scattering and Sum-Frequency Spectroscopy. *Vibrational Spectroscopy* **2000,** 24, 109-123.
65. Greene, P. R.; Bain, C. D., Total internal reflection Raman Spectroscopy of Barley Leaf Epicuticular Waxes in Vivo. *Colloids and Surfaces B: Biointerfaces* **2005,** 45, 174-180.
66. A.Michaels, C., Surface-Sensitive Raman Microscopy with Total Internal Reflection Illumination. *J. of Raman Spectrosc.* **2010**, DOI: 10.1002/jrs.2610.
67. Zhang, M.; Powell, H. V.; Mackenzie, S. R.; Unwin, P. R., Kinetics of Porphyrin Adsorption and DNA-Assisted Desorption at the Silica-Water Interface. *Langmuir* **2010**, DOI:10.1021/la903438p.
68. Knock, M. M.; Bell, G. R.; Hill, E. K.; Turner, H. J.; Bain, C. D., Sum-Frequency Spectroscopy of Surfactant Monolayers at the Oil-Water Interface. *J. Phys. Chem. B* **2003,** 107, 10801-10814.

69. Yamamoto, S.; Watarai, H., Counterion-Dependent Morphology of Porphyrin Aggregates Formed at the Liquid/Liquid Interface Studied by Total Internal Reflection Resonant Rayleigh and Raman Scattering Microscopy. *J. Phys. Chem. C* **2008,** 112, 12417-12424.
70. Fujiwara, K.; Watarai, H., Total Internal Reflection Resonance Raman Microspectroscopy for the Liquid/Liquid Interface. Ion-Association Adsorption of Cationic Mn(III) Porphine. *Langmuir* **2003,** 19, 2658-2664.
71. Jena, K. C.; Covert, P. A.; Hore, D. K., The Effect of Salt on the Water Structure at a Charged Solid Surface: Differentiating Second- and Third-order Nonlinear Contributions. *J. Phys. Chem. Lett.* **2011,** 2, 1056-1061.
72. Williams, C. T.; Yang, Y.; Bain, C. D., Total Internal Reflection Sum-Frequency Spectroscopy: A Strategy for Studying Molecular Adsorption on Metal Surfaces. *Langmuir* **2000,** 16, 2343-2350.
73. Yeganeh, M. S.; Dougal, S. M.; Silbernagel, B. G., Sum Frequency Generation Studies of Surfaces of High-Surface-Area Powdered Materials. *Langmuir* **2006,** 22, (2), 637-641.
74. Itoh, Y.; Hasegawa, T., Polarization Dependence of Raman Scattering from a Thin Film Involving Optical Anisotropy Theorized for Molecular Orientation Analysis. *J. Phys. Chem. A* **2012**.in print
75. Bain, C. D., Sum-frequency Vibrational Spectroscopy of the Solid/Liquid Interface. *J. Chem. Soc. Faraday Trans.* **1995,** 91, (9), 1281-1296.
76. Garbacik, E. T.; Korterik, J. P.; Otto, C.; Mukamel, S.; Herek, J. L.; Offerhaus, H. L., Background-Free Nonlinear Microspectroscopy with Vibrational Molecular Interferometry. *Physical Review Letters* **2011,** 107, 253902.
77. Long, D. A., Raman Spectroscopy. *McGraw-Hill international Book Co.* **1976**, 47-71.
78. Long, D. A., Raman Spectroscopy. *McGraw-Hill international Book Co.* **1976**, 41-52.
79. Harris, D. C.; Bertolucci, M. D., Symmetry and Spectroscopy: An Introduction to Vibrational and Electronic Spectroscopy. *Dover Publications, Inc. New York* **reprint 1989**, 160-162.
80. Izgorodina, E. I.; Forsyth, M.; MacFarlane, D. R., On the Components of the Dielectric Constants of Ionic Liquids: Ionic Polarization? *Phys. Chem. Chem. Phys.* **2009,** 11, 2452-2458.
81. Hecht, E., Optics 3rd Edition. *Addison-Wesley Longman, Inc.* **1998**, 112-126.
82. Butt, H.-J.; Graf, K.; Kappl, M., *Physics and Chemistry of Interfaces; 2nd Ed. (4th reprint), Wiley Publishing, Weinheim* **2011**.
83. Stubenrauch, C.; Khristov, K., Foams and Foam Films Stabilized by CnTAB: Influence of the Chain Length and of Impurities. *J. Colloid and Interface Sci* **2005,** 286, 710-718.
84. Adibhatla, B.; Mohanty, K. K.; Berger, P.; Lee, C., Effect of Surfactants on Wettability of Near-Well Bore Regions of Gas Reservoirs. *J. of Petroleum Sci Eng* **2006,** 52, 227-236.
85. Trompette, J. L.; Zajac, J.; Keh, E.; Partyka, S., Scanning of the Cationic Surfactant Adsorption on a Hydrophilic Silica Surface at Low Surface Coverages. *Langmuir* **1994,** 10, 812-818.
86. Atkin, R.; Craig, V. S. J.; Wanless, E. J.; Biggs, S., Mechanism of Cationic Surfactant Adsorption at the Solid–Aqueous Interface. *Advances in Colloid and Interface Sci* **2003,** 103, 219-304.
87. Hayes, P. L.; Chen, E. H.; Achtyl, J. L.; Geiger, F. M., An Optical Voltmeter for Studying Cetyltrimethylammonium Interacting with Fused Silica/Aqueous Interfaces at High Ionic Strength. *J. Phys. Chem. A* **2009,** 113, 4269-4280.
88. Zajac, J.; Trompette, J. L.; Partyka, S., Adsorption of Cationic Surfactants on a Hydrophilic Silica Surface at Low Surface Coverages: Effects of the Surfactant Alkyl Chain and Exchangeable Sodium Cations at the Silica Surface. *Langmuir* **1996,** 12, 1357-1367.

89. Chernyshova, I. V.; Ponnurangam, S.; Somasundaran, P., Adsorption of Fatty Acids on Iron (Hydr)oxides from Aqueous Solutions. *Langmuir* **2011,** 27, 10007-10018.
90. Dar, A. A.; Rather, G. M.; Das, A. R., Mixed Micelle Formation and Solubilization Behavior toward Polycyclic Aromatic Hydrocarbons of Binary and Ternary Cationic-Nonionic Surfactant Mixtures. *J. Phys. Chem. B* **2007,** 111, 3122-3132.
91. Fuchs-Godec, R., The Adsorption, CMC Determination and Corrosion Inhibition of Some N-alkyl Quaternary Ammonium Salts on Carbon Steel Surface in 2M H2SO4. *Colloids and Surfaces A: Physicochem. Eng. Aspects* **2006,** 280, 130-139.
92. Shimizu, S.; Seoud, O. A. E., Synthesis and Aggregation of Benzyl(2-acylaminoethyl)dimethylammonium Chloride Surfactants. *Langmuir* **2003,** 19, 238-243.
93. Treiner, C.; Makayssi, A., Structural Micellar Transition for Dilute Solutions of Long Chain Binary Cationic Surfactant Systems: A Conductance Investigation. *Langmuir* **1992,** 8, 794-800.
94. Kosmulski, M., Chapter 13: Sorption of Heavy Metal Cations on Silica. *in Adsorption on Silica Surfaces, Surfactant Series* **2000,** vol.90, 424-428.
95. Denoyel, R.; Giordano, F.; Rouquerol, J., Thermodynamic Study of Non-Ionic-Anionic Surfactant Mixtures: Micellization and Adsorption on Silica. *Colloids and Surfaces A: Physicochem. Eng. Aspects,* **1993,** 76, 141-148.
96. Umoren, S. A.; Ebenso, E. E.; Okafor, P. C.; Ogbobe, O., Water-Soluble Polymers as Corrosion Inhibitors. *Pigment & Resin Technology* **2006,** 35/6, 346-352.
97. Fuchs-Godec, R.; Pavlovic, M. G., Synergistic Effect between Non-Ionic Surfactant and Halide Ions in the Forms of Inorganic or Organic Salts for the Corrosion Inhibition of Stainless-Steel X4Cr13 in Sulphuric Acid. *Corrosion Science* **2012**,in print.
98. Somasundaran, P.; Huang, U. L., Adsorption/Aggregation of Surfactants and Their Mixtures at Solid/Liquid Interfaces. *Advances in Colloid and Interface Sci* **2000,** 88, 179 - 208.
99. Makayssi, A.; Lemordant, D.; Treiner, C., Structural Change and Micellar Composition in Aqueous Solutions of Binary Cationic Surfactant Mixtures As Deduced from Cross-Flow Ultrafiltration Experiments. *Langmuir* **1993,** 9, 2808-2813.
100. Stroem, C.; Hansson, P.; Joensson, B.; Soderman, O., Size of Cationic Surfactant Micelles at the Silica-Water Interface: A Fluorescent Probe Study. *Langmuir* **2000,** 16, (2469-2474).
101. Atkin, R.; Craig, V. S. J.; Biggs, S., Adsorption Kinetics and Structural Arrangements of Cationic Surfactants on Silica Surfaces. *Langmuir 2000* **2000,** 16, 9374-9380.
102. Hayes, P. L.; Keeley, A. R.; Geiger, F. M., Structure of the Cetyltrimethylammonium Surfactant at Fused Silica/Aqueous Interfaces Studied by Vibrational Sum Frequency Generation. *J. Phys. Chem. B* **2010,** 114, 4495-4502.
103. Elliott, J.; Cook, R., Design of Novel Corrosion Inhibiting Additives. *NACE # 08213* **2008**.
104. Ke, M.; Stevens, R. F.; Qu, Q., Novel Corrosion Inhibitor for High Density ZnBr2 Completion Brines at High Temperatures *NACE # 08630* **2008**.
105. Migahed, M. A.; AL-Sabag, A. M., Beneficial Role of Surfactants as Corrosion Inhibitors in Petroleum Industry: A Review Article. *Chem. Eng. Comm.* **2009,** 196, 1054-1075.
106. Zanten, R. v., Stabilizing Viscoelastic Surfactants in High Density Brines. *SPE #1414474* **2011**.
107. Kharnis, E.; Al-Lohedan, H. A.; Al-Mayouf, A.; lssa, Z. A., Adsorption Effect of Cationic Surfactants on Corrosion Inhibition of Steel. *Mat.-wiss., u. Werkstofftech.* **1997,** 28, 46-50.

108. Nagarajan, R.; Ruckenstein, E., Theory of Surfactant Self -Assembly: A Predictive Molecular Thermodynamic Approach. *Langmuir* **1991,** 7, 2934-2969.
109. Gonzalez-Perez, A.; Czapkiewicz, J.; Castillo, J. L. D.; Rodrıguez, J. R., Micellar Properties of Long-Chain Alkyldimethylbenzylammonium Chlorides in Aqueous Solutions. *Colloids and Surfaces A: Physicochem. Eng. Aspects* **2001,** 193, 129-137.
110. Gonzalez-Perez, A.; Castillo, J. L. D.; Czapkiewicz, J.; Rodrıguez, J. R., Micellization of Decyl- and Dodecyldimethylbenzylammonium Bromides at Various Temperatures in Aqueous Solutions. *Colloid Polym Sci* **2002,** 280, 503-508.
111. Hunter, R. J., *Foundations of Colloid Science. Clarendon Press, Oxford Science Pubs,* **1987,** Vol. 1.
112. Okano, L. T.; Quina, F. H.; Seoud, O. A. E., Fluorescence and Light-Scattering Studies of the Aggregation of Cationic Surfactants in Aqueous Solution:Effects of Headgroup Structure. *Langmuir* **2000,** 17, 3119-3123.
113. Coret, J.; Shiloachb, A.; Berger, P.; Blankschtein, D., Critical Micelle Concentrations of Ternary Surfactant Mixtures: Theoretical Prediction with User-Friendly Computer Programs and Experimental Design Analysis. *J Surfactants and Detergents, Vol. 5, No. 1* **1999,** 5, (1),51-58
114. Berger, P. D.; Lee, C. H., New Anionic Alkylaryl Surfactants Based on Olefin Sulfonic Acids. *J Surfactants and Detergents* **2002,** 5, (1), 39-43.
115. Makayssi, C. T. a. A., Structural Micellar Transition for Dilute Solutions of Long Chain Binary Cationic Surfactant Systems: A Conductance Investigation. *Langmuir* **1992,** 8, 794-800.
116. Gonzalez-Perez, A.; Castillo, J. L. d.; Czapkiewicz, J.; Rodrıguez, J. R., Conductivity, Density, and Adiabatic Compressibility of Dodecyldimethylbenzylammonium Chloride in Aqueous Solutions. *J. Phys. Chem. B* **2001,** 105, 1720-1724.
117. Zana, R., Critical Micellization Concentration of Surfactants in Aqueous Solution and Free Energy of Micellization. *Langmuir* **1996,** 12, 1208-1211.
118. Hunter, R. J., Association Colloids:. *in: Foundations of Colloid Science, Clarendon Press, Oxford Science Pubs* **1987,** 1, 570.
119. Zajac, J.; Chorro, C.; Lindheimer, M.; Partyka, S., Thermodynamics of Micellization and Adsorption of Zwitterionic Surfactants in Aqueous Media. *Langmuir* **1997,** 13, 1486-1495.
120. Evans, D. F.; Ninham, B. W., Ion Binding and the Hydrophobic Effect. *J. Phys. Chem.* **1983,** 87, (24), 5025-5032.
121. Pegram, L. M.; M. Thomas Record, J., Hofmeister Salt Effects on Surface Tension Arise from Partitioning of Anions and Cations between Bulk Water and the Air-Water Interface. *J. Phys. Chem. B* **2007,** 111, 5411-5417.
122. Dove, P. M.; Craven, C. M., Surface Charge Density on Silica in Alkali and Alkaline Earth Chloride Electrolyte Solutions. *Geochim. Cosmochim. Acta* **2005,** 69, (21), 4963-4970.
123. Chen, V.; Evans, D. F.; Ninham, B. W., Counterion and Co-Ion Specificity in Ionic Microemulsions. *J. Phys. Chem.* **1987,** 91, (7), 1823-26.
124. Para, G.; Warszynski, P., Cationic Surfactant Adsorption in the Presence of Divalent Ions. *Colloids and Surfaces A: Physicochem. Eng. Aspects* **2007,** 300, 346-352.
125. Hunter, R. J., Chapter 10: Association Colloids *in: Foundations of Colloid Science, Clarendon Press, Oxford Science Pubs* **1987,** Vol.1, 571-572.
126. Malin, J. N.; Holland, J. G.; Geiger, F. M., Free Energy Relationships in the Electric Double Layer and Alkali Earth Speciation at the Fused Silica/Water Interface. *J. Phys. Chem. C* **2009,** 113, 17795-17802.
127. Strom, C.; Jonsson, B.; Soderman, O.; Hansson, P., Adsorption of a Divalent Cationic Surfactant onto a Silica Surface. *Colloids and Surfaces A: Physicochem. Eng. Aspects* **1999,** 159, 109-120.

128. Kim, J.; Cremer, P. S., IR-Visible SFG Investigations of Interfacial Water Structure upon Polyelectrolyte Adsorption at the Solid/Liquid Interface. *J. Am. Chem. Soc.* **2000,** 122, 12371-12372.
129. Flores, S. C.; Kherb, J.; Konelick, N.; Chen, X.; Cremer, P. S., The Effects of Hofmeister Cations at Negatively Charged Hydrophilic Surfaces. *J. Phys. Chem. C* **2012,** 116, 5730-5734.
130. Hunter, R. J., Association Colloids. *in: Foundations of Colloid Science, Clarendon Press, Oxford Science Pubs* **1987,** 1, 608-610.
131. Butt, H. J.; Graf, K.; Kappl, M., Physics and Chemistry of Interfaces. *Wiley Publishing, Weinheim* **2011,** 2nd Ed., (4th reprint), 13-16.
132. Lunkenheimer, K.; Miller, R., A Criterion for Judging the Purity of Adsorbed Surfactant Layers. *Journal of Colloid and Interface Science* **1987,** 120, (1),176
133. Gonzalez-Perez, A.; Czapkiewicz, J.; Prieto, G.; Rodrıguez, J. R., Second Critical Micelle Concentration of Dodecyldimethylbenzylammonium Chloride in Aqueous Solution at 25 C. *Colloid Polym Sci* **2003,** 281, 1191-1195.
134. Butt, H.-J.; Graf, K.; Kappl, M., Physics and Chemistry of Interfaces. *Wiley Publishing, Weinheim* **2011**, 200.
135. Petersen, P. B.; Saykally, R. J., Probing the Interfacial Structure of Aqueous Electrolytes with Femtosecond Second Harmonic Generation Spectroscopy. *J. Phys. Chem. B* **2006,** 110, 14060-140.
136. Al-Abadleh, H. A.; Mifflin, A. L.; Bertin, P. A.; Nguyen, S. T.; Geiger, F. M., Control of Carboxylic Acid and Ester Groups on Chromium (VI) Binding to Functionalized Silica/Water Interfaces Studied by Second Harmonic Generation. *J. Phys. Chem. B* **2005,** 109, 9691-9702.
137. Rosen, R. J., *Surfactants and Interfacial Phenomena. Wiley-Interscience* **2004**, (3rd ed.).
138. Norde, W., *Colloids and Interfaces in Life Sciences and Bionanotechnology. CRC Press, Taylor & Francis Group* **2011**.
139. Hecht, E., *Optics, 3rd Edition Addison-Wesley Longman, Inc.* **1998.**
140. Turrell, C.; Corset, J., *Raman Microscopy: Developments and Applications.Academic Press, Harcout Brace&Co.* **1996**.
141. Wang, J.; Wang, H.; Zhang, S.; Zhang, H.; Zhao, Y., Conductivities, Volumes, Fluorescence, and Aggregation Behavior of Ionic Liquids [C4mim][BF4] and [Cnmim]Br (n) 4, 6, 8, 10, 12) in Aqueous Solutions. *J. Phys. Chem. B* **2007,** 111, 6182-6188.
142. Zhaoa, B. D. X.; Zheng, L.; Zhang, J.; Lia, N.; Inoue, T., Aggregation Behavior of Long-Chain Imidazolium Ionic Liquids in Aqueous Solution: Micellization and Characterization of Micelle Microenvironment. *Colloids and Surfaces A: Physicochem. Eng. Aspects* **2008,** 317, 666-672.
143. Bowers, J.; Butts, C. P.; Martin, P. J.; Vergara-Gutierrez, M. C., Aggregation Behavior of Aqueous Solutions of Ionic Liquids. *Langmuir* **2004,** 20, 2191-2198.
144. Farías, T.; Ménorval, L. C. d.; J. Zajacb, A. R., Solubilization of Drugs by Cationic Surfactants Micelles: Conductivity and 1H NMR experiments. *Colloids and Surfaces A: Physicochem. Eng. Aspects* **2009,** 345, 51-57.
145. Rodriguez-Navarro, C.; Doehne, E.; Sebastian, E., Influencing Crystallization Damage in Porous Materials through the Use of Surfactants: Experimental Results Using Sodium Dodecyl Sulfate and Cetyldimethylbenzylammonium Chloride. *Langmuir* **2000,** 16, 947-854.
146. Ledbetter, J. W.; Bowen, J. R., Spectrophotometric Determination of the Critical Micelle Concentration of Some Alkyldimethylbenzylammonium Chlorides Using Fluorescein. *Anal. Chem.* **1969,** 10, (10), 1345.

147. Okano, L. T.; Quina, F. H.; Seoud, O. A. E., Fluorescence and Light-Scattering Studies of the Aggregation of Cationic Surfactants in Aqueous Solution: Effects of Headgroup Structure. *Langmuir* **2000,** 16, 3119-3123.
148. Lunkenheimer, K.; Lind, A.; Jost, M., Surface Tension of Surfactant Solutions. *J. Phys. Chem. B* **2003,** 107, (31).
149. Santos, C. S.; Rivera-Rubero, S.; Dibrov, S.; Baldelli, S., Ions at the Surface of a Room-Temperature Ionic Liquid. *J. Phys. Chem. C* **2007,** 111, 7682-7691.
150. Sears, W. M.; Hunt, J. L.; Stevens, J. R., Raman Spectra at Low Temperature and Depolarization Ratios for Styrene and Polystyrene. *J. Chem. Physics* **1982,** 77, (4),1639
151. Somasundaran, P.; Fuerstenau, D. W., Mechanisms of Alkyl Sulfonate Adsorption at the Alumina-Water Interface. *J. Phys. Chem.* **1966,** 70, (1), 90.
152. Shimizu, S.; Pires, P. A. R.; Seoud, O. A. E., Thermodynamics of Micellization of Benzyl(2-acylaminoethyl)dimethylammonium Chloride Surfactants in Aqueous Solutions: A Conductivity and Titration Calorimetry Study. *Langmuir* **2004,** 20, 9551-9559.
153. Thompson, W. R.; Pemberton, J. E., Raman Spectroscopy of Covalently Bonded Alkylsilane Layers on Thin Silica Films Immobilized on Silver Substrates. *Anal. Chem.* **1994,** 66, 3362-3370.
154. Pemberton, J. E.; Mark A. Bryant, R.; Sobocinski, L.; Joa, S. L., A Simple Method for Determination of Orientation of Adsorbed Organics of Low Symmetry Using Surface-Enhanced Raman Scattering. *J. Phys. Chem.* **1992,** 96, 3716-3182.
155. Orendorff, C. J.; Michael W. Ducey, J.; Pemberton, J. E., Quantitative Correlation of Raman Spectral Indicators in Determining Conformational Order in Alkyl Chains. *J. Phys. Chem. A* **2002,** 106, 6991-6998.
156. Orendorff, C. J.; Michael W. Ducey, J.; Pemberton, J. E., Structure-Function Relationships in High-Density Octadecylsilane Stationary Phases by Raman Spectroscopy. 3. Effects of Self-Associating Solvents. *Anal. Chem.* **2003,** 75, 3360-3368.
157. Calkins, J. A.; Peacock, A. C.; Sazio, P. J. A.; Allara, D. L.; Badding, J. V., Spontaneous Waveguide Raman Spectroscopy of Self-Assembled Monolayers in Silica Micropores. *Langmuir* **2011,** 27, (2), 630-636.
158. Miranda, P. B.; Shen, Y. R., Liquid Interfaces: A Study by Sum-Frequency Vibrational Spectroscopy. *J. Phys. Chem. B* **1999,** 103, 3292-3307.
159. Richmond, G. L., Molecular Bonding and Interactions at Aqueous Surfaces as Probed by Vibrational Sum Frequency Spectroscopy. *Chem. Rev.* **2002,** 102, 2693-2724.
160. Shen, Y. R.; Ostroverkhov, V., Sum-Frequency Vibrational Spectroscopy on Water Interfaces: Polar Orientation of Water Molecules at Interfaces. *Chem. Rev. 2006,* **2006,** 106, 1140-1154.
161. Xu, M.; Spinney, R.; Allen, H. C., Water Structure at the Air-Aqueous Interface of Divalent Cation and Nitrate Solutions. *J. Phys. Chem. B* **2009,** 113, 4102-4110.
162. Irish, D. E.; Davis, A. R., Interactions in aqueous alkali metal nitrate solutions. *Canadian J. Chem.* **1968,** 46, 943.
163. Zhang, Y.-H.; Chan, C. K., Observations of Water Monomers in Supersaturated NaClO4, LiClO4, and Mg(ClO4)2 Droplets Using Raman Spectroscopy. *J. Phys. Chem. A* **2003,** 107, 5956-5962.
164. Cappa, C. D.; Smith, J. D.; Wilson, K. R.; Messer, B. M.; Gilles, M. K.; Cohen, R. C.; Saykally, R. J., Effects of Alkali Metal Halide Salts on the Hydrogen Bond Network of Liquid Water. *J. Phys. Chem. B* **2005,** 109, 7046-7052.
165. Irish, D. E.; Chang, T. G.; S.-Y. Tang, Raman and Ultrasonic Relaxation Studies of Some Nitrate Salts in N-Methylacetamide. *J. Phys. Chem. B* **1981,** 85, 1686-1692.

166. Li, P. X.; Dong, C. C.; Thomas, R. K., Adsorption of Gemini Surfactants with Dodecyl Side Chains and Different Spacers, Including Partially Fluorinated Spacers, on Different Surfaces: Neutron Reflectometry Results. *Langmuir* **2011,** 27, (5), 1844-1852.
167. Yang, Y.; Bittner, A. M.; Baldelli, S.; Kern, K., Study of Self-Assembled Triethoxysilane Thin Films Made by Casting Neat Reagents in Ambient Atmosphere. *Thin Solid Films* **2008,** 516, 3948-3956.
168. Ye, S.; Nihonyanagi, S.; Uosaki, K., Sum Frequency Generation (SFG) Study of the pH-Dependent Water Structure on a Fused Quartz Surface Modified by an Octadecyltrichlorosilane (OTS) Monolayer. *Phys. Chem. Chem. Phys.* **2001,** 3, 3463-3469.
169. Santos, C. S.; Baldelli, S., Gas-Liquid Interface of Hydrophobic and Hydrophilic Room-Temperature Ionic Liquids and Benzene: Sum Frequency Generation and Surface Tension Studies. *J. Phys. Chem. C* **2008,** 112, 11459-11467.
170. Kiraly, Z.; Findenegg, G. H., Calorimetric Evidence of the Formation of Half-Cylindrical Aggregates of a Cationic Surfactant at the Graphite/Water Interface. *J. Phys. Chem. B* **1998,** 102, 1203-1211.
171. Meziani, M. J.; Zajac, J.; Partyka, S., Adsorption and Interfacial Aggregation of a Cationic Quaternary Ammonium Surfactant on Powdered Mesoporous MCM-41 Aluminosilicates from Dilute Aqueous Solutions. *Langmuir* **2000,** 16, 8410-8418.
172. Duffy, D. C.; Davies, P. B., Polymer-Surfactant Aggregates at a Hydrophobic Surface Studied Using Sum-Frequency Vibrational Spectroscopy. *Langmuir* **1996,** 11, 2931-2937.
173. Evans, D. F.; Ninham, B. W., Molecular Forces In the Self-Organizatlon of Amphiphiles. *J. Phys. Chem.* **1986,** 90, (2), 226-233.
174. Galgano, P. D.; Seoud, O. A. E., Micellar Properties of Surface Active Ionic Liquids: A Comparison of 1-Hexadecyl- 3-Methylimidazolium Chloride with Structurally Related Cationic Surfactants. *J. Colloid and Interface Sci* **2010,** 345, 1-11.